

Louisiana Tech University

## Louisiana Tech Digital Commons

---

Doctoral Dissertations

Graduate School

---

Summer 8-2022

# UNDERSTANDING THE SHEAR DEFORMATION MECHANISM OF TRANSITION METAL/CERAMIC INTERFACES USING COMPUTATIONAL METHODS

Nisha Dhariwal

*Louisiana Tech University*

Follow this and additional works at: <https://digitalcommons.latech.edu/dissertations>

---

### Recommended Citation

Dhariwal, Nisha, "" (2022). *Dissertation*. 973.

<https://digitalcommons.latech.edu/dissertations/973>

This Dissertation is brought to you for free and open access by the Graduate School at Louisiana Tech Digital Commons. It has been accepted for inclusion in Doctoral Dissertations by an authorized administrator of Louisiana Tech Digital Commons. For more information, please contact [digitalcommons@latech.edu](mailto:digitalcommons@latech.edu).

**UNDERSTANDING THE SHEAR DEFORMATION  
MECHANISM OF TRANSITION METAL/CERAMIC INTERFACES  
USING COMPUTATIONAL METHODS**

by

Nisha Dhariwal, M.Tech, M.Sc

A Dissertation Presented in Partial Fulfillment  
of the Requirements of the Degree  
Doctor of Philosophy

COLLEGE OF ENGINEERING AND SCIENCE  
LOUISIANA TECH UNIVERSITY

August 2022

LOUISIANA TECH UNIVERSITY

GRADUATE SCHOOL

July 18, 2022

Date of dissertation defense

We hereby recommend that the dissertation prepared by

**NISHA DHARIWAL, M.Tech, M.Sc**

entitled **UNDERSTANDING THE SHEAR DEFORMATION**

**MECHANISM OF TRANSITION METAL/CERAMIC INTERFACES**

**USING COMPUTATIONAL METHODS**

be accepted in partial fulfillment of the requirements for the degree of

**Doctor of Philosophy in Molecular Sciences and Nanotechnology**



Collin Wick

Supervisor of Dissertation Research



Gergana Nestorova

Head of Molecular Sciences and Nanotechnology

**Doctoral Committee Members:**

Ramu Ramachandran

Pedro Derosa

Adarsh Radadia

Shengnian Wang

**Approved:**



Hisham Hegab

Dean of Engineering & Science

**Approved:**



Ramu Ramachandran

Dean of the Graduate School

## ABSTRACT

The objective of this research was to investigate the deformation behavior of metal/ceramic interfaces under external loadings in a multi-scale framework including first principles density functional theory (DFT) and molecular dynamics (MD) simulations. The mechanical properties of the metal/ceramic interfaces are dominated by defects on a length scale that first principles computations cannot access. Since the DFT calculations become computationally expensive for such large sized systems, therefore, MD simulations are required to deal with such systems. For MD simulations, second nearest neighbor modified embedded atom method (MEAM) potentials were developed to study metal/ceramic interfaces involving Cr, Ti, Al, and N.

The effect of misfit dislocation networks (MDNs) on the stability and shear strength of Cr/TiN was investigated using the newly developed potential. Good agreement with a combination of experimental and DFT results was achieved. The interfacial energy was lowest when the MDN was located in the Cr layer adjacent to the chemical interface, which also had the largest dislocation core width. This was consistent with generalized stacking fault energies, which had lower energy barriers between the first and second Cr layers next to the chemical interface. For all positions of MDNs, shear failure occurred in the ceramic, between the first and the second TiN layers next to the chemical interface. The lowest shear strength was found for the system with the MDN in the first Cr layer with respect to the

chemical interface. Only for this particular configuration was there a significant plastic deformation present.

The impact of Al doping on the stability and shear strength of Ti/TiN metal/ceramic interface was also investigated. The model was parameterized to the interfacial properties of pure Al, TiAl and AlN binaries as well as TiAlN ternary systems. A Monte Carlo scheme was developed to find the most likely doping configuration of Al atoms in Ti/TiN. The doping was increased up to 25 mol % Al concentration after which the enthalpy of mixing started to increase. There was a drastic increase in the maximum shear stress from about 200 MPa in case of the undoped system to almost 1 GPa for the 25 mol % Al doped Ti/TiN. This study would be particularly useful in materials-based engineering of metal/ceramic interfaces and will have a significant impact on applications of ceramic coating/substrate systems in material engineering.

## **APPROVAL FOR SCHOLARLY DISSEMINATION**

The author grants to the Prescott Memorial Library of Louisiana Tech University the right to reproduce, by appropriate methods, upon request, any or all portions of this Dissertation. It is understood that “proper request” consists of the agreement, on the part of the requesting party, that said reproduction is for his personal use and that subsequent reproduction will not occur without written approval of the author of this Dissertation. Further, any portions of the Dissertation used in books, papers, and other works must be appropriately referenced to this Dissertation.

Finally, the author of this Dissertation reserves the right to publish freely, in the literature, at any time, any or all portions of this Dissertation.

Author \_\_\_\_\_

Date \_\_\_\_\_

## **DEDICATION**

This dissertation is dedicated to my father, Dr. Tarsem Dhariwal, who has been my biggest source of inspiration.

## TABLE OF CONTENTS

ABSTRACT.....	iii
APPROVAL FOR SCHOLARLY DISSEMINATION .....	v
DEDICATION .....	vi
LIST OF FIGURES .....	ix
LIST OF TABLES .....	xii
ACKNOWLEDGMENTS .....	xiii
CHAPTER 1 INTRODUCTION .....	1
1.1    Metal/ceramic interfaces.....	1
1.1.1    Background.....	1
1.1.2    Experimental tools to study metal/ceramic interfaces .....	5
1.2    Atomistic level simulations .....	6
1.3    Organization of the dissertation.....	10
CHAPTER 2 MEAM Interatomic potential .....	11
2.1    Second nearest neighbor MEAM potential.....	11
2.2    MEAM potential formalism.....	14
2.3    Minimization and genetic algorithm.....	17
CHAPTER 3 MD study of metal/ceramic interfaces.....	19
3.1    Cr/TiN metal/ceramic system .....	19

3.2	General details .....	20
3.2.1	DFT calculations .....	20
3.2.2	Calculation of Properties from the MEAM Model .....	23
3.3	Results and discussion .....	26
3.3.1	Pure Cr metal .....	26
3.3.2	Mixed systems .....	27
3.3.3.	Stability of Cr/TiN systems .....	32
3.4	Impact of shear on Cr/TiN systems .....	37
CHAPTER 4 Doped metal/ceramic systems .....		44
4.1	Introduction.....	44
4.2	DFT calculations.....	47
4.3	Calculation of properties from the MEAM model.....	49
4.4	Large scale MD simulations .....	50
4.6.	Results and discussion .....	52
4.6.	Large scale simulation .....	59
CHAPTER 5 CONCLUSIONS AND FUTURE WORK.....		66
5.1	Future work.....	67
APPENDIX A.....		71
APPENDIX B .....		73
BIBLIOGRAPHY .....		76

## LIST OF FIGURES

<b>Figure 1-1:</b> Metal interlayer deposited in between the ceramic coating and the substrate .....	3
<b>Figure 2-1:</b> Atom embedded into homogeneous electron gas.....	12
<b>Figure 2-2:</b> The values of $C_{\max}$ and $C_{\min}$ are adjusted to control the second nearest neighbor interaction .....	16
<b>Figure 2-3:</b> Parameter Optimization Procedure for the MEAM potential [119] (b) Genetic Algorithm for simultaneous optimization of MEAM parameter.....	18
<b>Figure 3-1:</b> (a) Cr(001)/TiN(001) structure with the atomic layers denoted by M and the interlayer planes denoted by P, (b) Schematic of the shear displacements for calculating the GSFЕ surface of the Cr/TiN metal/ceramic system. ....	23
<b>Figure 3-2:</b> (a) Cr(001)/TiN(001) structure (b) orientation relationship in Cr/TiN multilayers. The top and the bottom red colored regions are the fixed atoms.....	25
<b>Figure 3-3:</b> GSFЕs of Cr(001) calculated using (a) DFT, (b) new model (c) Lee model [139] (d) Comparison of minimum energy path of the GSFЕ for Cr(001).....	27
<b>Figure 3-4:</b> GSFЕs of the Cr/TiN calculated using (a) DFT (b) MEAM for P = 0 and P = 1 planes. (c) A comparison of minimum energy path extracted from the GSFЕs for P =0 and P= 1. ....	32
<b>Figure 3-5:</b> MDN structure of Cr/TiN system at (a) M=1, (b) M=2, and (c) M=5 (d) M=1 (X axis only) layers. Atoms are color-coded according to CSP results. ....	34
<b>Figure 3-6:</b> Dislocation core width with respect to the location of MDN (M). ....	35
<b>Figure 3-7:</b> Plot of the difference in the interfacial energy with respect to the coherent interfacial energy as a function of MDN location (M). ....	36
<b>Figure 3-8:</b> Plot of interfacial shear strength vs. the location of MDN (M). ....	38

<b>Figure 3-9:</b> Plot of the difference in displacement (D) per layer per stress step for (a) coherent (b) MDN at M=1 and (c) M=5 layer. ....	40
<b>Figure 3-10:</b> Snapshots of the displacement of atoms immediately after shear failure (a) for coherent system and (b) for with MDNs at the M=1 layer. Red atoms represent Cr, blue atoms N, and white atoms Ti. ....	41
<b>Figure 3-11:</b> (a) Stress vs stress step scaled by the fracture step. (b-f) Snapshots of different configurations in the shear calculations as shown in the stress plot with letters on the stress plot corresponding to the snapshot letters in parenthesis. ....	42
<b>Figure 4-1:</b> Al doped Ti/TiN metal/ceramic system snapshot with 4 mol%. ....	52
<b>Figure 4-2:</b> Comparison of the 1D-GSFEs for pure Al from DFT, the new MEAM model, and the Lee model along the (a) (001) and (b) (111) planes. ....	54
<b>Figure 4-3:</b> (a) Snapshot of the Al (red atoms) and Ti (gray atoms) used to calculate the GSFE. (b) Comparison of DFT, the new model and the Lee model [96] 1D-GSFE for this system. ....	58
<b>Figure 4-4:</b> Comparison of the 1D-GSFE for Ti/TiN with (a) 1 Al atom in the M=1 layer (b) 2 Al atoms in the M=2 layer (c) 16 Al atoms extracted from MC calculations. ....	59
<b>Figure 4-5:</b> (a) Plot of the total energy with respect to MC step (b) Enthalpy of mixing of various Al doped Ti/TiN metal/ceramic systems (c) Aluminum concentration in each layer of Ti/TiN system with the snapshot below the figure shows the position of each layer. ....	61
<b>Figure 4-6:</b> (a) Plots of shear stress versus iteration step, and (b) of maximum shear stress achieved for the different Al concentrations in Ti/TiN interfacial systems. ....	63
<b>Figure 4-7:</b> Snapshots of displacement for various layers of Al doped Ti/TiN surfaces ....	64
<b>Figure 4-8</b> (top) Snapshots of various Al doped Ti/TiN surfaces with green representing fcc, red hcp, and gray neither. (bottom) Dislocation and Burgers vector analysis of various Al doped Ti/TiN systems. Black arrows indicate Burgers vectors, blue lines indicate an edge type dislocation and red line indicate a screw type dislocation. ....	65

<b>Figure A-1:</b> GSFE curves of the Cr along (110) plane calculated using (a) DFT, (b) MEAM model (c) Lee model (d) Comparison of minimum energy path (1-D GSFE) for pure Cr along (110) plane .....	70
<b>Figure A-2:</b> Plot of the displacement per layer per iteration step for (a) M=2, (b) M=3 and (c) M=4 layers .....	71
<b>Figure B-1:</b> GSFE curves of the Al(001) calculated using (a) DFT, (b) MEAM model (c) Lee model .....	72
<b>Figure B-2:</b> GSFE curves of the Al(111) calculated using (a) DFT, (b) MEAM model (c) Lee model .....	72
<b>Figure B-3:</b> 2D GSFE plots of the Al doped bulk Ti using (a) DFT, (b) MEAM model and (c) Lee model.....	73
<b>Figure B-4:</b> 2D GSFE plots of the Ti/TiN system with 1 Al atom in M =2 layer using (a) DFT and (b) new MEAM model.....	73
<b>Figure B-5:</b> 2D GSFE plots of the Ti/TiN system with 2 Al atoms in M =2 layer using (a) DFT and (b) new MEAM model.....	74
<b>Figure B-6:</b> 2D GSFE plots of the Ti/TiN system with 16 Al atoms using (a) DFT and (b) new MEAM model.....	74

## LIST OF TABLES

<b>Table 3-1:</b> MEAM potential parameter sets for pure Cr, Ti, and N.....	26
<b>Table 3-2:</b> Comparison of the DFT calculated/experimental properties of Cr with values obtained from the MEAM model. ....	28
<b>Table 3-3:</b> MEAM potential parameters for the binary systems ( $x$ - $y$ ). In any pair, the first element is denoted by $x$ , and the second element is denoted by $y$ . ....	29
<b>Table 3-4:</b> MEAM potential parameters for the Cr/TiN ternary system.....	29
<b>Table 3-5:</b> Comparison of DFT calculated values of properties of binary CrN and Cr <sub>2</sub> Ti and ternary Cr/TiN with the MEAM fitted values.....	31
<b>Table 4-1:</b> MEAM potential parameters for Ti-Al-N.....	53
<b>Table 4-2:</b> Comparison of the DFT calculated/experimental properties of Al with values obtained using the Lee model [96] and the newly developed model in this work. ....	53
<b>Table 4-3:</b> MEAM potential parameters for the binary systems ( $x$ - $y$ ). In any pair, the first element is denoted by $x$ , and the second element is denoted by $y$ . ....	55
<b>Table 4-4:</b> MEAM potential parameters for the Ti-Al-N ternary system .....	55
<b>Table 4-5:</b> Values of the properties of the TiAl binary model compared with the experimental/DFT results.....	56
<b>Table 4-6:</b> Values of the properties of the TiAlN ternary model compared with the experimental/DFT results.....	57

## **ACKNOWLEDGMENTS**

I would like to thank quite a number of people for making this dissertation possible. First, I would like to thank Waheguru, and Lord Krishna, for providing me strength to carry out this work. I would like to express my deepest gratitude to my advisor Dr. Collin Wick and Dr. Bala Ramu Ramachandran for their guidance and support throughout this journey. I would have never been able to complete this work without their constant motivation and encouragement.

I would like to thank my advisory committee members, Dr. Adarsh Radadia, Dr. Pedro Derosa and Dr. Shengnian Wang for their careful review and valuable insights. I have benefitted from numerous discussions with my lab mate, Abu Shama Mohammed Miraz, who has always been a constant support throughout my journey. I am ever so grateful to Kulwinderjit Singh, who has been the biggest source of my strength and emotional support during this journey. I also thank the faculties from Louisiana State University whom I had the great fortune to collaborate with, Dr. Shuai Shao and Dr. Wen Jin Meng. Finally, I would like to thank Louisiana Board of Regents, National Science Foundation and Louisiana Tech University for supporting my work through the following grants, #OIA-1541079 and #OIA-1946231.

# CHAPTER 1

## INTRODUCTION

### 1.1 Metal/ceramic interfaces

#### 1.1.1 Background

The study of metal/ceramic systems is becoming an increasingly important area of research, both scientifically and technologically, due to their wide range of industrial applications including electro ceramic devices, nanolaminates, structural composites, thermal barrier coatings on high temperature materials, corrosion protection, advanced packaging technology for electronic devices, wear-resistant materials, medical implants, high temperature aircraft structures and protective coatings [1–12]. For instance, thermal barrier coatings (TBCs) have been extensively utilized to safeguard gas and jet turbine engines [7]. In microelectronics packaging, interfaces between metallic inter-connects and ceramics are common, and impact the performance and longevity of solid-state devices [13]. Such significant applications have motivated researchers to try to understand and develop a fundamental structure-property relationship for the metal/ceramic systems.

Metal/ceramic systems combine the properties of metals, such as ductility, high electrical and thermal conductivity with the properties of ceramics such as high hardness, corrosion resistance and wear resistance [14]. In metal/ceramic systems, the overall composite properties depend on the properties of the metal/ceramic ‘interface’ [15,16] and interfacial failures can limit their durability as well as reliability [17]. The study of the

structure-property relationship between metal/ceramic interfaces is necessary because of a number of factors as discussed below:

- The significance of interfaces lies in the fact that physical and chemical properties change dramatically at or near the interface. Atoms at or near the interface do not possess the same local environment and hence, characterizing the local atomic structure near the interface becomes important.
- With the decrease in size, the surface to volume ratio of any object increases resulting in dramatic impact on its several properties [18]. It is observed that the interfacial area per unit volume of the metal/ceramic system increases many folds at nano scale which in turn impacts the bulk mechanical properties of the system [19].
- Usually, there is a large difference in the strength and elastic modulus between the metal and ceramic phase and it is observed that the stress required to move the dislocation inside a ceramic is much higher than the metal [20]. Thus, it is worthwhile to investigate the deformation behavior of the metal/ceramic system with the possibility of enhancing the shear strength of the composite upon inclusion of the ceramic material.
- Another crucial concern is spallation of TBCs that are used to safeguard the components of gas and jet turbine engines [2]. A detailed insight into the structure property relationship of metal ceramic interfaces can result in the improvement of the operating conditions that lead to their failure [7].

Hence, it is important to understand the relationship between the structure and properties of metal/ceramic interfaces in order to develop a fundamental understanding of their failure process and provide standards for optimum selection and processing of metal/ceramic systems for current and future applications [15].

In a number of ceramic-coated mechanical components and manufacturing tools, the mechanical integrity of the interfacial region between the ceramic coatings and substrates is critical [21] since the mechanical failure of the coating/substrate interfacial region leads to a catastrophic failure of the coated system as a whole. Interfacial mechanical integrity can often be improved by the addition of thin metal interlayers between the ceramic coating and the substrate (**Figure 1-1**)[22]. However, not much quantitative data exists in order to explain the interfacial mechanical response of the ceramic/metal/substrate system and most of the selection of ceramic/metal/substrate system depends largely on trial-and-error manner.

In general, a defined orientation relationship occurs between the two crystal lattices during the formation of interfaces [23] and they are termed as coherent, semi-coherent or incoherent depending on whether the lattice spacing structure of both the lattices match perfectly, partially, or not at all.

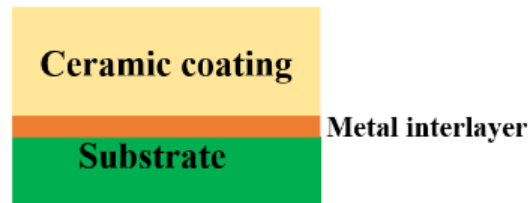


**Figure 1-1:** Metal interlayer deposited in between the ceramic coating and the substrate

A coherent interface is formed when the two crystals match perfectly at the interface and the two lattices seem to be continuous across the interface. Usually, a perfect matching occurs up to a lattice mismatch of tensile or compressive stress up to  $\pm 10\%$ . In incoherent or semi-coherent interfaces, the locally coherent regions are separated by ‘misfit dislocations’ (MDNs) [3]. Due to the lattice mismatch and orientation relationship between

the constituent materials, the MDNs are formed that have a significant impact on the interfacial adhesion and failure mechanism [23,24]. MDNs usually form to relieve the strain between the two constituent materials with large lattice mismatch. The greater the initial mismatch, the higher is the MDN density in those instances. Under the shear stress, the glide of these MDNs and/or the formation of interfacial dislocation loops at nodes have been shown to lower the interfacial shear resistance [25,26].

Earlier, the prime focus of the metal/ceramic research was to study the wettability and adhesive property and hence much of the research efforts were carried out to study the work of adhesion of these materials [15,27]. Multilayered metal/metal nitride systems gained much attraction due to their remarkable mechanical properties during deformation [23]. Out of various metal/metal nitride systems, transition metal nitrides such as TiN and CrN are good candidates for coatings on machining tools due to their high hardness, high melting point, and good wear resistance [28–30]. However, they display low adhesion to the substrate in many cases [29]. Enhanced plastic co-deformation was observed in Al/TiN at a layer thickness of 5 nm or below due to the lattice dislocations that nucleated from interfaces and propagated inside both metal and ceramic layers during the deformation processes [19,26,27]. A significant effect of layer thickness on the mechanical deformation behavior was also observed in the same metal/ceramic system. For metal/ceramic systems with large individual layer thickness, plastic co-deformation could not be achieved which resulted in cracking inside the ceramic layers. Although such observations implied the potential of designing novel metal/ceramic composites with improved mechanical properties such as high hardness and enhanced ductility, there is not much quantitative data available on the characterization of interfacial mechanical response of metal/ceramic

systems and the processes to achieve desirable interfacial properties continues to depend on trial and error [25].

### 1.1.2 Experimental tools to study metal/ceramic interfaces

A number of experimental techniques have been utilized to explore the atomic and electronic structure of the interfaces. High resolution transmission electron microscopy (HR-TEM) [31] can probe the atomic structure of the interfaces up to 0.02 nm accuracy [6]. The atom probe field-ion microscopy can perform atomic scale studies of segregation at metal ceramic interfaces [32] and electron-energy loss spectroscopy (EELS) [33] can probe their chemical structure to almost atomic resolution. In situ mechanical straining techniques, in either scanning electron microscopy (SEM) or TEM, with the micromechanical testing samples machined using focused ion beam (FIB), is one of the more recently developed tools for studying the mechanical properties of different metal/ceramic interfaces [34,35]. Nanoindentation is another experimental method used to study a number of mechanical properties such as adhesion, hardness, wear resistance and fracture in metal/ceramic systems [36–43]. Novel insights into the interfacial structure and chemistry were provided due to the improvements in the experimental characterization techniques [3].

Experimental techniques such as axial compression loading of micropillar specimens containing metal/ceramic interfacial regions, fabricated with focused ion beam micro/nano scale machining, have been utilized to provide some quantitative data, such as the average critical shear stress, for the mechanical failure of metal/ceramic interfaces [44]. Specifically, a recent experimental study provided details on the mechanical failure of Cr/CrN [45], Cu/CrN and Ti/CrN interfaces under shear loading [21]. The addition of a Cr

metal interlayer between CrN (or TiN) and the underlying substrates, such as stainless steel or Ti6Al4V alloys [29,46,47] has been shown to improve their strength and stability by reducing the stress between the ceramic and the substrate. Additionally, the presence of Cr interlayers has been found to improve the corrosion and wear resistance [48–51], and the high-temperature oxidation resistance of different alloys [52,53].

The presence of MDNs has also been confirmed by a number of experimental studies [54–56]. The atomic arrangement of MDNs has been observed using high resolution electron microscopy [57,58]. Still, the interfacial behavior of metal/ceramic systems at the atomic level is unclear. Most of the experimental studies focused on the static characteristics of MDNs while the motion of MDNs in interface dynamics is still challenging to be studied experimentally [24]. Computational techniques such as first-principles density functional theory (DFT) and Molecular Dynamics (MD) simulations can be an alternative for direct observations and quantitative predictions of the atomic structure of MDNs. Combining the experimental methods with multiscale modeling and simulation techniques can provide better atomic-level insights that are verified by experimental measurements.

## **1.2 Atomistic level simulations**

### **1.2.1. Density Functional Theory (DFT)**

A number of computational methodologies have been developed over the past two decades to study and design materials with desired properties [59]. Among various atomistic simulations techniques, DFT is an attractive choice due to its flexibility in studying a large array of systems without the need for parameterizing atomic models. DFT treats the system under study in a quantum mechanical manner and helps in understanding

the chemistry between metal/ceramic interfaces. Also, it can provide a detailed understanding of the factors that contribute to interfacial strength and stability.

A large amount of research has been carried out to study a number of metal/ceramic systems [16,23,31,32,60] using the DFT method. Many DFT studies focused on the investigation of work of adhesion (WoA) of metal/ceramic interfaces [61,62], interface-driven twinning [63], phase transitions [64,65] and tensile or shear strength of the interface [66,67]. A number of DFT studies have also been performed to study the interfacial energy and electronic structure [68], interfacial adhesion [69–72], and stability of metal/ceramic interfaces [73]. Using DFT, it has been possible to calculate the equilibrium crystal structures [74], cohesive energies [75], lattice parameters [76], elastic moduli [77], and phase diagrams of crystalline solids [78].

A recent study on the Al/TiN and Al/VN metal-nitride interfaces using the DFT calculations [79] revealed an unusual phenomenon of interfacial structural modifications due to the influence of interface chemistry, while no such structural modifications at Pt/TiN and Pt/VN interfaces were observed. The structural modification can be explained on the basis of the metal-N affinity at the interface. The presence of nitrogen (N) atoms at interfaces changes the generalized stacking fault energy (GSFE) landscape (the GSFE is the measure of the energy differences as a function of displacement in a particular slip direction between two adjacent planes [80]) of Al layers nearby the interface in a significant way because of the strong Al-N affinity at the interface. Another DFT calculation found that resistance to shear was highest for Cr/TiN in comparison to many other metal/ceramic combinations [81]. In addition, the weakest plane for Cr with ceramics was observed to be

the chemical interface. This was attributed to Cr/TiN having the lowest overall GSFs near the interface of the systems studied [81].

DFT, however, has a number of limitations. It is limited to relatively small system sizes and time-scales [82]. Mechanical properties and strength usually depend on many large-scale phenomena such as defect concentrations, slip behavior of dislocations, dislocation dipoles at metal/ceramic interfaces and defect dynamics. These are not yet predictable from DFT theory even for single-phase systems [4]. The study of heterogeneous interfaces becomes even more complicated. High computational cost limits the size of DFT simulation supercell to a few hundred atoms [6].

First principles calculations pose some serious limitations for carrying out realistic simulations of alloy systems. Hence, an alternative is MD simulations that utilize semi-empirical potentials and can handle systems with more than a million atoms. The structure and properties of the metal/ceramic interfaces can be explored using these MD simulations [83] that have the ability to quantify the mechanisms of the structure-property relationship and statistically predict the material properties. However, lack of accurate empirical potentials for studying metal/ceramic interfaces limits the research to the first principles based DFT methods mostly.

### 1.2.2. Molecular dynamics (MD) simulations

It is one of the reliable ways to explore the structure and properties of an interface [6]. Zhang *et al.* performed MD simulations and DFT calculations together with the experimental mechanical testing on Ti/TiN interface and observed a weakening effect of the metal/ceramic interface on its adjacent metal atomic monolayers in both shear and tension, parallel and normal to the interface [40]. As a result, the minimum energy and

shear strength of the interface occurred when the MDN was near, but not at the chemical interface. It was speculated by the authors that such failure mode for metal/ceramic interfaces might be, in general, valid for other metal/ceramic systems.

In another work by the same research group [7], it was observed that the average critical shear stress for failure varied significantly on changing the type of metal interlayer from Cu to Ti and Cr. The Cr interlayers exhibited the highest critical shear stress among the three metals followed by Ti. In addition, the interfacial shear strength of the metal/ceramic systems was also observed to be impacted by the presence of dopant atoms. Stronger adhesion and resistance to shear can be acquired by adding small amounts of ‘dopant’ atoms to such metal/ceramic systems. It was observed that the presence of these dopant atoms at the interface can affect the interfacial chemical bond resulting in changing the properties of interface materials.

One of the most important components of MD simulations is the interatomic potential that essentially describes the forces on individual atoms [59]. However, the lack of accurate empirical potentials results in limiting the atomistic level studies of metal/ceramic interfaces to DFT methods. There is a need to develop new interatomic potentials, validated with experiments, to accurately understand the complex behavior at the interfaces. To understand the structure-property relationships of metal/ceramic systems through large scale simulations, reliably parameterized interaction potentials are needed.

### **1.3 Organization of the dissertation**

The dissertation is divided into five chapters. The background and literature review about the metal/ceramics interfacial studies is presented in Chapter 1. A theoretical background of the MEAM formalism and the interatomic potential development for the present work has been discussed in Chapter 2. Chapter 3 discusses the MD studies of various metal/ceramic interfaces. Chapter 4 discusses the deformation mechanism of the doped metal/ceramic interfaces. In the final chapter, the results obtained throughout this work are summarized and future outlook of the work is presented.

## CHAPTER 2

### MEAM INTERATOMIC POTENTIAL

#### 2.1 Second nearest neighbor MEAM potential

As discussed in previous chapter, MD simulation is a powerful tool to study systems with a large number of atoms. In order to employ the MD technique semiempirical atomic potentials are required. For alloys, a potential that can describe various elements with various crystal structures simultaneously is often sought [84].

In this regard, the embedded atom method (EAM) [85–87] is one of the extensively used interatomic potential models to study metals, covalent materials as well as the materials with impurities [59]. EAM was developed in order to investigate the brittle fracture of transition metals in the presence of hydrogen [88]. As the name suggests, this method assumed each atom as embedded in the host lattice consisting of all the other atoms (**Figure 2-1**). This assumption allowed a realistic treatment of impurities in structures with cracks and the calculations involved electron density which is a definable quantity. EAM potentials work better than simple pair-potentials because of the addition of an “embedding energy” term involving the physics of coordination dependent bond strengths [82]. They have been utilized for a number of metals and alloys for their bulk and interfacial studies. However, EAM potentials have a number of limitations such as in case of the systems

where directional bonding is important such as in semiconductors and elements from the middle of the transition metal series [89].

The modified EAM (MEAM) method [90] introduced by Baskes [35–38] extended the embedded atom method proposed by Daw and Baskes [39,40] so that the directionality of bonding in materials is considered. It was introduced originally to provide improved description of shear in silicon [82].

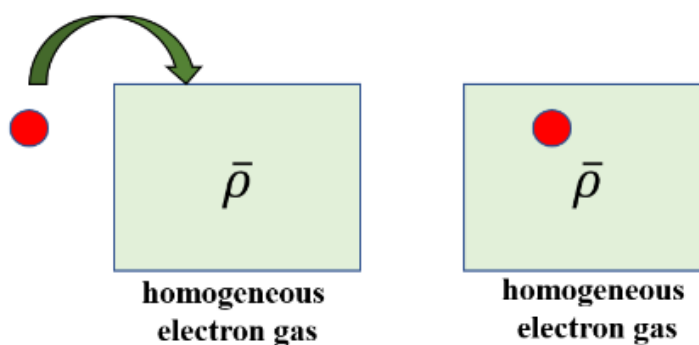


**Figure 2-1:** Atom embedded into homogeneous electron gas

MEAM potential has been developed for different crystal structures including *fcc*, *bcc*, and *hcp* [91–94], binary [95–99] as well as ternary [98,100–102] combinations of various crystal structures along with different ceramics, such as TiN and CrN [103–105]. For metal/ceramic mixed material systems in particular, the atomic potentials of various elements having different crystal structures must be described using the same formalism. In this respect, the MEAM potential can be utilized since it can reproduce physical properties of metals with various crystal structures (*fcc*, *bcc*, *hcp*, diamond and even gaseous elements) using the same formalism and functional form [31]. The MEAM potential has been utilized to perform MD simulations on various metal/ceramic systems to study their mechanical behavior under varying loading conditions [106–108].

Simulations with the MEAM model have also been shown to work efficiently for large system sizes [109,110].

Also, metal/ceramic interfaces have recently been examined with MEAM potentials, providing information on their interfacial stability, the influence of MDNs, and shear strength [111]. The original MEAM considers only nearest-neighbor interactions, and a many-body screening function is used to take into consideration different neighbor interactions. However, for *bcc* crystal structures, using MEAM, the surface energy of the (111) surface was calculated to be smaller than for the (100) [112] which was contrary to experimental results. Also, there is only about 15% difference between the first nearest-neighbor and the second nearest-neighbor distance [112] and hence the interactions between second nearest-neighbor atoms must be considered.

In the second nearest neighbor MEAM (2NN-MEAM), the many-body screening function is adjusted so that is able to consider the second nearest-neighbor interactions [38]. In addition, a radial cutoff function is applied to reduce calculation time [95]. Hence, the 2NN-MEAM potential provides higher reliability than the EAM in treating metal/ceramic systems. By taking into consideration the second nearest neighbor interactions, a number of problems such as structural instability, the phase transitions, or incorrect surface reconstructions on thin films were also resolved for *fcc* elements.

Using the 2NN-MEAM model, the deformation mechanism of a number of metal/nitrides and metal/carbides were investigated [108,113]. Recently, MD simulations were used to study the plastic deformation mechanisms in Nb/NbC [39] and Ti/TiN [40] using the MEAM potential and focused on the mechanical responses of interfaces under different loading conditions.

The MEAM interatomic potential was used by Yang *et al.* for the interfacial study of Ti/TiN metal/ceramic system, using MD simulations, in order to understand its deformation behavior under compressive loading [41]. The interfacial structure was analyzed using atomically informed Frank-Bilby theory [114]. Upon compression, contrary to the stress-strain response usually observed in metals and metal/ceramics where generally two peaks (known as yield points) are observed, their work showed three distinct peaks with each peak related to a distinct deformation mechanism. The first peak was created due to the dissociation of a perfect dislocation into pairs of partial dislocations around extended node regions at the interface. Upon further compression, the second peak, termed as the first yielding, resulted from the slip transfer to the Ti layer. Finally, a third peak termed as the second yielding, was observed when the dislocation transmitted into the TiN layer.

The original MEAM formalism involved a particular reference structure for which the Rose equation [115] was obeyed which might not work for other structures. A new MEAM model called reference free (RF-MEAM) was developed for silicon [116] in which the reference structure was no longer required, and the pair-potential could be optimized freely. It was found to be more convenient, flexible, and turned out to be superior to the standard MEAM.

## 2.2 MEAM potential formalism

The details of the MEAM formalism have been reported in the literature [84,117], and an overview is presented here. The total energy of a system is the sum of an embedding function,  $F_i$ , and a pair interaction,  $\varphi_{ij}(R_{ij})$  between atoms  $i$  and  $j$  separated by a distance  $R_{ij}$ ,

$$E_{\text{total}} = \sum_i \left[ F_i(\bar{\rho}_i) + \frac{1}{2} \sum_{j \neq i} S_{ij} \varphi_{ij}(R_{ij}) \right] \quad (2.1)$$

$$F(\bar{\rho}) = A E_c (\bar{\rho} / \bar{\rho}^0) \ln(\bar{\rho} / \bar{\rho}^0) \quad (2.2)$$

where the sums are over the atoms  $i$  and  $j$ . The embedding function  $F_i$  is the energy to embed an atom of type  $i$  into the background electron density at site  $i$ ,  $\bar{\rho}_i$ .  $A$  is an adjustable parameter,  $E_c$  is the cohesive or the sublimation energy, and  $\bar{\rho}^0$  is the background electron density for a reference structure. The reference structure is the one where the individual atoms lie on the exact lattice points. In general, the equilibrium structure is taken as the reference structure for elements. The background electron density  $\bar{\rho}$  at the atomic site  $i$  is computed by combining the partial electron density terms for different angular contributions [93] with weight factors  $r^{(h)}$  ( $h=1-3$ ). It consists of spherically symmetric electron density and the angular contributions.  $S_{ij}$ , as given in equation (2.1), is a three-body screening factor that denotes the effect of the position of a third atom,  $k$ , (**Figure 2-2**) on the interaction between atoms  $i$  and  $j$ , which is limited by  $C_{\min}$  ( $S_{ij}=0$ ) and  $C_{\max}$  ( $S_{ij}=1$ ) [112]. For energy calculations, the functional forms of  $F_i$  and  $\varphi_{ij}$  should be given.

During the atomistic simulations, the energy is calculated using the expression on the right-hand side of equation (2.1). The way of combining the partial electron densities is not unique and several expressions for combining the partial electron densities have been proposed [118]. Among them, the following form has been widely used, including in the present work:

$$\bar{\rho}_i = \rho_i^{(0)} G(\Gamma) \quad (2.3)$$

where

$$G(\Gamma) = 2 / (1 + e^{-\Gamma}) \quad (2.4)$$

$$\Gamma = \sum_{h=1}^3 t_i^{(h)} \left[ \rho_i^{(h)} / \rho_i^{(0)} \right]^2 \quad (2.5)$$

$t_i^{(h)}$  are the weight factors. The atomic electron density is given as

$$\rho_j^{(h)}(R) = \rho_0 e^{-\beta^{(h)} \left( \frac{R}{r_e} - 1 \right)} \quad (2.6)$$

which involves the adjustable parameters  $\beta^{(0)}$ ,  $\beta^{(1)}$ ,  $\beta^{(2)}$ ,  $\beta^{(3)}$  (the decay lengths) and  $r_e$ , the nearest neighbor distance in the equilibrium reference structure. The total energy per atom for a given reference structure is evaluated from the zero-temperature universal equation of state by Rose *et al.* [115] as a function of nearest neighbor distance  $R$ ,

$$F[\bar{\rho}^0(R)] + \frac{1}{2} \sum \phi(R) = E^u(R) = -E_c(1 + a^*)e^{-a^*} \quad (2.7)$$

where

$$a^* = \alpha \left( \frac{R}{r_e} - 1 \right) \quad (2.8)$$

and  $\alpha$  is an adjustable parameter that includes contributions from the bulk modulus, cohesive energy, and equilibrium atomic volume. The pair interaction is then calculated from the total energy per atom and the embedding energy as a function of the nearest neighbor distance.

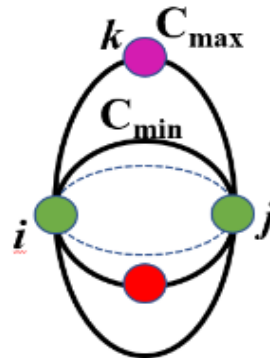


**Figure 2-2:** The values of  $C_{\max}$  and  $C_{\min}$  are adjusted to control the second nearest neighbor interaction

### 2.3. Minimization and genetic algorithm

An in-house Python code [119] will be used for the optimization of a set of MEAM parameters,  $\{\xi\}$ , as outlined in **Figure 2-3**. The code worked by minimizing the mean square displacement between the calculated and experimental/DFT derived properties. In particular for pure metals, the MEAM parameters were optimized to experimentally and DFT derived elastic constants ( $C_{ij}$ ), monovacancy formation energies ( $E_{\text{defect}}$ ), surface energies ( $E_{\text{surf}}$ ), ratios of the cohesive energy of different crystal structures, and solid densities.

For pure metal systems, there are 11 MEAM parameters to be optimized. For the optimization procedure, one random MEAM parameter  $\xi_i$  is chosen, and four different trials are generated using a maximum displacement,  $\Delta_i$  to  $\xi_i$ . ( $\xi_i - \Delta_i$ ,  $\xi_i - \Delta_i/2$ ,  $\xi_i + \Delta_i/2$  and  $\xi_i + \Delta_i$  (' $i$ ' is over all the eleven parameters)). The different physical properties are calculated using these four different trial values and are compared with the DFT/experimental results. A mean-squared deviation of the value of a specific property is calculated for each trial

$$\sigma_i = \sum_j w_j (p_j^i - p_j^{\text{DFT/expt}})^2 \quad (2.9)$$

where the sum ' $j$ ' is over all the properties and  $w_j$  is the weight assigned to each property. The trial with the smallest mean squared deviation is chosen and the process is repeated for the next MEAM parameter.

The minimization method, however, does not span a large array of parameter  $\xi$  values and similar properties can be reproduced with different  $\xi$  values. To account for this, the minimization cycle is coupled to a genetic algorithm as described in **Figure 2-3(b)** to obtain optimal  $\xi$  values. The genetic algorithm expands the domain of search for the most

optimal MEAM parameters, increasing it to six different sets. These six sets are optimized simultaneously. Out of the six sets,  $s_1, s_2, s_3, s_4, s_5$  and  $s_6$ , some are taken from models existing in literature and some are randomly generated. For each set, the minimization cycle is carried out for 50 cycles and optimized  $\xi$  parameters are obtained. The set with the smallest  $\sigma$  value as given in equation (2.9) is chosen as  $s_{\min}$ . After every 50 cycles, the parameter sets with  $\sigma$  values greater than  $10 \times \sigma_{\min}$  are destroyed. The destroyed sets are then replaced by new ones, which are created by mating the surviving sets. The mating is done by averaging the parameter values of the two sets. In general, the most optimum parameter set may be obtained after 20 genetic algorithms or about 1000 minimization cycles.

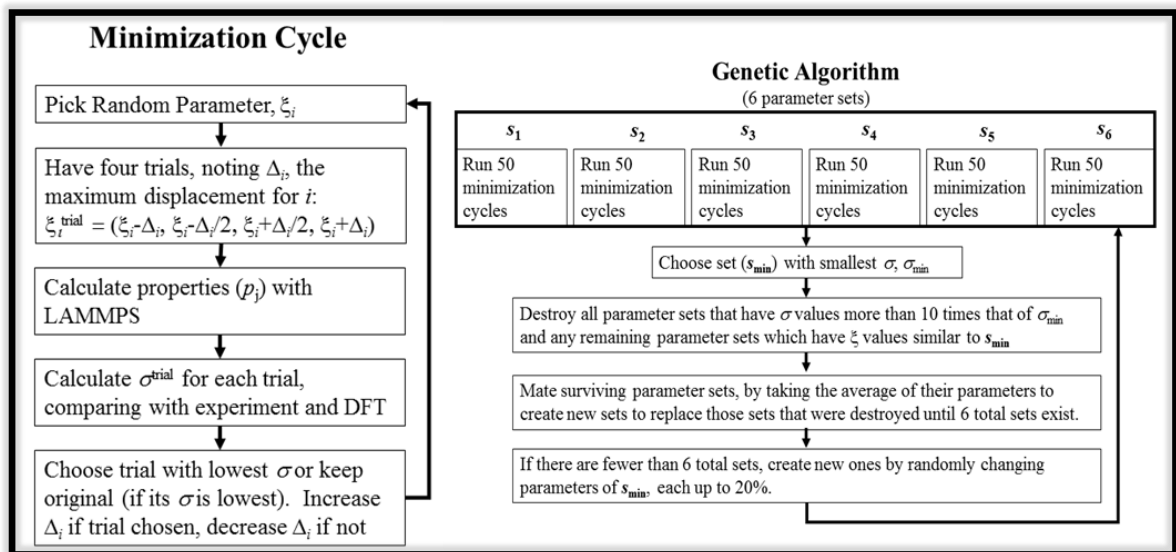


**Figure 2-3:** Parameter Optimization Procedure for the MEAM potential [119] (b) Genetic Algorithm for simultaneous optimization of MEAM parameter.

## CHAPTER 3

### MD STUDY OF METAL/CERAMIC INTERFACES

#### 3.1 Cr/TiN metal/ceramic system

In one of the previous works, a MEAM potential was developed to study Ti/TiN and Cu/TiN interfaces [120]. The potential model was utilized to perform MD simulations in order to understand the MDN structure and their effect on the mechanical response of Ti/TiN and Cu/TiN interfacial systems. It was observed that the stable Ti/TiN systems were obtained when the MDN was away from the interface. For Cu/TiN, the most stable system consisted of MDN at the interface. Based on the previous study of the effect of the MDNs on the mechanical response of Ti/TiN and Cu/TiN interfaces [121], this part of the research is aimed at developing a new interatomic potential for the interaction of Cr with TiN and studying its interfacial properties in the presence of MDNs. While a considerable amount of work has been done on the study of *fcc* metal/TiN [67,122] and *hcp* metal/TiN interfaces [29,121,123,124], to our knowledge, no previous work has studied the interfacial behavior of the *bcc* metal/NaCl-type TiN interface. The research represents the development of a new Cr/TiN MEAM model, and the investigation into the role of the presence and location of MDNs on its shear strength.

For a single element, once the reference structure is defined, including its  $E_c$  and  $r_e$ , which are set to experiment, 11 remaining MEAM parameters need to be determined:  $\beta^{(0)}$ ,  $\beta^{(1)}$ ,  $\beta^{(2)}$ ,  $\beta^{(3)}$ ,  $t^{(1)}$ ,  $t^{(2)}$ ,  $t^{(3)}$ ,  $A$ ,  $\alpha$ ,  $C_{\min}$ , and  $C_{\max}$ . The values for the MEAM parameters for N were taken from the literature without any modification [105]. The reference structures for Ti and Cr are *hcp* and *bcc*, respectively. This requires fitting eleven additional parameters for the binary systems. These include the  $E_c$  between them in equation (2.2), along with their  $\alpha$  and  $r_e$  values in equation (2.8). The remaining eight parameters are their  $C_{\min}$  and  $C_{\max}$  values. For ternary interactions, an additional six parameters, three  $C_{\min}$  and three  $C_{\max}$ , need to be fit. For Ti and TiN, we used the previously developed model designed to study the Ti/TiN interface [121]. We parameterized a model for pure Cr, along with a model for CrN, Cr<sub>2</sub>Ti [125,126] and Cr/TiN interface. A model for CrN was recently developed by Ding *et al* [103], while no model for the CrTi binary system is currently available to the best of our knowledge.

## 3.2 General details

### 3.2.1 DFT calculations

The surface and interfacial properties were extracted from a combination of experimental measurements and DFT calculations. We carried out the DFT calculations in most cases, even if values existed in the literature. The Vienna ab initio simulation package (VASP) [127] was utilized for the DFT calculations using the Perdew, Burke, and Ernzerhof (PBE) generalized gradient approximation for the exchange-correlation functional [128]. The potential due to the core electrons was accounted for by the projector augmented wave method [129], which combines the features of the pseudopotential approach and the linear augmented plane wave method. Kohn-Sham orbitals for valence

electrons were expanded in terms of a plane wave basis set with a cutoff energy of 400 eV. The Monkhorst-Pack scheme was used for sampling the k-point of the plane wave basis in the first Brillouin zone [130]. The specific k-point mesh size depended on the system size and the calculation being carried out.

For pure Cr, the monovacancy formation energy, surface energies, and the GSFEs were calculated using first-principles DFT. In order to calculate the monovacancy formation energy, the Brillouin zone was sampled using  $3 \times 3 \times 3$  mesh of k-points for the 128-atom cells. The surface energies were calculated for the surfaces Cr(001), Cr(110), and Cr(111) with the system sizes of 54, 72, and 48 atoms respectively and the Brillouin zone was sampled using  $4 \times 4 \times 1$  k-point mesh. For each of these surfaces, a periodic system with a 15 Å of vacuum was created, resulting in the formation of two surfaces.

The GSFE surface was calculated for the Cr(001) system. For this calculation, half of the atoms were displaced in the X[110] and Y[ $\bar{1}$ 10] directions, keeping the other half of atoms fixed as had been done previously [81] (**Figure 3-1b**). A total of ten positions along X and ten along the Y directions were sampled, mapping a total of 100 points. For each point, an energy minimization followed their displacement, allowing the atoms to only relax in the Z direction (keeping X and Y positions all fixed). The minimum energy path was then plotted along the X direction after mapping the full GSFEs out [131]. The maximum height of the minimum energy plot gives the energy barrier of the shear displacement of the GSFE surfaces.

For the binary systems, the elastic constants, surface energies, and the enthalpies of mixing were calculated using DFT. The elastic constants were calculated using a system size of 64 atoms for CrN and 24 atoms for Cr<sub>2</sub>Ti with a  $12 \times 12 \times 12$  k-point mesh. To

calculate the enthalpy of mixing, a Cr<sub>2</sub>Ti system of 24 atoms and a CrN system of 32 atoms were used, each with a 4 × 4 × 4 k-point mesh. For the surface energy calculations, 72, 32 and 54 atoms were used for CrN(001), CrN(110) and CrN(111) while 48, 44 and 72 atoms were used for Cr<sub>2</sub>Ti(001), Cr<sub>2</sub>Ti(110) and Cr<sub>2</sub>Ti(111). In each of these systems, 15 Å of vacuum were present normal to the surface in consideration, and a k-point grid of 4 × 4 × 1 was used for all the cases. The impact of spin-polarized calculations was investigated for all the systems, and it was found that they only had a significant impact on the structure and energetics of CrN, so they were used only for CrN.

For Cr/TiN interfaces, the WoA was calculated for a system that consisted of eight layers of four Cr atoms (32 total) along with six layers of eight TiN atoms (48 total) that formed a single interface between Cr(001) and TiN(001). The plane separating Cr and TiN phases was defined as the chemical interface. The interface was perpendicular to the Z-direction in a cell of approximate dimensions of 5.88 × 5.88 × 40.22 Å. As with the previous work [81], there was 15 Å of vacuum present along the Z direction to assure that only one interface was formed in between Cr and TiN. The WoA for the Cr/TiN interface was calculated as done previously [132]:

$$\text{WoA} = (E_{\text{Cr}} + E_{\text{TiN}} - E_{\text{Cr/TiN}})/A \quad (3.1)$$

where  $E_{\text{Cr/TiN}}$  is the energy of the entire system, and  $E_{\text{Cr}}$  is the energy of the Cr(001) system optimized in both atomic positions and cell coordinates.  $E_{\text{TiN}}$  is the energy of an optimized TiN(001) system, and  $A$  is the area of the Cr/TiN interface.

For the GSFE surface of the Cr/TiN system, the configuration was the same as for the WoA, and it was calculated at the chemical interface between the Cr(001) phase and the TiN(001) phase. This was denoted as  $P = 0$  (**Figure 3-1a**). The GSFE surface was also

calculated for the P=1 layer, which was in between the TiN(001) phase with one Cr(001) layer (4 additional atoms) and the remaining eleven Cr(001) layers (44 atoms). The GSFE surface for Cr/TiN was mapped out using the procedure described above, i.e., by displacing all the atoms above the planes P=0 or P=1 from one lattice point to another equivalent lattice point along the X[110] and Y[ $\bar{1}$ 10] directions (**Figure 3-1b**), keeping the positions of all the atoms below those planes fixed, followed by relaxation along the Z direction.

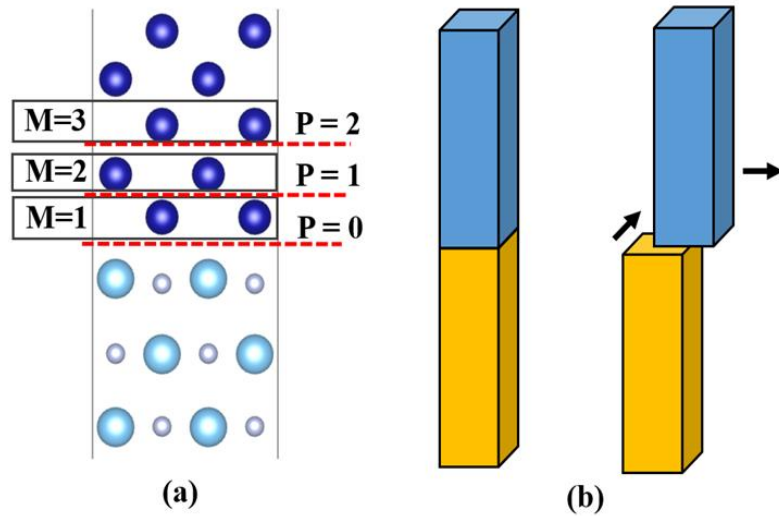


**Figure 3-1:** (a) Cr(001)/TiN(001) structure with the atomic layers denoted by M and the interlayer planes denoted by P, (b) Schematic of the shear displacements for calculating the GSFE surface of the Cr/TiN metal/ceramic system.

### 3.2.2 Calculation of Properties from the MEAM Model

All the MEAM properties were calculated using the LAMMPS simulation software [133]. For Cr, the lattice parameters, ratios of the energy of different crystal structures ( $E_{fcc}/E_{bcc}$ ) and ( $E_{hcp}/E_{bcc}$ ), surface energies ( $E_s$ ) of various surfaces Cr(001), Cr(110), Cr(111), solid density ( $\rho_s$ ), elastic constants, and monovacancy formation energy ( $E_{vac}$ ) were calculated [119]. For all calculations except the solid density, energy minimizations were carried out with the conjugate gradient method. The *fcc* structure had 32 atoms, the

hcp structure had 48 atoms, and the *bcc* structure had 54 atoms. To calculate the monovacancy formation energy for Cr, one atom was removed from the bcc system of 128 atoms. The elastic constant calculations were carried out for the bcc system with 54 atoms, and systems with 54, 72, and 48 atoms were used for the calculation of surface energies of Cr(001), Cr(110), and Cr(111) surfaces, respectively.

To calculate the solid density for Cr metal, 20 ps of NPT simulations of a system with 432 atoms were carried out at 298 K and 1 atm using the Nosè-Hoover thermostat and barostat [134,135] with a timestep of 1 fs. For binary systems, the enthalpy of mixing and WoA were calculated for CrN and Cr<sub>2</sub>Ti. The enthalpy of mixing was calculated using a system of 192 atoms for CrN, and a system of 216 atoms for Cr<sub>2</sub>Ti. The surface energies were calculated using a system size of 108 atoms for CrN(001), 144 atoms for both CrN(110) and CrN(111) surfaces, 48 atoms for Cr<sub>2</sub>Ti (001), 44 atoms for Cr<sub>2</sub>Ti (110), and 72 atoms for the Cr<sub>2</sub>Ti (111) surface. The elastic constants, GSFE, and WoA were calculated using the same system sizes as used in DFT calculations described in Section 3.2.1.

The Baker-Nutting orientation relationship [136]—with  $[100]_{\text{NaCl}} \parallel [110]_{\text{bcc}}$  along the X axis,  $[010]_{\text{NaCl}} \parallel [\bar{1}10]_{\text{bcc}}$  along the Y axis, and  $(001)_{\text{NaCl}} \parallel (001)_{\text{bcc}}$  along the Z axis—was adopted between the rock salt (B1) structured TiN and bcc Cr (Error! Reference source not found.). The interface was parallel to the X-Y plane, with each dimension close to 7.5 nm in the initial structures. The total thickness in the Z direction was approximately 10 nm, with 6 nm of Cr and 4 nm of TiN present. The first Cr layer next to this interface was denoted by M=1, the second layer by M=2, and so on (Error! Reference source not found.). The equilibrium interfacial structure was obtained by an initial relaxation followed by an

iterative conjugate-gradient stress-relief treatment [34]. The preliminary relaxation was carried out through an NVT equilibration at 10 K for 50 ps in which the top and the bottom two layers in the Z direction were fixed. The iterative stress-relief treatment was conducted to adjust the magnitude of the normal stress components to be less than 100 Pa.

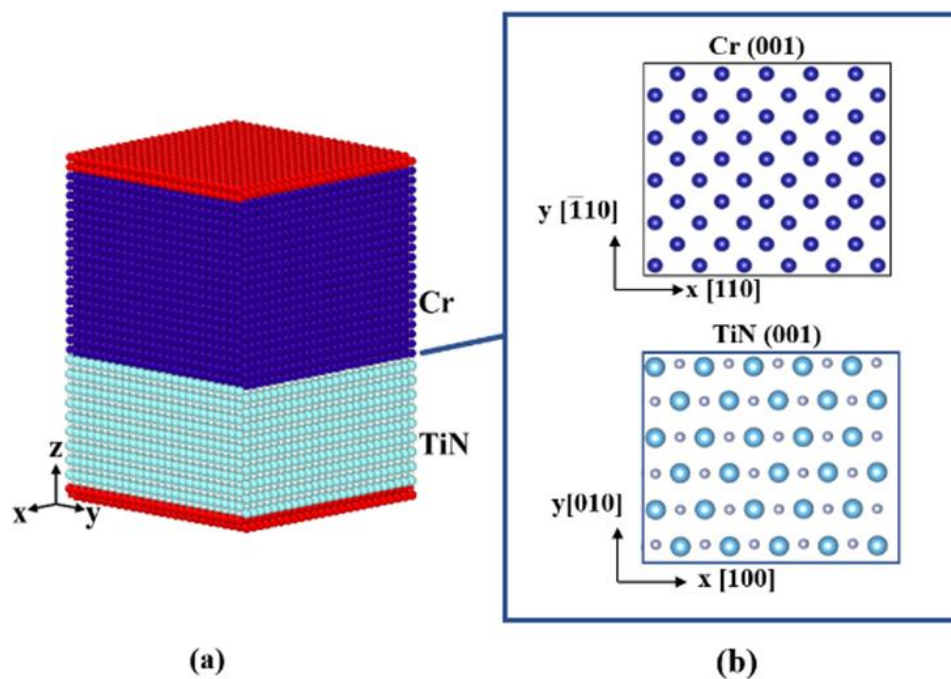


**Figure 3-2:** (a) Cr(001)/TiN(001) structure (b) orientation relationship in Cr/TiN multilayers. The top and the bottom red colored regions are the fixed atoms.

### 3.3 Results and discussion

#### 3.3.1 Pure Cr metal

**Table 3-1** shows the newly determined MEAM parameter values for Cr, along with the MEAM parameter values used for this work for Ti [121] and N [105] taken from the literature. The values for  $E_c$  and  $r_e$  for Cr were taken from the experimental values in the literature [137,138]. The experimental/DFT and the MEAM calculated values of the various properties of Cr using the present model, as well as Lee's model [139], are listed in **Table 3-2**. The Lee model underestimated the GSFE barriers for Cr(001) to a moderate degree. The minimum energy path on these GSFEs plotted as a function of position along the X axis is shown in **Figure 3-3**. For this system, the path ended up as simply the energy at  $Y=0$  as a function of X since the minimum energy path is parallel to the X axis. The GSFE barrier and the minimum energy path for Cr(110) has been shown in **Figure A-1**. Even in that case, our model reproduces the DFT result fairly well as compared to Lee's model.

**Table 3-1:** MEAM potential parameter sets for pure Cr, Ti, and N.

	$E_c$	$r_e$	$A$	$\alpha$	$\beta^{(0)}$	$\beta^{(1)}$	$\beta^{(2)}$	$\beta^{(3)}$	$t^{(1)}$	$t^{(2)}$	$t^{(3)}$	$C_{\min}$	$C_{\max}$
	(eV)	(Å)											
<b>Cr</b>	4.10 <sup>a</sup>	2.88 <sup>b</sup>	0.28	5.70	8.74	0.01	5.48	0.37	1.06	11.09	-7.73	0.75	2.36
<b>Ti<sup>a</sup></b>	4.87	2.92	1.19	4.41	1.58	0.08	2.89	0.0016	5.55	6.79	-2.05	0.89	2.85
<b>N<sup>a</sup></b>	4.88	1.10	1.80	5.96	2.75	4.00	4.00	4.00	0.05	1.00	0.00	2.00	2.80

<sup>a</sup>Reference [121]

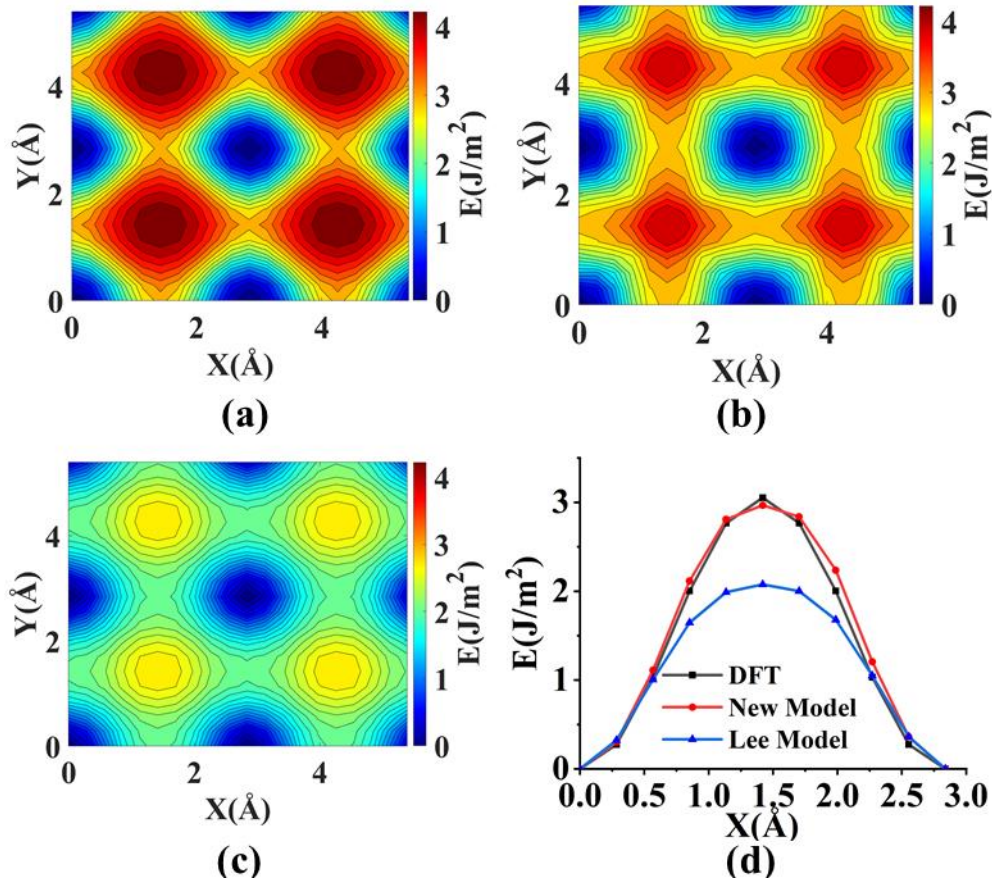


**Figure 3-3:** GSFEs of Cr(001) calculated using (a) DFT, (b) new model (c) Lee model [139] (d) Comparison of minimum energy path of the GSFE for Cr(001).

The new model, again, reproduced the DFT barrier height in the minimum energy pathway with good accuracy, while the Lee model underestimated it by around 30%.

### 3.3.2 Mixed systems

The binary parameters for Cr-Ti and Cr-N were fit to several properties, including enthalpies of mixing, elastic constants, and surface energies. **Table 3-3** shows the values of the binary parameters obtained in the present work and Ti-N binary parameters from the previous work by Miraz *et al.* [121].

**Table 3-2:** Comparison of the DFT calculated/experimental properties of Cr with values obtained from the MEAM model.

Property	DFT/expt. value	New model	Lee model [139]
$E_{\text{vac}}$ (eV)	2.57 <sup>a</sup> , 2.27 <sup>b</sup>	3.17	1.95
$E_s$ (001) (J/m <sup>2</sup> )	2.50 <sup>a</sup>	2.85	2.39
$E_s$ (110) (J/m <sup>2</sup> )	2.34 <sup>a</sup> , 2.35 <sup>c</sup>	2.69	2.26
$E_s$ (111) (J/m <sup>2</sup> )	2.60 <sup>a</sup>	3.07	2.44
Elastic constants (GPa)			
$C_{11}$	391.0 <sup>d</sup>	455.91	344.40
$C_{12}$	89.60 <sup>d</sup>	69.76	112.80
$C_{44}$	103.20 <sup>d</sup>	112.11	130.40
$\rho_s$ (g/cm <sup>3</sup> )	7.15 <sup>e</sup>	7.28	7.25
$E_{\text{fcc}}/E_{\text{bcc}}$	0.96 <sup>a</sup>	0.92	0.97
$E_{\text{hcp}}/E_{\text{bcc}}$	0.95 <sup>a</sup>	0.93	0.98

<sup>a</sup>DFT as calculated in this work.

<sup>b</sup>Reference [140]

<sup>c</sup>Reference [141]

<sup>d</sup>Reference [142]

<sup>e</sup>Reference [143]

It is observed from **Table 3-3** that some  $C_{\text{max}}$  values were larger than 2.8. This is due to the fact that the electronic structure of Cr and Ti atoms is altered in the vicinity of one another resulting in charge transfer. A charge-transfer modified embedded atom method (CT-MEAM) has been developed [102,144] which can overcome the limitation of conventional fixed charge potential method. However, this model is computationally far more expensive than the traditional MEAM model, which only considers the short-range metallic/covalent interactions. The charge transfer interactions are taken care of implicitly to a degree by the large  $C_{\text{max}}$  that results from the current parameterization. Other researchers have also reported cases where  $C_{\text{max}} > 2.8$  has been used [100].

**Table 3-3:** MEAM potential parameters for the binary systems (x-y). In any pair, the first element is denoted by x, and the second element is denoted by y.

Parameters	(x-y) pair		
	Cr-N	Cr-Ti	Ti-N <sup>a</sup>
Reference state	b1	b1	b1
$E_c(x, y)$ (eV)	5.5269	2.9859	6.6139
$r_e(x, y)$ (Å)	2.1069	2.6952	2.1195
$\alpha(x, y)$	6.9415	7.3082	4.7225
$C_{min}(x, x, y)$	0.08	2.0	0.4263
$C_{min}(y, y, x)$	1.4265	1.88	1.0733
$C_{min}(x, y, x)$	1.7054	0.22	1.5
$C_{min}(x, y, y)$	1.75	1.2036	1.5
$C_{max}(x, x, y)$	2.18	3.4196	2.0328
$C_{max}(y, y, x)$	3.814	3.2941	1.7998
$C_{max}(x, y, x)$	2.891	2.0	2.4073
$C_{max}(x, y, y)$	4.0	2.198	2.3557

<sup>a</sup>Reference [121]

**Table 3-4:** MEAM potential parameters for the Cr/TiN ternary system

Parameters	Value
$C_{min}(\text{Cr, N, Ti})$	1.9376
$C_{min}(\text{Cr, Ti, N})$	0.9440
$C_{min}(\text{N, Ti, Cr})$	0.7918
$C_{max}(\text{Cr, N, Ti})$	3.8510
$C_{max}(\text{Cr, Ti, N})$	3.6540
$C_{max}(\text{N, Ti, Cr})$	3.1064

The parameters for the ternary Cr/TiN system are shown in **Table 3-4**. The NaCl-type CrN and TiN (space group  $Fm\bar{3}m$ ) were chosen as reference structures for the Cr-N and Ti-N binary systems. Since the  $\text{Cr}_2\text{Ti}$  (space group  $Fd\bar{3}m$ ) structure cannot be used as a reference for the MEAM packages in LAMMPS, an NaCl type CrTi reference structure was chosen. Despite choosing a different reference structure, we parameterized the Cr-Ti

interactions to reproduce the enthalpy of mixing, elastic constants, and surface energies of  $\text{Cr}_2\text{Ti}$ .

The DFT and the MEAM calculated values of the various physical properties of CrN,  $\text{Cr}_2\text{Ti}$ , and the ternary Cr/TiN systems using the present model are presented in **Table 3-5**. The new model reproduced the target values to a reasonable extent. In particular, the enthalpies of mixing, elastic constants, and the order of stability of the different surfaces compared well for  $\text{Cr}_2\text{Ti}$ .

A MEAM model for CrN was developed by Ding *et al.* [103] (the Ding model in **Table 3-5**), which was parameterized to reproduce elastic constants extracted from CrN thin films [145] and DFT calculations without spin polarization. Because of this focus, the elastic constants calculated with the Ding model were somewhat different in comparison with the new parametrization, which focused on the Cr/TiN interfacial properties. While the surface energies of the new model had the same order as DFT, their magnitudes are consistently underestimated. The reason that a better agreement with the surface energies was not achieved is that improving CrN surface energies hindered the agreement with DFT for the WoA and GSFE surfaces of the Cr/TiN interface. Since the focus of this work was to model the Cr/TiN interface, a greater weight on the WoA and GSFEs was used than CrN surface energies in evaluating the new MEAM parameters.

**Table 3-5:** Comparison of DFT calculated values of properties of binary CrN and Cr<sub>2</sub>Ti and ternary Cr/TiN with the MEAM fitted values.

Property	System		DFT	MEAM	Ding Model <sup>a</sup>
<b>Enthalpy of mixing</b> $\Delta H_{\text{mix}}$ (eV/atom)	CrN		-1.65 <sup>b</sup>	-1.036	
	Cr <sub>2</sub> Ti		-0.11 <sup>c,d</sup>	-0.109	
<b>Elastic Constants</b> (GPa)	CrN	C <sub>11</sub>	319 <sup>c</sup> , 386 <sup>e</sup>	245	515
		C <sub>12</sub>	117 <sup>c</sup> , 120 <sup>e</sup>	114	62
		C <sub>44</sub>	60 <sup>c</sup> , 111 <sup>e</sup>	103	100
	Cr <sub>2</sub> Ti	C <sub>11</sub>	296 <sup>c</sup> , 287.3 <sup>f</sup>	251	
		C <sub>12</sub>	154.3 <sup>c</sup> , 151.2 <sup>f</sup>	97	
		C <sub>44</sub>	81.6 <sup>c</sup> , 81.1 <sup>f</sup>	58	
<b>Surface energies</b> $E_s$ (J/m <sup>2</sup> )	CrN	CrN(001)	0.8088 <sup>c</sup>	0.3767	1.06
		CrN(110)	1.4602 <sup>c</sup>	0.7438	1.75
		CrN(111)	1.8264 <sup>c</sup>	1.0077	1.92
	Cr <sub>2</sub> Ti	Cr <sub>2</sub> Ti(001)	3.195 <sup>c</sup>	2.4220	
		)	1.436 <sup>c</sup>	1.5549	
		Cr <sub>2</sub> Ti(110)	2.744 <sup>c</sup>	1.7224	
		)			
		Cr <sub>2</sub> Ti(111)			
	)				
<b>WoA</b> (J/m <sup>2</sup> )	Cr/TiN		3.69 <sup>c</sup>	4.75	

<sup>a</sup>Reference [103]<sup>b</sup>Reference [146]<sup>c</sup>DFT calculated in this work.<sup>d</sup>Reference [125]<sup>e</sup>Reference [147]<sup>f</sup>Reference [126]

**Figure 3-4** shows a comparison of the GSFES for the Cr(001)/TiN(001) interface for the P=1 and P=2 planes (see **Figure 3-1** for a description of P) calculated by the new model with the DFT results. While there were some subtle differences in the GSFES surfaces between DFT and the MEAM model, their overall agreement was good. Moreover, the minimum energy path and GSFES barrier heights had good agreement between DFT and

the new MEAM model for both layers studied. For semi-coherent interfaces, smaller GSFE barriers have been shown to lead to larger dislocation core widths (intersection points of MDNs) [81,148], which generally decrease shear strength [149]. Because of these reasons, reproducing GSFEs was one of the main focuses for the parameterization of the new MEAM model.

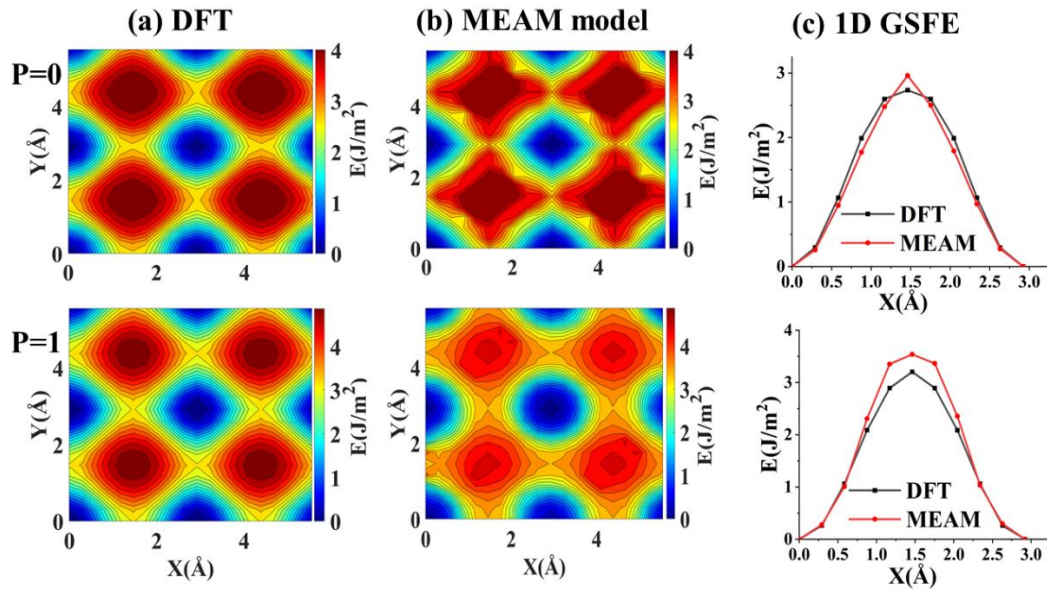


**Figure 3-4:** GSFEs of the Cr/TiN calculated using (a) DFT (b) MEAM for  $P = 0$  and  $P = 1$  planes. (c) A comparison of minimum energy path extracted from the GSFEs for  $P=0$  and  $P=1$ .

### 3.3.3. Stability of Cr/TiN systems

We used large scale MD simulations to study the effect of the MDNs on the mechanical response of the Cr/TiN interfacial system under shear loading. MDNs were accommodated in successive metal layers and their relative energies were calculated to determine how MDN location influences interfacial stability and structure. MDNs were introduced by adding an extra row of atoms in both the X and Y direction in their respective layers. There were 25 atomic rows of TiN in the X and Y directions, and in a coherent

interface between Cr and TiN, the same number of Cr atomic rows were present. For bulk TiN, the X dimension with 25 rows was 74.94 Å, while for bulk Cr, the X dimension was 72.02 Å. Hence, when adding an MDN, there were 26 rows of Cr, giving a bulk Cr X dimension of 74.91 Å, remarkably close to equilibrium TiN. The proximity of each metal layer with respect to the chemical interface was denoted by the letter M, as shown in **Figure 3-1a**. When an MDN was located at a specific M layer, all Cr layers greater than or equal to M had additional Cr rows in the X and Y directions (except when noted otherwise), while those layers less than M (or in between the M layer and TiN) were coherent with the TiN interface. For instance, if the MDN was at the M=1 layer, all Cr layers had additional rows, while for M=4, the M=1-3 layers did not have additional rows and were coherent with the TiN interface.

The open-source software OVITO [150] was used for visualization and analysis. The centrosymmetric parameter (CSP), a measure of the lattice disorder around an atom, was used to characterize local atomic environment [151]. **Figure 3-5** shows atomic structures of the relaxed Cr/TiN interface with MDNs at the M=1, M=2, and M=5 layers in both the X and Y directions. To compare, a system (**Figure 3-5d**) with an MDN only in the X direction at M=1 was also studied. To aid in viewing, the structures are replicated 3 times in the X and Y dimensions in the figures. The atoms are colored according to the CSP values with dark green atoms representing perfect lattice positions, yellow fully off-lattice, and light green in-between [151]. The layer shown is the one with the MDN (top) and all layers between that and the ceramic, along with the ceramic phase. The dislocation cores formed by the MDNs can easily be observed via the yellow bands present with the MDN at M=1 having the largest core width. The network of edge-shaped MDN cores

shown in **Figure 3-5(a-c)** are similar to what was observed for other  $\{001\}$  stacking orientations, such as the Nb/NbC interface [136].

**Figure 3-6** shows the dislocation core width as a function of the position of the MDNs. The core widths were measured by calculating the width of the off-lattice regions that form as observed in **Figure 3-5** (atoms with a CSP  $> 20$  [151]).

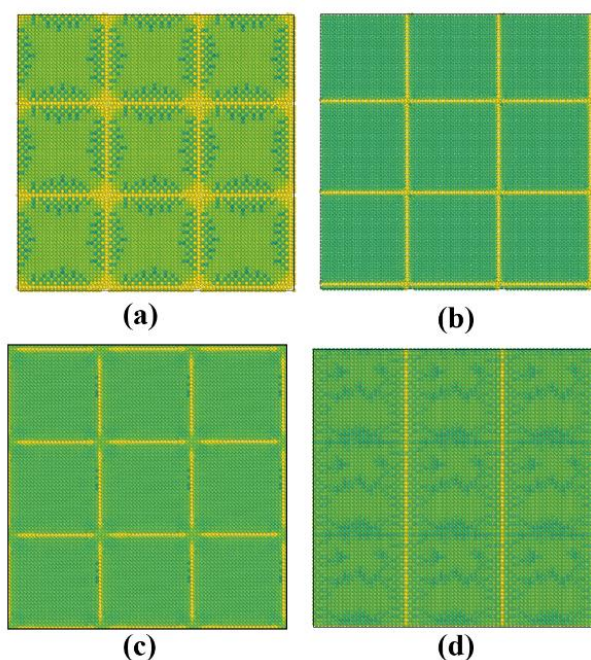


**Figure 3-5:** MDN structure of Cr/TiN system at (a)  $M=1$ , (b)  $M=2$ , and (c)  $M=5$  (d)  $M=1$  (X axis only) layers. Atoms are color-coded according to CSP results.

**Figure 3-5** shows that larger sized nodes are present for the system with MDNs at  $M=1$ , and the node size decreases as the MDNs moves away from the interface with little to no node formation for the system with MDN at  $M = 5$ . The larger width of the dislocation cores for  $M=1$ , which corresponds to semi-coherency at the  $P=0$  plane, is consistent with the fact that the GSFE for  $P=0$  has a lower amplitude than for  $P = 1$  (see **Figure 3-4**) An increase in GSFE barriers corresponds to reduced dislocation core widths, constricting the

nodes at their intersection, which provide stronger pinning points to the motion of MDNs [34].

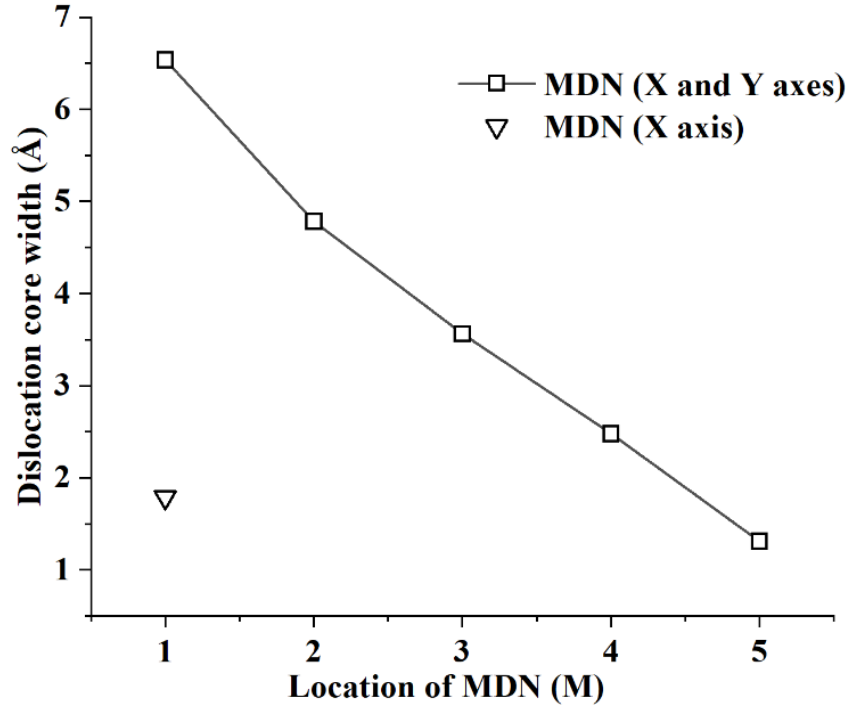


**Figure 3-6:** Dislocation core width with respect to the location of MDN (M).

The interfacial energy ( $\gamma$ ) of the Cr/TiN interface is calculated as follows:

$$\gamma = (E_{\text{interface}} - nE_{\text{Cr}} - mE_{\text{TiN}})/A \quad (3.2)$$

where  $E_{\text{interface}}$  is the total potential energy of the bilayer system,  $A$  is the area of the interface,  $n$  is the number of Cr atoms, and  $m$  is the number of TiN groups.  $E_{\text{Cr}}$  and  $E_{\text{TiN}}$  are the cohesive energies of Cr and TiN, respectively. **Figure 3-7** gives the interfacial energy as a function of the location of the MDNs, where the energy of the fully coherent interface was subtracted from them for comparison.

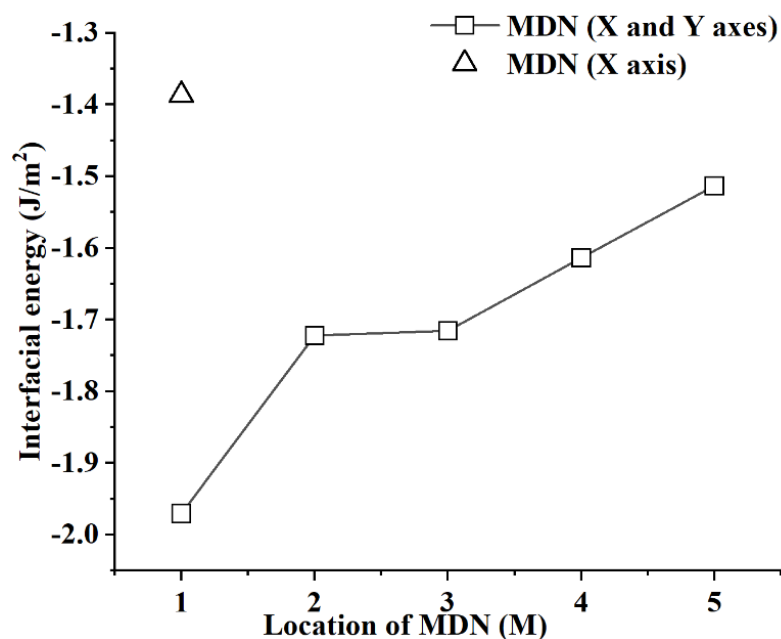


**Figure 3-7:** Plot of the difference in the interfacial energy with respect to the coherent interfacial energy as a function of MDN location (M).

The interfacial energy was found to be dependent on the location of the MDN and was lowest when the MDN was present at the interface due to the lower GSFE barriers at that layer ( $P=0$ ). There was a gradual increase in the interfacial free energy as the location of MDN moved further into the Cr layers. The increase in energy associated with larger M is due to the energy required to strain additional Cr layers to keep it coherent with the TiN surface. The interfacial energy for the configuration with the MDN at M=1 layer along one axis is also shown in **Figure 3-7** and has a value that is significantly closer to the coherent energy than when the MDN is present in two axes at M=1. This was expected as with the MDN in one direction, it more closely represents the higher energy coherent structure than with MDNs in two directions.

### 3.4 Impact of shear on Cr/TiN systems

The relaxed structure was subjected to a shear loading parallel to the interfacial plane in the X direction. **Figure 3-8** shows the variation in the shear strength of the interface as a function of the location of MDNs. All the structures with MDNs displayed much lower yield strength than the coherent interface, which showed a maximum shear stress of 20 GPa. It can be seen from **Figure 3-8** that the maximum shear stress was lowest for the structure with the MDN at the interface (7.2 GPa) and gradually increases as the location of MDN moves away from the interface reaching 15.3 GPa for the MDN at M=5. The shear response of the interface was observed to be related to the dislocation core width. The larger nodes in the M=1 layer (corresponding to the lower GSFE barrier) causes a reduced pinning force and therefore, reduces the shear strength of the interface. Additionally, **Figure 3-8** gives the shear strength when the MDN in the M=1 layer was only in one direction perpendicular to the shear.

It can be observed that the shear strength was moderately higher, 9.3 GPa vs. 7.2 GPa, with the MDN in one direction in comparison with it in both X and Y directions in the M=1 layer. This is expected as the system with MDNs along two directions has much wider core sizes in comparison with the system with MDNs in one direction (see **Figure 3-6**). Another aspect of the M=1 system with MDNs in two directions, is that the nodes that are formed at the intersection of dislocation cores are significantly larger in size than the cores themselves, creating extended regions of local disorder (see **Figure 3-5a**). For the M=5 system, where the cores meet results in a node that is smaller in width than the cores themselves (see **Figure 3-5c**). Overall, the larger regions of local disorder present in

the M=1 layer with MDNs in two directions reduces internal strain reducing its shear strength [34].

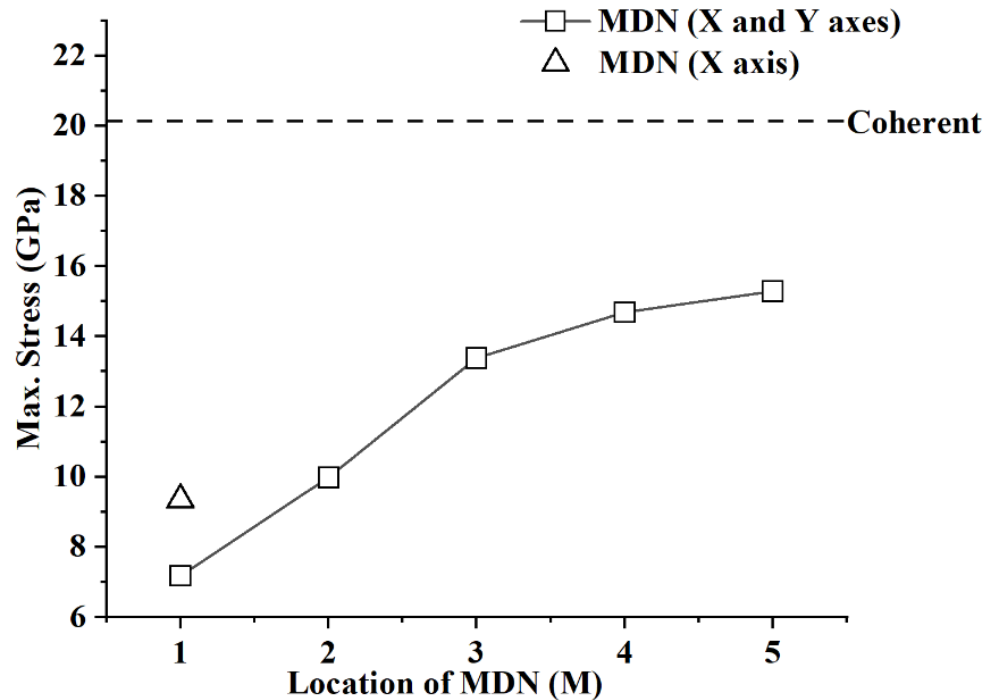


**Figure 3-8:** Plot of interfacial shear strength vs. the location of MDN (M).

Overall, the maximum shear stress was shown to be significantly higher for Cr/TiN than for Ti/TiN and Cu/TiN by the previous work done by Miraz *et al.* [120]. This is consistent with previous experimental results comparing the shear strength of Cr, Cu, and Ti in contact with CrN, which showed highest shear strength for Cr [21]. Furthermore, Cr performed much better than Ti and Mo in wear and friction tests with TiC ceramic [152] due to its higher hardness and better adhesion.

**Figure 3-9** shows a plot of the magnitude of the relative displacement between layers as a function of the number of stress steps as mentioned in Section 2.3.3 for the coherent structure, and configurations with the MDN at the M=1 and M=5 layers. The plots

for the other configurations studied are given in the Appendix A (**Figure A-2**). Each stress step is scaled with respect to the step at which the shear failure occurs (where the shear force drops dramatically) to better compare among the different configurations. A unit value of this scaled stress step represents the initiation of fracture in all cases.

It can be observed that for all configurations, shear failure occurs between the first and second ceramic layers in comparison to the chemical interface. This is different than what was observed at the Ti/TiN and Cu/TiN interfaces [121]. The likely reason for this is due to the different interfacial configuration for TiN in the case of Cr/TiN, in which the TiN(001) surface is in contact with Cr, while the TiN(111) surface is in contact with both Cu and Ti. This is also consistent with the work of adhesion at the Cr (001)/TiN (001) interface, which is  $3.69 \text{ J/m}^2$ , higher than the value of  $1.70 \text{ J/m}^2$ , observed one layer into the ceramic. When the MDN is at the M=5 layer, a weak displacement can be observed between the M=4 and M=5 layers that forms before fracture occurs. Additionally, for the coherent system, there is a small displacement between the chemical interface and the M=1 layer. However, none of these are enough to cause shear failure. The more gradual displacement observed when the MDN is at the M=1 layer as indicated in **Figure 3-9b** hints towards a plastic deformation behavior for that configuration, which will be discussed later.

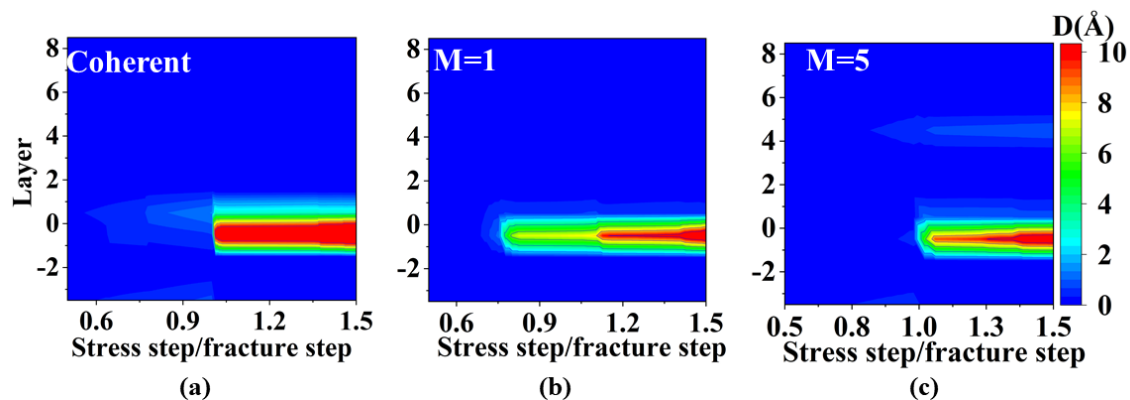


**Figure 3-9:** Plot of the difference in displacement ( $D$ ) per layer per stress step for (a) coherent (b) MDN at  $M=1$  and (c)  $M=5$  layer.

To better illustrate where shear failure occurs, snapshots showing atom positions and their displacements with respect to their equilibrium positions are shown in **Figure 3-10** for the coherent system and for the configuration with MDNs located at the  $M=1$  layer. The displacement arrow magnitudes are set to be consistent within each individual system, but not with respect to one another. It is clear that shear failure occurs in both cases one layer into the ceramic from the Cr/TiN interface, and that under shear, the nitrogen atoms in the top ceramic layer shift towards the Cr metal with respect to the Ti atoms. The shifting that occurs under shear destabilizes the interaction between the first two layers of the TiN phase, causing shear failure to occur. Moreover, this destabilization is present in all MDN patterns we studied, being prevalent enough to overcome weaker interactions between Cr layers caused by the presence of these MDNs.

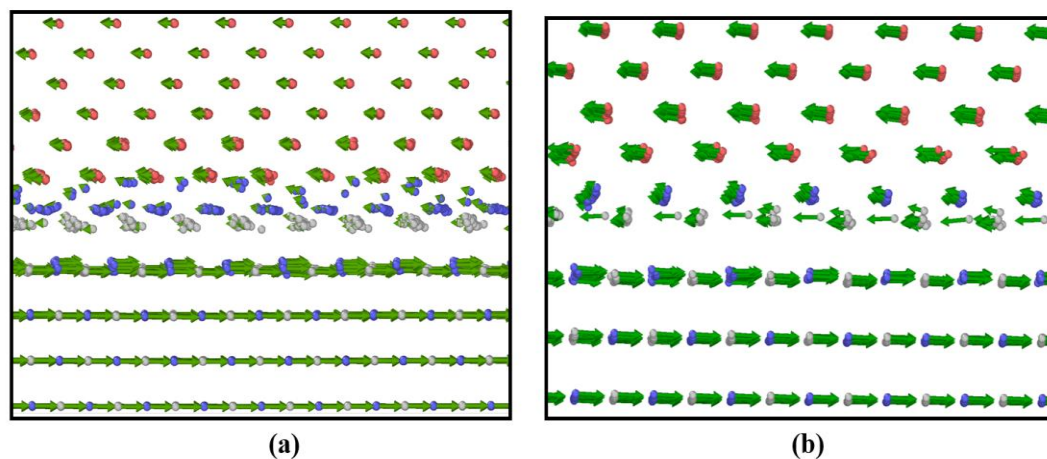


**Figure 3-10:** Snapshots of the displacement of atoms immediately after shear failure (a) for coherent system and (b) for with MDNs at the M=1 layer. Red atoms represent Cr, blue atoms N, and white atoms Ti.

**Figure 3-11a** shows the shear stress vs the stress step relative to shear failure for the Cr/TiN system with MDNs present at the M=1 and M=5 layers. The snapshots in **Figure 3-11(b-d)** correspond to the letters in **Figure 3-11a** all showing the M=1 layer and all ceramic atoms. Atoms in the snapshots are color coded with respect to their CSP. For the system with MDNs at M=1 along both X and Y axes, the elastic deformation was observed up to point **b** in the plot. Further shear loading resulted in a plastic deformation region for the metal/ceramic system leading to point **c**, as can be observed from the flattening of the stress curve in **Figure 3-11a**. In the corresponding snapshots, it can be observed that the nodes present in the minimum energy structure (see **Figure 3-5a**) start to expand and move at point **b** as shown in **Figure 3-11b**. During the plastic deformation, the size of the locally disordered region expands until it propagates through the entire system when it reaches point **c** as shown in **Figure 3-11c**. When the MDN is only present in one direction, no specific nodes are present like they are when MDNs are present in the

X and Y directions, and the yielding flows from the dislocation lines evenly as can be observed in **Figure 3-11d**.

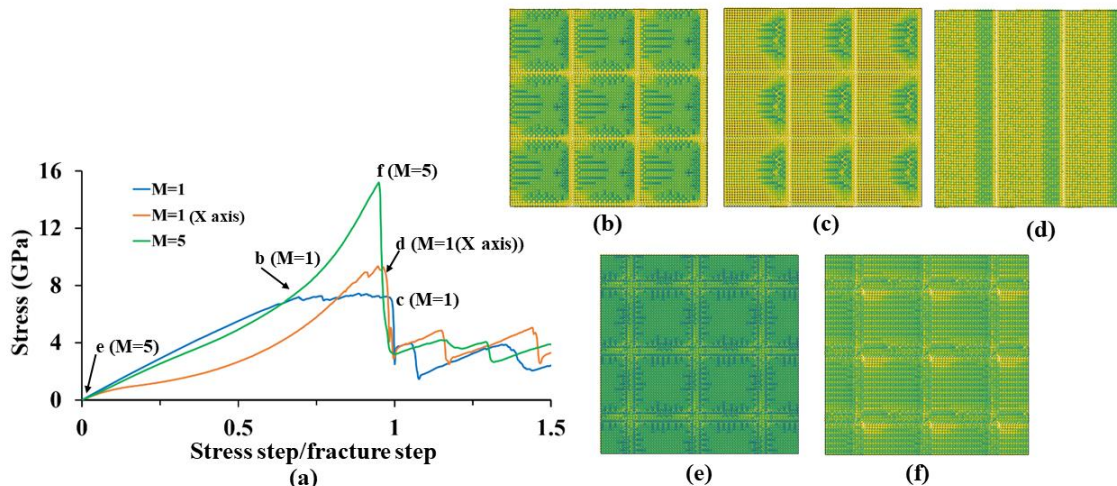


**Figure 3-11:** (a) Stress vs stress step scaled by the fracture step. (b-f) Snapshots of different configurations in the shear calculations as shown in the stress plot with letters on the stress plot corresponding to the snapshot letters in parenthesis.

The consequence is a sharper peak in stress before shear failure, as can be observed near point **d**. As described previously, when the MDNs are present at  $M=5$ , the yielding does not occur at that layer to a significant amount, but near the chemical interface. **Figure 3-11e** shows the equilibrium structure for the system with MDNs at  $M=5$ , but unlike **Figure 3-5c**, the top layer shown is the  $M=1$  layer, which is closer to where shear failure occurs. It is apparent that the disorder induced by the MDN propagates to the interfacial region to a modest degree. Shown at point **f** in **Figure 3-11a**, a very sharp peak is present at shear failure with no plastic behavior. **Figure 3-11f**, which corresponds with this point, shows only a small amount of disorder, which encompasses atoms close to the positions of the MDN in the  $M=5$  layer (four layers above what is shown). In general, MDNs in the  $M=5$  layer appears to have only a modest impact on the structure at the interface, which lowers

its shear strength in comparison with the coherent interface by around 4 GPa as shown in **Figure 3-8**.

## **CHAPTER 4**

### **DOPED METAL/CERAMIC SYSTEMS**

#### **4.1 Introduction**

An important consideration while studying metal/ceramic interfaces is the presence and impact of impurities or dopant atoms on the interfacial properties of the metal/ceramic interfaces. Dopants have been known to affect the bonding and cohesion at imperfections such as grain boundaries of the metal/ceramic interfaces [153–155]. They further impact the adhesion at the metal/ceramic interface [156–160]. A number of first principles calculations were done to study the interfacial properties of metal/ceramic systems with the introduction of transition metal dopants into them [120,161].

In a recent first principles study, it was observed that the addition of Al to the Ti/TiN interfacial region significantly increased the generalized stacking fault energy (GSFE) barrier by drawing some of the electron charge from the ceramic N atoms into the Ti phase [131]. However, DFT is limited to the study of small sized systems due to the high computational cost associated with them [162]. In order to study the effect of much complicated interfacial effects, such as how MDNs affect interfacial mechanical properties of materials with defects, larger system sizes are required. These will allow greater insight into experimental observations to be achieved. In particular, large-scale MD simulations can be utilized [108] to bring system sizes on the order of hundreds of thousands of atoms.

One of the main challenges in carrying out large-scale MD simulations is the need for appropriate interatomic potentials that can accurately describe the system of interest. The MEAM has been extensively utilized for metallic systems [91–94], along with different ceramics, such as TiN and CrN [103–105]. A number of metal/ceramic interfaces utilizing MEAM potentials have been recently studied providing a detailed understanding on their interfacial stability, the influence of MDNs, and shear strength [111,121]. Based on the above considerations and extending previous work in this group [131], this work describes the development of a new MEAM potential for Ti-Al-N ternary systems. The new model was used to investigate how the addition of Al dopants impacts the structure and shear strength of the Ti/TiN interface.

A detailed description of MEAM formalism has been covered in the literature [84] and also in Chapter 2. A modified form of the equation was utilized for carrying out this work where a different Rose equation compared to equation (2.7) was utilized. The energy per atom for a given reference structure is calculated from the universal equation of state by Rose *et al.* [115]

$$F[\overline{\rho^0}(R)] + \frac{1}{2} \sum \phi(R) = E^u(R) = -E_c(1 + a^* + a_3 a^{*3})e^{-a^*} \quad (4.1)$$

where

$$a^* = \alpha \left( \frac{R}{r_e} - 1 \right) \quad (4.2)$$

$$a_3 = d_{repuls}, a^* < 0 \text{ and } a_3 = d_{attrac}, a^* \geq 0 \quad (4.3)$$

and  $\alpha$  is an adjustable parameter involving contributions from the bulk modulus, cohesive energy, and equilibrium atomic volume.  $S_{ij}$ , as given in equation (2.1), is a many-body screening function that denotes the effect of the position of an atom,  $k$ , on the interaction between atoms  $i$  and  $j$ , which is limited by  $C_{min}$  and  $C_{max}$  as described in detail in the

previous work [112] and in Chapter 2. A value of  $S_{ij} = 1$  implies that the interaction between atoms  $i$  and  $j$  is unscreened while a value of  $S_{ij} = 0$  means that the interaction is completely screened. The cutoff distance of 5 Å was used in this work.

For pure elements, 13 MEAM parameters are required to be determined:  $\beta^{(0)}$ ,  $\beta^{(1)}$ ,  $\beta^{(2)}$ ,  $\beta^{(3)}$ ,  $t^{(1)}$ ,  $t^{(2)}$ ,  $t^{(3)}$ ,  $A$ ,  $\alpha$ ,  $E_c$ ,  $r_e$ ,  $C_{min}$ , and  $C_{max}$ . Normally, the equilibrium structure is taken as the reference structure and  $E_c$  and  $r_e$  values are set to experiment. The reference structures for Ti and Al are hcp and fcc, respectively and the MEAM parameters for N were taken from the literature without any modification [105]. For each binary system, parameters such as  $E_c$  between them in equation (4.1),  $\alpha$  and  $r_e$  values in equation (4.2), four  $C_{min}$  and four  $C_{max}$  values, giving a total of 11 additional parameters are required to be fitted.

For ternary interactions, an additional six parameters, three  $C_{min}$  and three  $C_{max}$ , are to be fitted. For the pure Ti and the binary TiN system, the previously developed model designed to study the Ti/TiN interface was used [121]. We parameterized a model for pure Al and compared it with the one developed by Lee et al. [96], along with a model for the binary combinations Al-N and Ti-Al (Ti-N we took from previous work [121]), and for the ternary combination of Ti-Al-N. The optimization of a set of MEAM parameters was done by utilizing a Python code developed by our group based on minimizing the mean square displacement between the calculated and experimental/DFT derived properties with the aid of a genetic algorithm [119].

## 4.2 DFT calculations

The same DFT methods as used in Chapter 3 were used. The monovacancy formation energy, surface energies, and the GSFEs for the pure Al atom were calculated using first-principles DFT. In order to calculate the monovacancy formation energy, the Brillouin zone was sampled using  $4 \times 4 \times 4$  mesh of k-points for the 32-atom cells. The surface energies were calculated for the surfaces Al(001), Al(110), and Al(111) with the system sizes of 36, 32, and 24 atoms respectively and the Brillouin zone was sampled using  $4 \times 4 \times 1$  k-point mesh. For each of these surfaces, a periodic system with a 15 Å of vacuum was created, resulting in the formation of two surfaces.

The GSFE surface was calculated for the Al(001) and Al(111) planes. For both, a system of 48 atoms was used with 12 layers of 4 atoms each with 15 Å of vacuum present. In the Al(001) GSFE calculation, half of the atoms were displaced in the X[110] and Y[ $\bar{1}10$ ] directions, while for Al(111), the displacements were in the X[001] and Y[00 $\bar{1}$ ] directions, keeping the other half of atoms fixed as had been done previously [38]. A total of ten positions along X and ten along the Y directions were sampled, mapping a total of 100 points. For each point, an energy minimization followed their displacement, allowing the atoms to only relax in the Z direction (keeping X and Y positions all fixed). The minimum energy path was then plotted along the X direction after mapping the full GSFEs [131]. The maximum height of the minimum energy plot gives the energy barrier of the shear displacement of the GSFE surfaces.

The binary systems had their elastic constants, surface energies, and the enthalpies of mixing calculated using DFT. The elastic constants were calculated using a system size of 64 atoms for TiAl, 24 atoms for TiAl<sub>3</sub> and 24 atoms for Ti<sub>3</sub>Al with a  $12 \times 12 \times 12$  k-

point mesh. To calculate the enthalpy of mixing, a  $\text{Ti}_3\text{Al}$  system of 24 atoms, a  $\text{TiAl}_3$  system of 32 atoms and a  $\text{TiAl}$  system of 32 atoms were used, each with a  $4 \times 4 \times 4$  k-point mesh. For the surface energy calculations, 48, 44 and 72 atoms were used for  $\text{TiAl}(001)$ ,  $\text{TiAl}(110)$  and  $\text{TiAl}(111)$ . In each of these systems,  $15 \text{ \AA}$  of vacuum were present normal to the surface in consideration, and a k-point grid of  $4 \times 4 \times 1$  was used for all the cases. The impact of spin-polarized calculations was investigated for all the systems, and it was found that they did not have a significant impact on the structure and energetics of these systems.

The GSFE calculations of the interfacial systems were carried out in previous work [131]. The metal phase included 16 layers of 4 atoms (64 total metal atoms) with its (0001) surface in contact with the (111) surface of 6 layers of TiN (48 total atoms) with the N atoms oriented towards the Ti phase. As with the metal GSFE calculations,  $15 \text{ \AA}$  of vacuum was present. The value of M describes the metal layer away from the TiN surface. Three different system configurations were used for the GSFE calculations: a system with one Al atom in the M=1 layer, a system with two atoms in the M=2 layer, and a system with 16 Al atoms (1/4 of the metal atoms), which were distributed based on a Monte Carlo minimization scheme. The determination of the GSFE was carried out by displacing the atoms along the X and Y planes in 10 increments each (see ref. [131] for the specific directions and further details). The plane in which the displacement occurred was in between the M=1 and M=2 surface layers in the metal phase, which has the lowest barrier for the Ti/TiN interface.

### 4.3 Calculation of properties from the MEAM model

The LAMMPS simulation software [133] was used to calculate all the MEAM parameters. For Al, the lattice parameters, ratios of the energy of different crystal structures ( $E_{bcc}/E_{fcc}$ ) and ( $E_{hcp}/E_{fcc}$ ), surface energies ( $E_s$ ) of various surfaces Al(001), Al(110), Al(111), solid density ( $\rho_s$ ), elastic constants, and monovacancy formation energy ( $E_{vac}$ ) were calculated. For all calculations except the solid density, energy minimizations were carried out with the conjugate gradient method. The fcc system had 108 atoms, the hcp system had 48 atoms, and the bcc system had 54 atoms. To calculate the monovacancy formation energy for Al, one atom was removed from the fcc system of 108 atoms. The elastic constant calculations were carried out for the fcc system with 108 atoms, and systems with 72, 48, and 48 atoms were used for the calculation of surface energies of Al(001), Al(110), and Al(111) surfaces, respectively. To calculate the solid density for Al metal, 20 ps of NPT simulations of a system with 500 atoms were carried out at 298 K and 1 atm using the Nosè-Hoover thermostat and barostat [134,135] with a timestep of 1 fs.

The enthalpy of mixing was calculated for TiAl, TiAl<sub>3</sub> and Ti<sub>3</sub>Al. The enthalpy of mixing was calculated using a system of 128 atoms for TiAl, 64 atoms for Ti<sub>3</sub>Al and a system of 64 atoms for TiAl<sub>3</sub>. The surface energies were calculated using a system size of 72 atoms for both TiAl(001) and TiAl(100), 64 atoms for TiAl(110) and 54 atoms for TiAl(111) surfaces. The elastic constants were calculated using 36 for TiAl, and 64 for both Ti<sub>3</sub>Al and TiAl<sub>3</sub>. For ternary systems, the enthalpy of mixing and lattice parameters were calculated using 216 atoms for Ti<sub>2</sub>AlN and 40 for Ti<sub>3</sub>AlN. The surface energy for the Ti<sub>2</sub>AlN(0001) hexagonal system was calculated using 32 atoms, and 40 atoms for Ti<sub>2</sub>AlN(001), 80 atoms for Ti<sub>2</sub>AlN(110) and 112 for Ti<sub>2</sub>AlN(111) system. The elastic

constants for the  $\text{Ti}_2\text{AlN}$  and  $\text{Ti}_3\text{AlN}$  systems were calculated using 96 atoms and 40 atoms, respectively. The GSFs were calculated using the same system sizes as used in DFT calculations described in Section 4.3.

#### 4.4 Large scale MD simulations

In this work, the orientation with the lowest energy found in previous work for Ti/TiN was used [121]:  $X \parallel [11\bar{2}0]_{\text{Ti}} \parallel [1\bar{1}0]_{\text{TiN}}$ ;  $Y \parallel [\bar{1}100]_{\text{Ti}} \parallel [11\bar{2}]_{\text{TiN}}$  and  $Z \parallel [0001]_{\text{Ti}} \parallel [111]_{\text{TiN}}$ . The length of the X and Y dimensions were 16.1 nm and 27.9 nm respectively for the Ti/TiN system in order to minimize the lattice mismatch between the metal and the ceramic at the interface. Previous work also found that the interfacial energy was lowest when a MDN was present on the Ti layer adjacent to the TiN interface, so that was the configuration used in this study (see reference [162] for a detailed description of the formation of dislocations). A total of 133100 atoms in the metal phase and 69984 Ti and N atoms combined in the ceramic phase were used in the simulation.

A number of the Ti atoms in the metal phase were replaced with Al atoms giving mol % ranging from 1 to 25%. It should be noted that 25% Al means that 25% of the 133100 Ti atoms in the metal phase are replaced (33275). To find the most likely configuration for these atoms, a Monte Carlo (MC) scheme was developed as follows.

- 1) The Al atoms were placed randomly in the Ti metal phase excluding the top two layers. An energy minimization followed.
- 2) Each MC move attempted to exchange 5 atoms (*nexchange*) using Rosenbluth sampling to reduce the number of energy calculations required. The Ti and Al atoms that were chosen for exchange included all atoms not present in the top two or bottom two layers of the system.

3) For each atom exchange attempt, a total of 10 (*ntrial*) trials were attempted. The acceptance probability for each trial was carried out with the following probability.

$$P_{acc}^{trial} = \frac{P_i}{\sum_j P_j} \quad (4.4)$$

where the sum of  $j$  is over *ntrial*. How each  $p_i$  was determined will be described below.

4) After the *nexchange* exchange attempts were carried out, a single energy minimization was carried out, and if the energy was lower than the energy before the exchanges were attempted, then the entire MC move was accepted.

If the goal were to sample the system at a specific state (i.e., with a set temperature and pressure), the biasing used for the trials would need to be accounted for in the final acceptance. Since the goal is to find the minimum energy of the system (the most stable configuration), this is not necessary. The  $p_i$  values used to bias the trialed atomic exchanges was generated by the identity of the 12 nearest neighbors around each atom type. For instance, in bulk Ti doped with Al, there will be an average number of Al atoms surrounding each Al atom, along with an average number of Ti surrounding the Al atom. The biasing probabilities were constantly updated throughout the simulation based on which attempted moves were accepted to better guide which exchanges were more likely to lower the system's energy. In essence, when a MC move was accepted, the environment surrounding the exchanged Ti and Al atoms in the accepted configurations are used to update  $p_i$ . **Figure 4-1** gives a representative configuration with 4 mol% of Al in Ti. As can be observed, the Al atoms are distributed throughout the system, including the TiN phase as well, albeit in a much lower concentration than in the Ti phase.

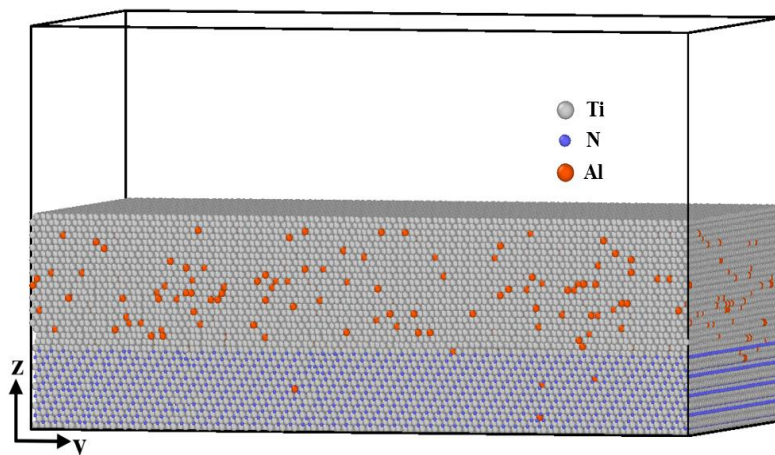


**Figure 4-1:** Al doped Ti/TiN metal/ceramic system snapshot with 4 mol%.

## 4.6. Results and discussion

### 4.6.1. Pure Al metal

The parameters for the Al MEAM model developed for this work are shown in **Table 4-1**. A comparison of the DFT calculated/experimental properties with values obtained using an existing model (Lee model) [96] and the model developed for this work are given in **Table 4-2**. The values for  $E_c$  and  $r_e$  for Al were taken from the experimental values in the literature [163,164]. From **Table 4-2**, it can be observed that reasonable agreement with experimental/DFT values was achieved with both MEAM models. The fcc structure was found to be the most stable, and the correct order of the low index surface energies was achieved for both models. **Figure B-1** and **Figure B-2** in the Appendix B show detailed GSFES of Al(001) and Al(110) surfaces calculated by DFT, the new MEAM model, and the Lee model [96]. The 1D-GSFES plotted as a function of position along the x-axis is shown in **Figure 4-2**.

**Table 4-1:** MEAM potential parameters for Ti-Al-N

	$E_c$ (eV)	$r_e$ (Å)	$A$	$\alpha$	$\beta^{(0)}$	$\beta^{(1)}$	$\beta^{(2)}$	$\beta^{(3)}$	$t^{(1)}$	$t^{(2)}$	$t^{(3)}$	$C_{min}$	$C_{max}$
<b>Al</b>	3.36	1.43	0.89	4.47	2.15	4.62	7.01	0.0	1.82	-1.02	9.07	0.39	2.24
<b>Ti<sup>a</sup></b>	4.87	2.92	1.19	4.41	1.58	0.08	2.89	0.0016	5.55	6.79	-2.05	0.89	2.85
<b>N<sup>b</sup></b>	4.88	1.10	1.80	5.96	2.75	4.00	4.00	4.00	0.05	1.00	0.00	2.00	2.80

<sup>a</sup>Reference [165]<sup>b</sup>Reference [105]

The new model overpredicts the DFT barrier height in the 1D-GSFE for both surfaces, but only by a modest amount. It should be noted that better agreement with the GSFEs could not be achieved without doing significantly worse on reproducing other properties such as lattice constants, cohesive energy, and elastic constants.

**Table 4-2:** Comparison of the DFT calculated/experimental properties of Al with values obtained using the Lee model [96] and the newly developed model in this work.

Property	DFT/expt value	New model	Lee model <sup>d</sup>
Lattice parameters (Å)	12.1487	12.150	12.133
	12.1487	12.150	12.133
	12.1487	12.150	12.133
$E_{vac}$ (eV)	0.78 <sup>a</sup> , 0.68 <sup>b</sup>	1.046	0.6788
$E_s$ (111) (J/m <sup>2</sup> )	1.14 <sup>a</sup>	0.874	0.6263
$E_s$ (100) (J/m <sup>2</sup> )	1.366 <sup>a</sup>	1.069	0.8545
$E_s$ (110) (J/m <sup>2</sup> )	1.433 <sup>a</sup>	1.254	0.9152
Elastic constants (GPa)			
$C_{11}$	114 <sup>a</sup>	95	114
$C_{12}$	62 <sup>a</sup>	60	61
$C_{44}$	32 <sup>a</sup>	32	31
$\rho_s$ (g/cm <sup>3</sup> )	2.70 <sup>c</sup>	2.697	2.7182
$E_{bcc}/E_{fcc}$	0.971 <sup>a</sup>	0.9882	0.9647
$E_{hcp}/E_{fcc}$	0.994 <sup>a</sup>	0.9975	0.9912

<sup>a</sup>DFT calculated in this work.<sup>b</sup>Reference [166]<sup>c</sup>Reference [143]<sup>d</sup>Reference [96]

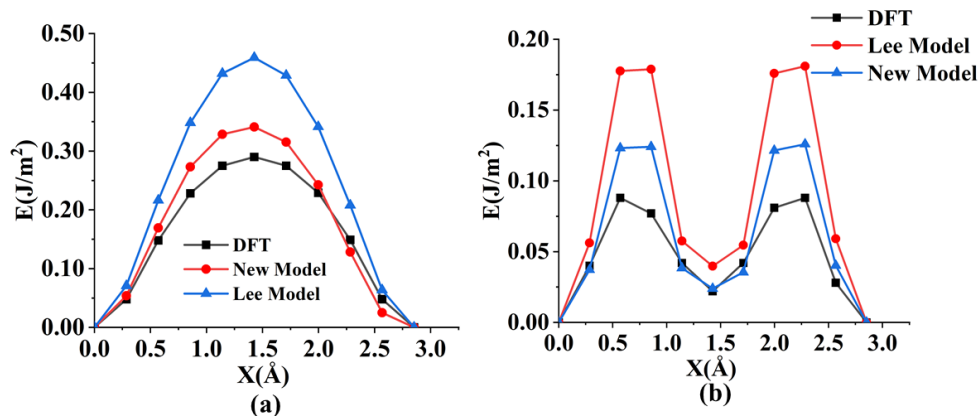


**Figure 4-2:** Comparison of the 1D-GSFs for pure Al from DFT, the new MEAM model, and the Lee model along the (a) (001) and (b) (111) planes.

#### 4.6.2. Mixed Systems

The binary parameters for TiAl, Ti<sub>3</sub>Al, and TiAl<sub>3</sub> were fit to several properties, including enthalpies of mixing, elastic constants, and surface energies. **Table 4-3** and **Table 4-4** show the values of the binary and ternary parameters obtained in the present work, respectively, while the Ti-N binary parameters have been taken from our previous work [121]. The DFT and the MEAM calculated values of various properties of binary and ternary Ti-Al-N systems using the present model are presented in **Table 4-5** and **Table 4-6**. Reasonable agreement between the model and DFT/experimental results are obtained for the properties of TiAl and Ti-Al-N systems. It should be noted that in addition to these properties, a major focus of the parameterization was to reproduce GSFs for Al doped Ti and Ti/TiN.

**Table 4-3:** MEAM potential parameters for the binary systems ( $x$ - $y$ ). In any pair, the first element is denoted by  $x$ , and the second element is denoted by  $y$ .

Parameters	(x-y) pair		
	Ti-Al	N-Al	Ti-N <sup>a</sup>
Reference state	b2	b1	b1
$E_c(x, y)$ (eV)	4.8436	6.53	6.6139
$r_e(x, y)$ (Å)	3.023	1.6258	2.1195
$\alpha(x, y)$	4.022	6.8183	4.7225
$C_{min}(x, x, y)$	2.0	0.7183	0.4263
$C_{min}(y, y, x)$	1.4088	0.3414	1.0733
$C_{min}(x, y, x)$	0.055	0.8582	1.5
$C_{min}(x, y, y)$	0.9356	1.1618	1.5
$C_{max}(x, x, y)$	4.0	3.3405	2.0328
$C_{max}(y, y, x)$	2.1333	2.5308	1.7998
$C_{max}(x, y, x)$	2.6437	3.2418	2.4073
$C_{max}(x, y, y)$	2.9925	3.9408	2.3557

<sup>a</sup>Reference [121]

**Table 4-4:** MEAM potential parameters for the Ti-Al-N ternary system

Parameters	Value
$C_{min}(\text{Ti, Al, N})$	0.0848
$C_{min}(\text{Ti, N, Al})$	1.2438
$C_{min}(\text{Al, N, Ti})$	1.5301
$C_{max}(\text{Ti, Al, N})$	2.517
$C_{max}(\text{Ti, N, Al})$	2.4209
$C_{max}(\text{Al, N, Ti})$	3.1322

**Table 4-5:** Values of the properties of the TiAl binary model compared with the experimental/DFT results.

Property	System		Expt/DFT	New Model	Lee Model <sup>f</sup>	
$\Delta H_{\text{mix}}$ (eV/atom)	TiAl		-0.258 <sup>a</sup>	-0.237	-0.141	
	Ti <sub>3</sub> Al		-0.279 <sup>a</sup>	-0.313	-0.029	
	TiAl <sub>3</sub>		-0.398 <sup>a</sup>	-0.435	-0.163	
Elastic Constants (GPa)	TiAl	$C_{11}$	187 <sup>b</sup>	192	190	
		$C_{12}$	74.8	83	67	
		$C_{13}$	74.8	111	133	
		$C_{33}$	182	224	234	
		$C_{44}$	109	172	86	
		$C_{66}$	81.2	52	52	
	Ti <sub>3</sub> Al	$C_{11}$	183.2 <sup>c</sup>	241	200	
		$C_{12}$	89.0	95	107	
		$C_{13}$	62.6	56	91	
		$C_{33}$	225.1	286	238	
		$C_{44}$	64.1	67	45	
		$C_{66}$	47.1	73	46	
	TiAl <sub>3</sub>	$C_{11}$	217.7 <sup>d</sup>	202	152	
		$C_{12}$	57.7	105	138	
		$C_{13}$	45.5	90	116	
		$C_{33}$	217.5	188	154	
		$C_{44}$	92	100	71	
		$C_{66}$	116.5	143	87	
	$E_S$ (J/m <sup>2</sup> )	TiAl	(001)	2.16 <sup>e</sup>	1.92	2.43
			(110)	1.64 <sup>e</sup>	0.64	1.80
			(111)	1.79 <sup>e</sup>	1.00	1.98
(100)			2.03 <sup>e</sup>	1.75	2.09	

<sup>a</sup>Reference [167]

<sup>b</sup>Reference [168]

<sup>c</sup>Reference [169]

<sup>d</sup>Reference [170]

<sup>e</sup>DFT calculated in this work

<sup>f</sup>Reference [96]

**Table 4-6:** Values of the properties of the TiAlN ternary model compared with the experimental/DFT results

Property	System		Expt/DFT	New Model
Lattice parameters	Ti <sub>2</sub> AlN (hexagonal)		8.98	8.90
			7.77	7.71
			40.83	41.34
	Ti <sub>3</sub> AlN (cubic)		8.22	8.20
			8.22	8.20
			8.22	8.20
$\Delta H_{\text{mix}}$ (eV)	Ti <sub>2</sub> AlN(hexagonal)		-1.32	-1.21
	Ti <sub>3</sub> AlN (cubic)		-1.00	-1.14
Elastic constants (GPa)	Ti <sub>2</sub> AlN(hexagonal)	$C_{11}$	305	234
		$C_{12}$	67	96
		$C_{13}$	93	105
		$C_{33}$	281	322
		$C_{44}$	123	109
		$C_{66}$	119	69
	Ti <sub>3</sub> AlN (cubic)	$C_{11}$	202	335
		$C_{12}$	144	55
		$C_{13}$	-	-
		$C_{33}$	-	-
		$C_{44}$	60	177
		$C_{66}$	-	-
$E_S$ (J/m <sup>2</sup> )	Ti <sub>3</sub> AlN (cubic)	(001)	1.69*	1.76
		(110)	2.32	2.12
		(111)	1.83	1.95
	Ti <sub>2</sub> AlN (hexagonal)	(0001)	2.208*	1.87

Previous work showed that with two Al atoms in adjacent layers of bulk Ti the lattice had the lowest enthalpy of mixing [131]. Furthermore, GSFES from this work showed a significant increase in barrier height for this configuration, so it was a focus on

parameterization for the new model. **Figure 4-3** gives a snapshot of the system in which the GSFE was extracted, along with the associated 1D-GSFE (See **Figure B-3** in the Appendix B for the full GSFE). The plane in which the GSFE was calculated is between the two Al atoms in the X and Z directions in **Figure 4-3a**. The 1D-GSFE has a complex structure than the ones extracted from pure phases, but the new model does a reasonable job of reproducing it.

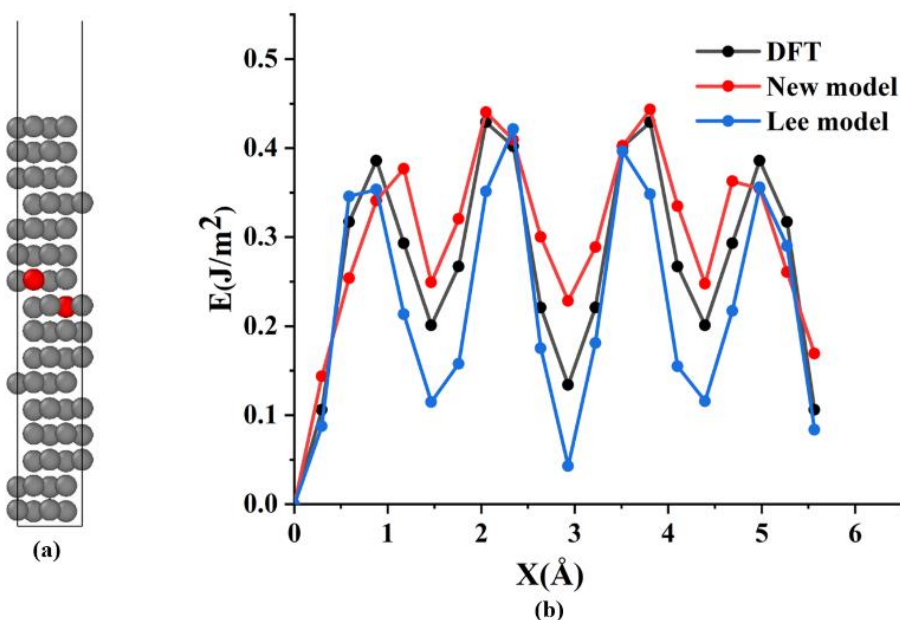


**Figure 4-3:** (a) Snapshot of the Al (red atoms) and Ti (gray atoms) used to calculate the GSFE. (b) Comparison of DFT, the new model and the Lee model [96] 1D-GSFE for this system.

For a low concentration doping of, the substitutional dopant atoms were added at different layers of the Ti/TiN interfaces. **Figure 4-4** shows comparisons of the 1D-GSFEs between the M=1 and M=2 metal layers for the Al doped Ti/TiN interfacial systems from DFT and the new model. The three systems are those with a single Al atom (**Figure 4-4a**), two Al atoms (**Figure 4-4b**), and 16 Al atoms, or 25% of the metal atoms (**Figure 4-4c**).

The full GSFES for these systems, along with snapshots of their structures, are given in **Figure B-4**, **Figure B-5**, and **Figure B-6** in the Appendix B. The agreement between the DFT and MEAM is not particularly good for the system with one Al atom but is significantly better for two systems with two or more Al atoms in them. This was due to our greater emphasis being placed on systems with more Al atoms than the one with only one Al atom in the MEAM parameterization strategy. There is reasonable agreement between the new model and DFT for the system with two Al atoms, while the agreement for the system with 16 Al atoms is particularly good. Overall, the new model somewhat underestimates the 1D-GSFE barrier, but agreement improves with higher Al concentration, in which the barrier heights increase to a value of approximately  $0.28 \text{ J/m}^2$ .

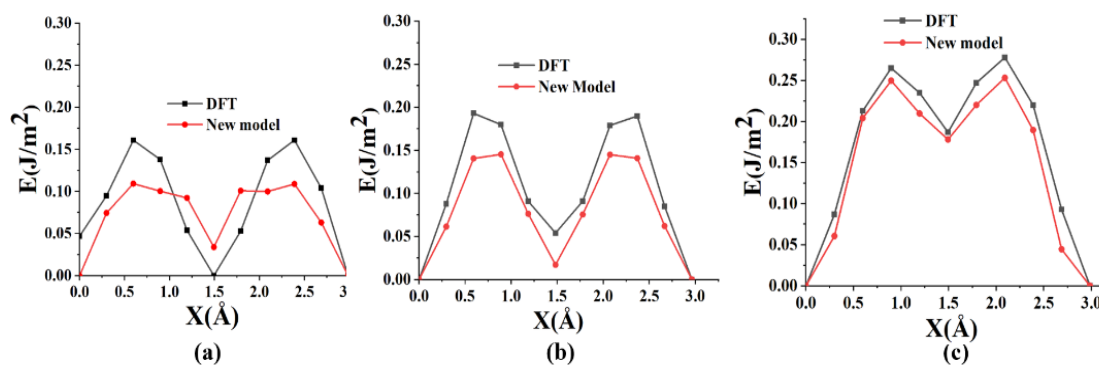


**Figure 4-4:** Comparison of the 1D-GSFE for Ti/TiN with (a) 1 Al atom in the M=1 layer (b) 2 Al atoms in the M=2 layer (c) 16 Al atoms extracted from MC calculations.

## 4.6. Large scale simulation

### 4.7.1. Structure and Stability

The purpose of the MC simulations was to find low energy configurations for high concentrations. As stated before, the most stable structure for Ti/TiN is with an MDN in the M=2 layer (or the second metal layer from the TiN phase). Because of this, all large-

scale simulations included an MDN here. **Figure 4-5a** shows the energy with respect to MC step for the different systems studied, showing a rapid initial decrease in energy followed by a slower one. The rate at which the decrease in energy occurs increases significantly at higher Al concentrations, but after 5000 steps, it appears fairly stable as a function of step in all cases. The plot is of total energy, which is generally higher with a larger Al concentration due to its lower cohesive energy. To compare the stability of the different systems, the enthalpy of mixing is a better measure, which is calculated as follows when there are  $n$  Al atoms exchanged with Ti atoms,

$$\Delta H_{\text{mix}} = E_{\text{doped}} - E_{\text{undoped}} + nE_{\text{Ti}} - nE_{\text{Al}} \quad (4.5)$$

where  $E_{\text{undoped}}$  is the Ti/TiN system, and the  $E_{\text{Al}}$  and  $E_{\text{Ti}}$  systems are the bulk Al and Ti systems, respectively. **Figure 4-5b** gives the enthalpy of mixing as a function of Al concentration after the 5000 MC steps were completed for each system. Unlike the total system energy, the enthalpy decreases with increasing Al concentration until 25 mol % is reached, after which it increases.

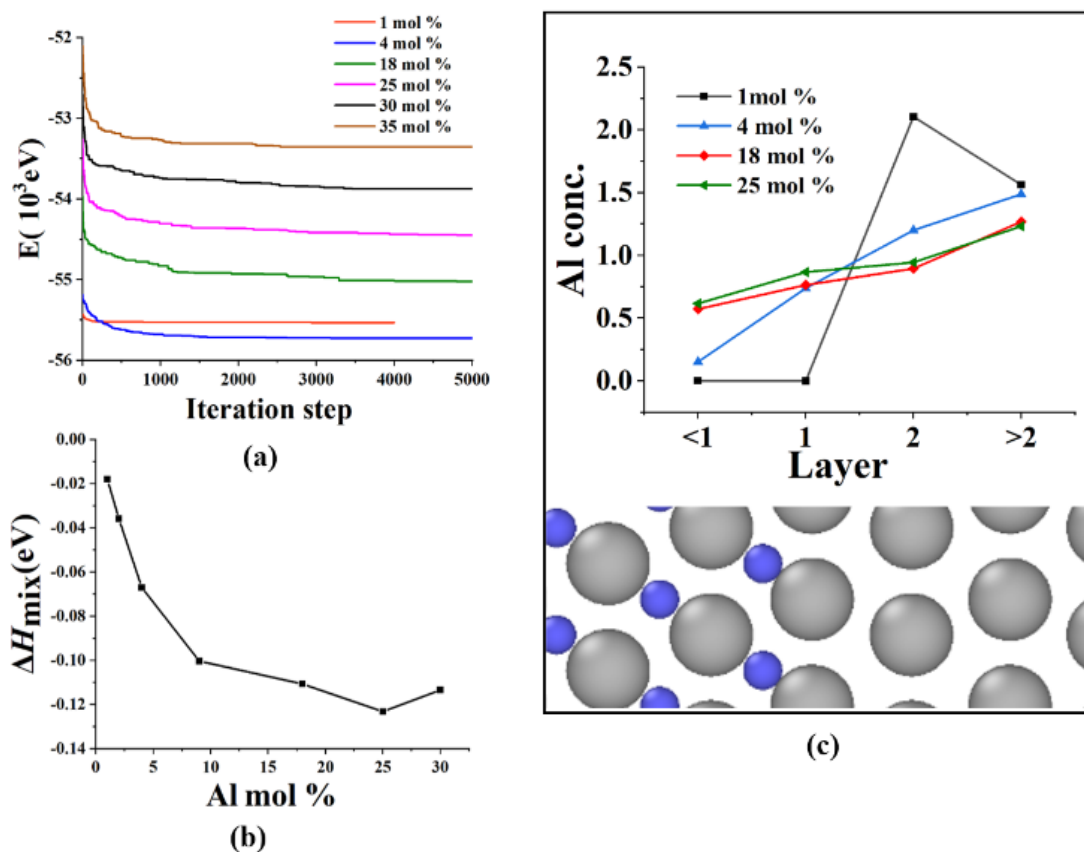


**Figure 4-5:** (a) Plot of the total energy with respect to MC step (b) Enthalpy of mixing of various Al doped Ti/TiN metal/ceramic systems (c) Aluminum concentration in each layer of Ti/TiN system with the snapshot below the figure shows the position of each layer.

To demonstrate the distribution of Al atoms at the doped Ti/TiN interface, **Figure 4-5c** gives the relative Al concentration as a function of position with respect to the interface. Layer one is the metal layer immediately next to the TiN phase coinciding with the snapshot at the bottom of the **Figure 4-5(c)**. A value of 1.0 in Al conc. represent the overall average Al concentration with respect to all of the Ti atoms in the system. So, if the Al atoms are evenly distributed, there will be a value of 1.0 throughout at any mol % of Al. From MC simulations, it was observed that For the system with 1 mol % Al, there is essentially zero Al atoms in the TiN phase or in the metal layer adjacent to the TiN surface,

while the most likely position to find one is in layer two. This is consistent with previous DFT calculations when one or two Al atoms were present [131]. At all higher Al concentrations, the probability to find Al atoms in layer two become lower than in bulk Ti, showing that the higher Al concentration in layer two is only present for the lowest concentrations. Al atoms do not significantly accumulate in layer one or in the TiN phase until 4 mol % is reached, showing that this is also a consequence of higher concentrations.

#### 4.7.2. Interfacial Shear

The shear strength was calculated by using a stress-controlled shear loading with quasi-static loading applied in the X direction, as used previously in Chapter 3 [34]. The method used incremental deformation gradients separately applied to the metal and ceramic phase, which were implemented in the  $X \parallel [11\bar{2}0]_{\text{Ti}} \parallel [1\bar{1}0]_{\text{TiN}}$  direction, followed by energy minimization at fixed deformation. **Figure 4-6a** shows the plot of shear stress in the various Al doped Ti/TiN systems as a function of iteration step of the quasi-static loading procedure. The results for the undoped system are taken from previous work [121], which has an extremely low shear strength that is reached with a handful of iteration steps. With increased doping, it takes more iteration steps to reach plastic behavior, with the maximum, or close to maximum, shear stress reached within 500 steps. To better compare how Al concentration impacts shear stress, **Figure 4-6b** shows the maximum shear stress as a function of Al concentration. The value for the undoped system is very small, almost unimpeded due to the presence of the MDN and the low GSFE barrier near the Ti/TiN interface [121]. When the Al concentration is increased slightly, the shear stress increases a substantial amount, to over 150 MPa, increasing at an almost linear rate with higher Al mol % until the strength is greater than 1 GPa at 25 Al mol %.

To determine specifically where shear failure occurs, the displacement was calculated as a function of percent strain for each layer near the metal/ceramic interface. Specifically, the displacement difference between adjacent layers was calculated, which is shown in **Figure 4-7** for the undoped interface, the system with 4 Al mol % and the system with 25%. All the systems were displaced up to the displacement value of 10 Å. It was observed that as the concentration of Al atoms increased, the displacement of dislocations does not restrict to their plane but extends across layers indicating the formation of dislocation jogs.

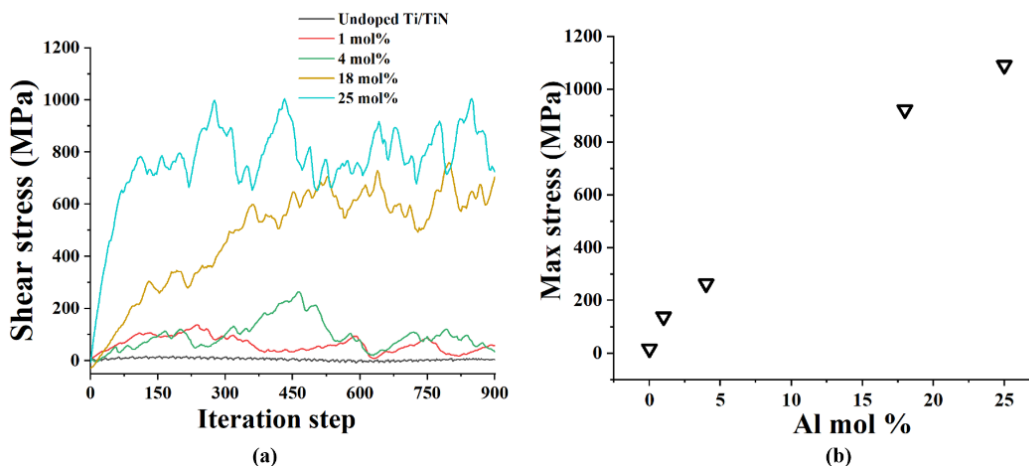


**Figure 4-6:** (a) Plots of shear stress versus iteration step, and (b) of maximum shear stress achieved for the different Al concentrations in Ti/TiN interfacial systems.

The jogs serve as strong pinning point to the motion of MDN [34] and hence they do not move easily in response to loading. The pinning effect of jogs result in increased interfacial shear strength.

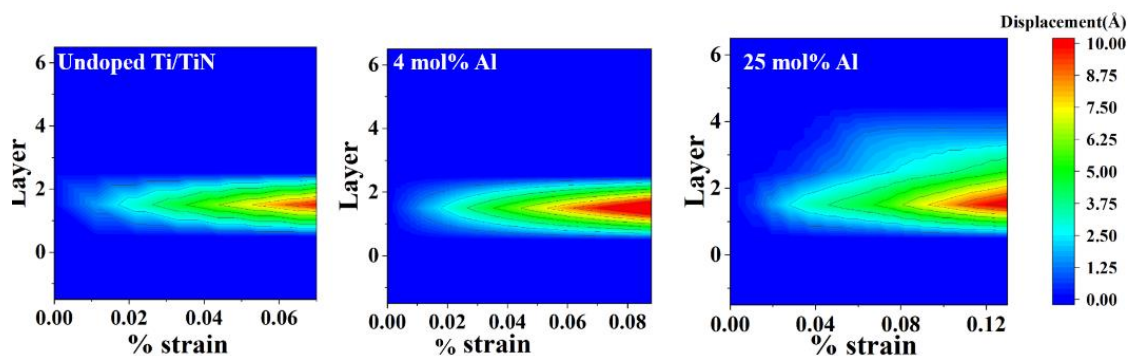


**Figure 4-7:** Snapshots of displacement for various layers of Al doped Ti/TiN surfaces

As shear failure occurs between the second and third layers, we investigated the structure of the system in the first two metal layers next to the ceramic, along with the ceramic phase. It can be observed from **Figure 4-8(top)** that the increase in the doping concentration of Al atoms resulted in the formation of more constricted nodes. More constricted nodes resulted in the higher GSFE barrier. The alloying or doping Al atoms made the plastic deformation difficult by impeding the dislocation motion through creation of local strain fields that were created due to the alloying elements interacting with the dislocations.

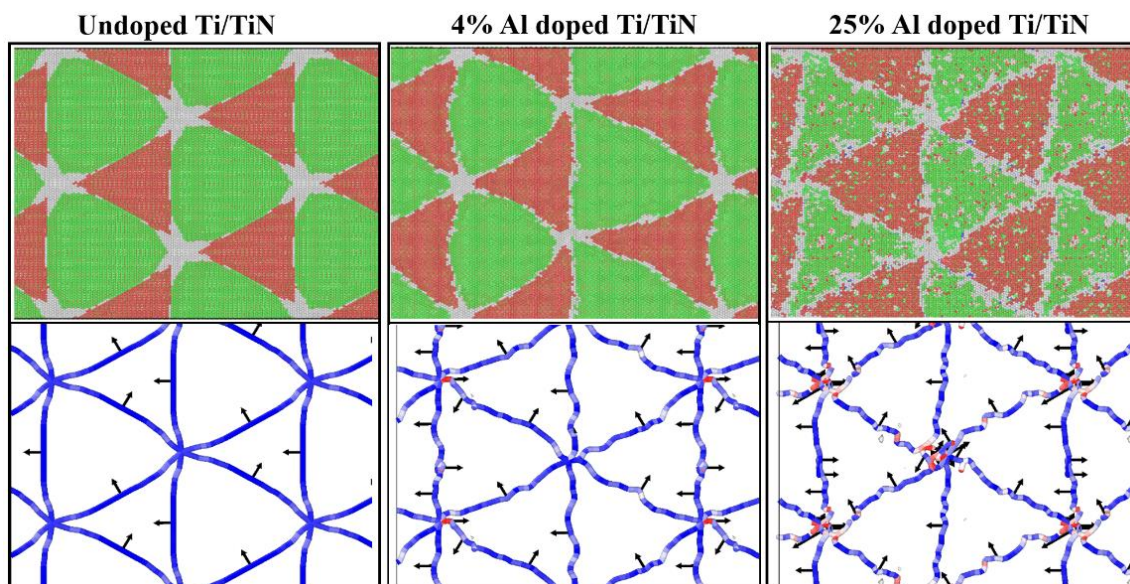


**Figure 4-8** (top) Snapshots of various Al doped Ti/TiN surfaces with green representing fcc, red hcp, and gray neither. (bottom) Dislocation and Burgers vector analysis of various Al doped Ti/TiN systems. Black arrows indicate Burgers vectors, blue lines indicate an edge type dislocation and red line indicate a screw type dislocation.

Also, the phenomenon of solid solution strengthening is realized by addition of Al into Ti/TiN metal ceramic system where the local strain fields of the alloying Al atoms in the host Ti matrix interact with the dislocations and provide resistance to the dislocation motion [171]. Such increase in the critical resolved shear stress due to the presence of Al atoms has been observed in Mg based alloys [172]. Solute Al atoms strengthened Ti over the concentration range of 0 to 15 atm % [173].

In addition, it has been observed that as the concentration of Al increased, non-planar screw dislocations were manifested as observed from **Figure 4-8** (bottom), which further impedes the motion of dislocations making the shear strength increased by an order of magnitude at 25% doping as compared to the undoped system [174,175].

## CHAPTER 5

### CONCLUSIONS AND FUTURE WORK

Although systematic studies of metal/ceramic interfaces began during early 1960s, a complete understanding of the relationship between interface chemistry and mechanical behavior is still unclear [3,176]. The subject of metal/ceramic interfaces is currently under extensive research.

We parametrized new MEAM interatomic potentials to study stability and shear strength of various metal/ceramic interfaces. The new potential expanded upon our previous work on TiN to parameterize new interactions for Cr, CrTi, CrN, and CrTiN. We fit to experimental and density function theory derived thermodynamic, mechanical, and interfacial properties. In particular, we focused on reproducing the GSFE for Cr/TiN and Ti/TiN interfacial systems, since they were found to be important for describing the formation and stability of MDNs. Using the new MEAM model, large scale MD simulations were used to determine the impact of MDN position on the stability and resistance to shear for the Cr/TiN interface.

When the MDN was located adjacent to the chemical interface, it had the largest dislocation cores and the lowest interfacial energy. The larger dislocation nodes led to the lowest shear strength, and for this particular system, a significant plastic deformation region was present. As the MDN was moved farther away from the Cr/TiN interface, the interfacial core width decreased, the interfacial energy increased, and the shear strength

increased. For all systems studied, shear failure occurred in the ceramic phase, between the first and second TiN layers from the Cr/TiN interface.

In addition to the presence of MDNs, the impact of the presence of alloying dopant atoms, such as Al, on the shear strength of Ti/TiN metal/ceramic interface was studied. A new interatomic MEAM potential for the ternary Ti-Al-N system was developed to study the impact of doping on the interfacial strength of Ti/TiN metal/ceramic interfaces. We fit to experimental and DFT derived thermodynamic, mechanical, and interfacial properties. In particular, we focused on reproducing the GSFE for various Al doped bulk Ti and Ti/TiN interfacial systems, since they were found to be important for describing the formation and stability of MDNs. The Ti metal was doped with various amounts of Al and the stability of the systems was then studied. It was observed, from our earlier DFT studies, that the most stable system was 25% Al doped Ti/TiN metal/ceramic system. The maximum shear stress increased from about 200 MPa to almost 1 GPa for the 25% Al doped Ti/TiN metal/ceramic system without much plastic deformation.

## **5.1 Future work**

In view of an array of applications of the metal/ceramic interfaces, it is likely to remain a prolific area of collaborative research. Some future work can be done to improve the interatomic potentials to accurately describe the complex chemical bonding at the interface. More reliable interatomic potentials can be developed using machine-learning based interatomic potential approach [177]. The methods developed in this work can be extended to a number of research areas based on interfaces.

### 5.1.1 Complex concentrated alloys

High Entropy Alloys (HEAs) are alloys having multiple principal alloying elements, often in near-equiatomic ratios [178]. They are alloys with multiple elements mixed in high mole fractions usually between 5% and 35% [179]. They, therefore, differ from the classical engineering alloys in the sense that they do not have one majority component with minority additions. The high configurational entropy of mixing of these HEAs results in stabilizing single phase solid-solution phases over the intermetallic phases. As a result, HEAs exhibit microstructural stability as well as a number of unique properties arising from their complex compositions [178]. However, the definition of HEAs was restricted to alloys with 5 or more principal elements that excluded the results of new alloy systems based solely on the number of elements. Hence, it was concluded that the HEA field was too broad to be described by a single definition, and the new term complex concentrated alloys (CCAs) was introduced [180]. The term is more inclusive that focus on concentrated alloys having no single dominant element. They therefore further spread out the HEA field by including concentrated ternary and quaternary alloys as well. They allow elemental concentrations in excess of 35 atomic percent and include single-phase intermetallic alloys and alloys with any number of solid solution and intermetallic phases [179].

CCAs exhibit superior mechanical properties such as high yield strength and ductility, good thermal stability, and creep resistance because of their highly disordered lattice structure. However, not much research has been carried out to design CCAs with multiple properties required for specific applications. For instance, enhanced high-cycle-fatigue (HCF) resistance and processability are two important properties in the advanced

manufacturing (AM) process, in addition to ductility and wear resistance. In order to design CCAs that meet such multi-criteria target specifications and establish a structure-property relationship in these multicomponent materials, a multivariable mapping in the hyper-dimensional compositional space is required. There are 67 stable metallic elements. The unique combination of these 67 elements taken three at a time give 47,905 ternary alloys, taken four at a time give 766,480 quaternary bases and more than 110 million new alloy bases with 3, 4, 5, or 6 principal elements [181]. This compositional space is vast consisting of almost  $10^7$  possibilities. One solution to this complex problem is Machine-Learning (ML)-guided materials design which is commercially available and can accelerate the search for AM-processable CCAs. It helps in an efficient search for candidate alloys in a compositional space extending from single principal element alloys to multi-component CCAs. The most significant stage of the ML-guided material design is generating data that can be used for initial training of ML models. DFT based calculations can be performed to predict the CCAs suitable for AM processes. However, the DFT calculations, although reliable, are computationally expensive and limited to small systems and a small number of configurations.

Large scale atomistic simulation techniques based on semi-empirical interatomic potential can be employed depending upon the availability of reliable interatomic potentials [182]. In this respect, 2NN-MEAM potential can be employed since all the constituent alloying elements can be described using one common formalism. MEAM models are far less expensive than DFT, however, parameterizing them for multicomponent alloy systems can be tedious. A number of interatomic potentials for the binary alloy systems have been developed using 2NN-MEAM that can be utilized for atomistic simulation of

multicomponent alloy systems [97,98,183–185]. Recently, the material phenomena such as sluggish diffusion and micro-twinning at cryogenic temperatures were studied for equiatomic CoCrFeMnNi HEA along with the impact of individual elements on solid solution hardening using 2NN-MEAM model [182].

Based on the above considerations, some future work can focus on development of a 2NN-MEAM model for CCAs based on 3d transition metal elements (Ni, Co, Cu, and Cr). Such newly developed MEAM models may accelerate the data generation for initial training of ML models.

## APPENDIX A

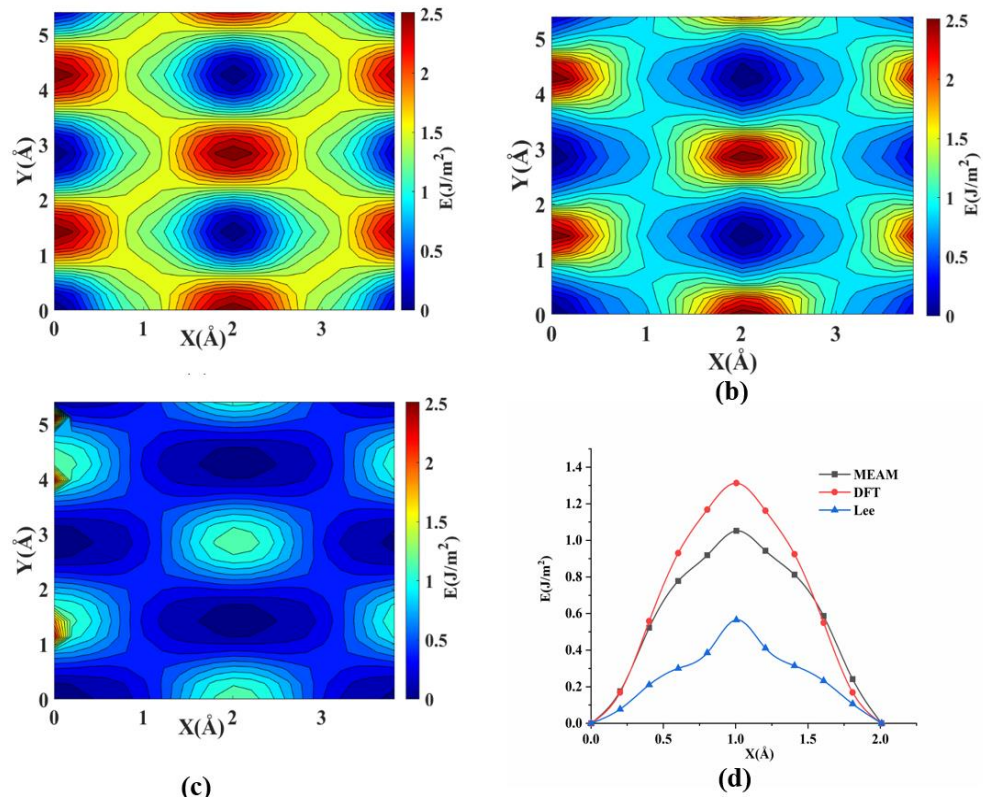


**Figure A- 1:** GSFE curves of the Cr along (110) plane calculated using (a) DFT, (b) MEAM model (c) Lee model (d) Comparison of minimum energy path (1-D GSFE) for pure Cr along (110) plane

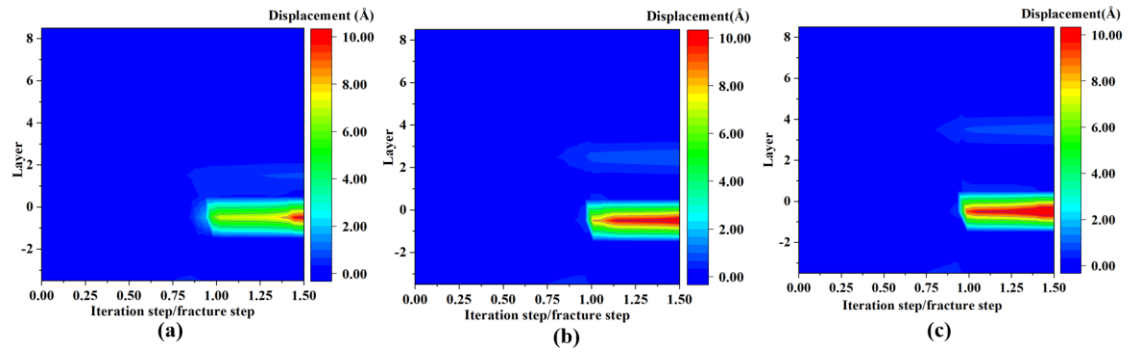


**Figure A- 2:** Plot of the displacement per layer per iteration step for (a) M=2, (b) M=3 and (c) M=4 layers.

## APPENDIX B

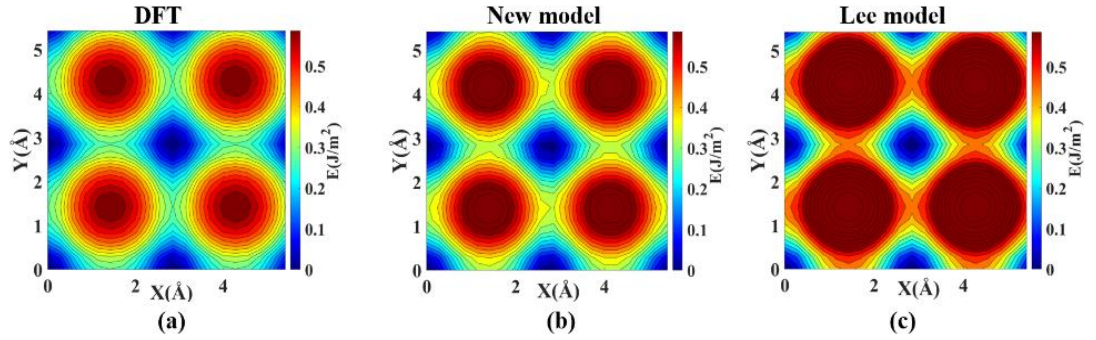


**Figure B- 1:** GSFE curves of the Al(001) calculated using (a) DFT, (b) MEAM model (c) Lee model

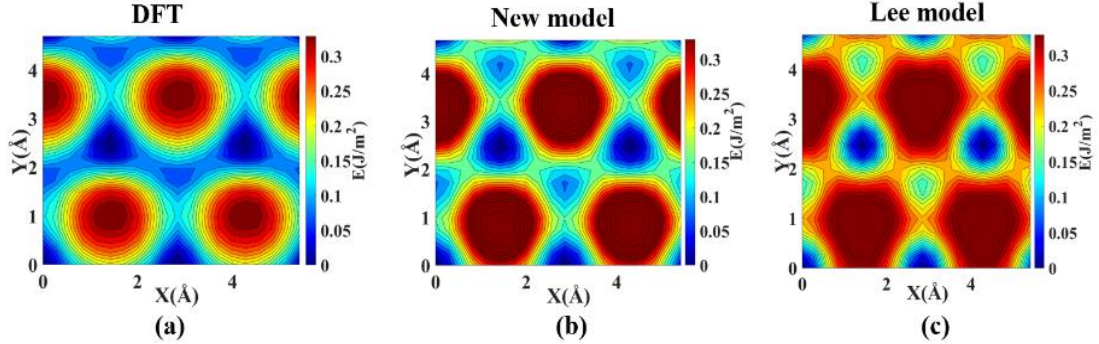


**Figure B- 2:** GSFE curves of the Al(111) calculated using (a) DFT, (b) MEAM model (c) Lee model

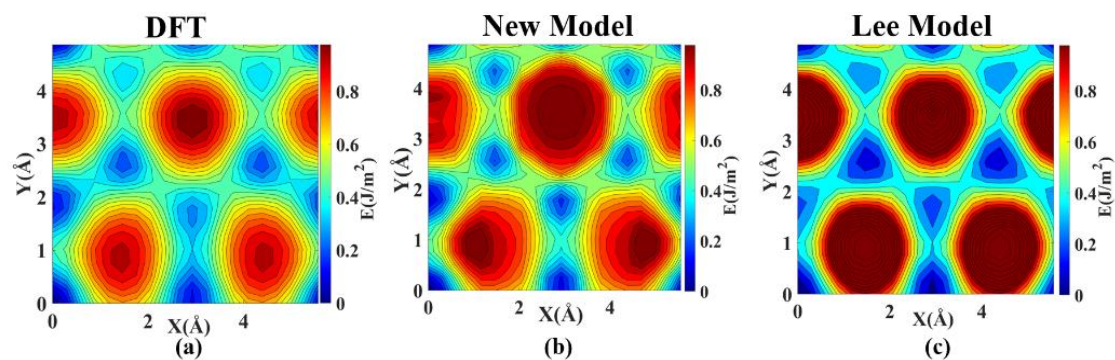


**Figure B- 3:** 2D GSFE plots of the Al doped bulk Ti using (a) DFT, (b) MEAM model and (c) Lee model.

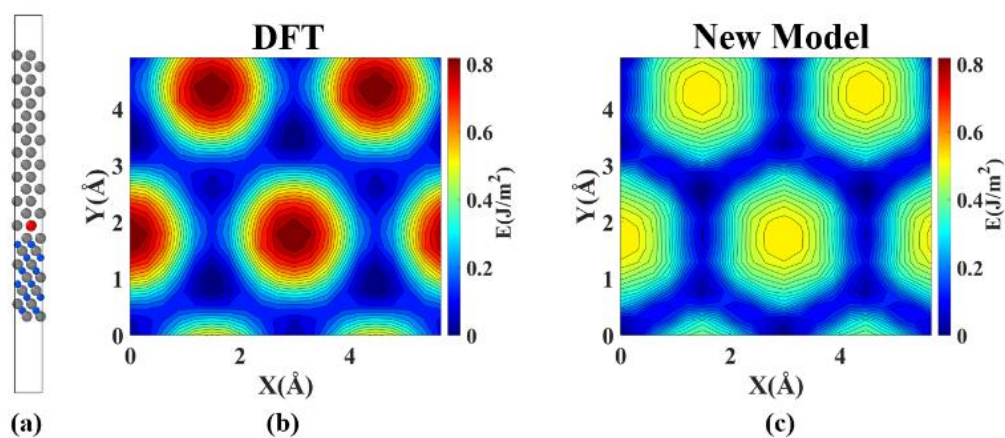


**Figure B- 4:** 2D GSFE plots of the Ti/TiN system with 1 Al atom in M =2 layer using (a) DFT and (b) new MEAM model.

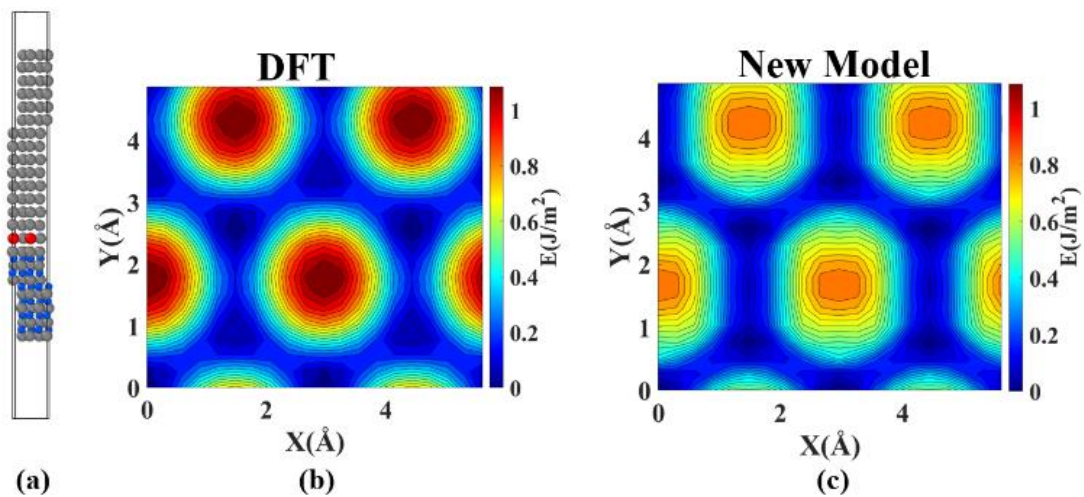


**Figure B- 5:** 2D GSFE plots of the Ti/TiN system with 2 Al atoms in M =2 layer using (a) DFT and (b) new MEAM model.

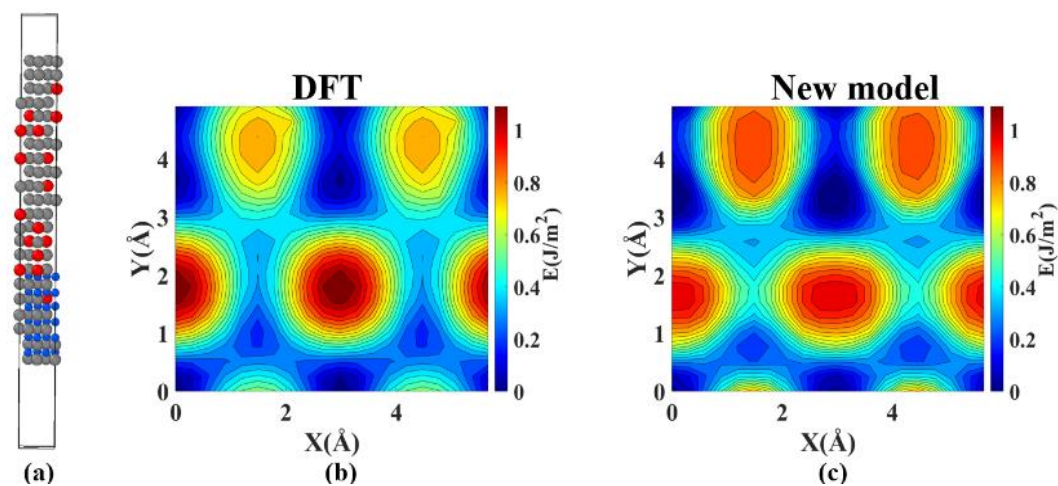


**Figure B- 6:** 2D GSFE plots of the Ti/TiN system with 16 Al atoms using (a) DFT and (b) new MEAM model.

## BIBLIOGRAPHY

- [1] N. Chawla, D.R.P. Singh, Y.L. Shen, G. Tang, K.K. Chawla, Indentation mechanics and fracture behavior of metal/ceramic nanolaminate composites, *Journal of Materials Science*. 43 (2008) 4383–4390. <https://doi.org/10.1007/S10853-008-2450-3>.
- [2] R. Darolia, Thermal barrier coatings technology: critical review, progress update, remaining challenges and prospects, *International Materials Reviews*. 58 (2013) 315–348. <https://doi.org/10.1179/1743280413Y.0000000019>.
- [3] S.B. Sinnott, E.C. Dickey, Ceramic/metal interface structures and their relationship to atomic- and meso-scale properties, *Materials Science and Engineering: R: Reports*. 43 (2003) 1–59. <https://doi.org/10.1016/j.mser.2003.09.001>.
- [4] M.W. Finnis, The theory of metal-ceramic interfaces, *Journal of Physics Condensed Matter*. 8 (1996) 5811–5836. <https://doi.org/10.1088/0953-8984/8/32/003>.
- [5] J.S. Moya, S. Lopez-Esteban, C. Pecharromás, The challenge of ceramic/metal microcomposites and nanocomposites, *Progress in Materials Science*. 52 (2007) 1017–1090. <https://doi.org/10.1016/J.PMATSCI.2006.09.003>.
- [6] N. Li, X.-Y.Y. Liu, Review: mechanical behavior of metal/ceramic interfaces in nanolayered composites—experiments and modeling, *Journal of Materials Science*. 53 (2018) 5562–5583. <https://doi.org/10.1007/s10853-017-1767-1>.
- [7] N.P. Padture, Thermal Barrier Coatings for Gas-Turbine Engine Applications, *Science*. 296 (2002) 280–284. <https://doi.org/10.1126/science.1068609>.
- [8] A. Leyland, A. Matthews, On the significance of the H/E ratio in wear control: a nanocomposite coating approach to optimised tribological behaviour, *Wear*. 246 (2000) 1–11. [https://doi.org/10.1016/s0043-1648\(00\)00488-9](https://doi.org/10.1016/s0043-1648(00)00488-9).
- [9] H. Bian, X. Song, S. Hu, Y. Lei, Y. Jiao, S. Duan, J. Feng, W. Long, Microstructure Evolution and Mechanical Properties of Titanium/Alumina Brazed Joints for Medical Implants, *Metals (Basel)*. 9 (2019) 644. <https://doi.org/10.3390/met9060644>.
- [10] M.C. Halbig, M.H. Jaskowiak, J.D. Kiser, D. Zhu, Evaluation of ceramic matrix composite technology for aircraft turbine engine applications, in: 51st AIAA Aerospace Sciences Meeting Including the New Horizons Forum and Aerospace Exposition. 0539 (2013) 1-11. <https://doi.org/10.2514/6.2013-539>.

- [11] H.C. Lee, K. Kim, S.Y. Han, S.K. Choi, E. Lee, M. Jo, M.S. Yoo, K. Cho, Highly Conductive Flexible Metal-Ceramic Nanolaminate Electrode for High-Performance Soft Electronics, *ACS Applied Materials and Interfaces*. 11 (2019) 2211–2217. <https://doi.org/10.1021/acsami.8b14821>.
- [12] D.A. Chance, D.L. Wilcox, Metal-ceramic constraints for multilayer electronic packages, *Proceedings of the IEEE*. 59 (1971) 1455–1462. <https://doi.org/10.1109/PROC.1971.8454>.
- [13] M.A. Siddiq, Modelling of crystal plasticity effects in the fracture of a metal/ceramic interface - bridging the length scales, PhD Dissertation, University of Stuttgart (2006).
- [14] P. Hynes, N. Rajesh Jesudoss Nagaraj, R.M. Selvaraj, Finite element based thermal modeling of friction welding of dissimilar materials, *International Journal of Modern Physics*. 22 (2013) 196–202. <https://doi.org/10.1142/S201019451301012X>.
- [15] J.M. Howe, Bonding, structure, and properties of metal/ceramic interfaces: Part 1 Chemical bonding, chemical reaction, and interfacial structure, *International Material Reviews*. 38 (2013) 233–256. <https://doi.org/10.1179/IMR.1993.38.5.233>.
- [16] K.K. Chawla, *Composite Materials*, Springer New York, New York, NY (1987). <https://doi.org/10.1007/978-1-4757-3912-1>.
- [17] A.G. Evans, D.R. Mumm, J.W. Hutchinson, G.H. Meier, F.S. Pettit, Mechanisms controlling the durability of thermal barrier coatings, *Progress in Materials Science*. 46 (2001) 505–553. [https://doi.org/10.1016/S0079-6425\(00\)00020-7](https://doi.org/10.1016/S0079-6425(00)00020-7).
- [18] C. de Mello Donegá, *The nanoscience paradigm: Size matters! Nanoparticles: Workhorses of Nanoscience*, Springer. 9783662448236 (2014) 1–12. [https://doi.org/10.1007/978-3-662-44823-6\\_1/COVER/](https://doi.org/10.1007/978-3-662-44823-6_1/COVER/).
- [19] A. Misra, M. Verdier, H. Kung, J.D. Embury, J.P. Hirth, Deformation mechanism maps for polycrystalline metallic multilayers, *Scripta Materialia*. 41 (1999) 973–979. [https://doi.org/10.1016/S1359-6462\(99\)00239-0](https://doi.org/10.1016/S1359-6462(99)00239-0).
- [20] D. Bhattacharyya, N.A. Mara, P. Dickerson, R.G. Hoagland, A. Misra, Compressive flow behavior of Al–TiN multilayers at nanometer scale layer thickness, *Acta Materialia*. 59 (2011) 3804–3816. <https://doi.org/10.1016/J.ACTAMAT.2011.02.036>.
- [21] Y. Mu, X. Zhang, J.W. Hutchinson, W.J. Meng, Measuring critical stress for shear failure of interfacial regions in coating/interlayer/substrate systems through a micro-pillar testing protocol, *Journal of Materials Research*. 32 (2017) 1421–1431. <https://doi.org/10.1557/jmr.2016.516>.

- [22] W.J. Meng, S. Shao, Experimentation and Modeling of Mechanical Integrity and Instability at Metal/Ceramic Interfaces, in: Handbook of Nonlocal Continuum Mechanics for Materials and Structures, Springer International Publishing, Cham, (2019) 153-210. [https://doi.org/10.1007/978-3-319-58729-5\\_50](https://doi.org/10.1007/978-3-319-58729-5_50).
- [23] W. Wunderlich, The Atomistic Structure of Metal/Ceramic Interfaces Is the Key Issue for Developing Better Properties, *Metals*. 4 (2014) 410–427. <https://doi.org/10.3390/MET4030410>.
- [24] X.Q. Fu, L.H. Liang, Y.G. Wei, Modeling of atomistic scale shear failure of Ag/MgO interface with misfit dislocation network, *Computational Materials Science*. 170 (2019) 109151. <https://doi.org/10.1016/j.commatsci.2019.109151>.
- [25] J. Wang, R.G. Hoagland, J.P. Hirth, A. Misra, Atomistic modeling of the interaction of glide dislocations with “weak” interfaces, *Acta Materialia*. 56 (2008) 5685–5693. <https://doi.org/10.1016/j.actamat.2008.07.041>.
- [26] J. Wang, R.G. Hoagland, J.P. Hirth, A. Misra, Atomistic simulations of the shear strength and sliding mechanisms of copper–niobium interfaces, *Acta Materialia*. 56 (2008) 3109–3119. <https://doi.org/10.1016/j.actamat.2008.03.003>.
- [27] W. Zhang, J.R. Smith, Nonstoichiometric Interfaces and Al<sub>2</sub>O<sub>3</sub> Adhesion with Al and Ag, *Physical Review Letters*. 85 (2000) 3225–3228. <https://doi.org/10.1103/physrevlett.85.3225>.
- [28] Y.L. Su, S.H. Yao, Z.L. Leu, C.S. Wei, C.T. Wu, Comparison of tribological behavior of three films—TiN, TiCN and CrN—grown by physical vapor deposition, *Wear*. 213 (1997) 165–174. [https://doi.org/10.1016/s0043-1648\(97\)00182-8](https://doi.org/10.1016/s0043-1648(97)00182-8).
- [29] J. Horník, S. Krum, D. Tondl, M. Puchnin, P. Sachr, L. Cvrček, Multilayer coatings Ti/TiN, Cr/CrN AND W/WN deposited by magnetron sputtering for improvement of adhesion to base materials, *Acta Polytechnica*. 55 (2015) 388–392. <https://doi.org/10.14311/AP.2015.55.0388>.
- [30] I. Kim, F. Khatkhatay, L. Jiao, G. Swadener, J.I. Cole, J. Gan, H. Wang, TiN-based coatings on fuel cladding tubes for advanced nuclear reactors, *Journal of Nuclear Materials*. 429 (2012) 143–148. <https://doi.org/10.1016/j.jnucmat.2012.05.001>.
- [31] J.Th.M. de Hosson, H.B. Groen, B.J. Kooi, W.P. Velinga, Metal-Ceramic Interfaces Studied with High Resolution Transmission Electron Microscopy, Impact of Electron and Scanning Probe Microscopy on Materials Research. (1999) 135–159. [https://doi.org/10.1007/978-94-011-4451-3\\_6](https://doi.org/10.1007/978-94-011-4451-3_6).

- [32] A.I. Vainshtein, V.I. Zakharov, D.A. Shashkov, D.N. Seidman, Z. Cao, R.C. Hwa, Atomic Scale Studies of Segregation at Ceramic/Metal Heterophase Interfaces, *Physical Review Letters*. 75 (1995) 3588.  
<https://doi.org/10.1103/PhysRevLett.75.3588.2>.
- [33] J. Bruley, R. Brydson, H. Miillejans, J. Mayer, G. Gutekunst, W. Madei, B. Knauss, M. Riihle, Investigations of the chemistry and bonding at niobium sapphire interfaces, *Journal of Materials Research*. 9 (1994) 2574–2583.  
<https://doi.org/10.1557/JMR.1994.2574>.
- [34] X. Zhang, B. Zhang, Y. Mu, S. Shao, C.D. Wick, B.R. Ramachandran, W.J. Meng, Mechanical failure of metal/ceramic interfacial regions under shear loading, *Acta Materialia*. 138 (2017) 224–236. <https://doi.org/10.1016/j.actamat.2017.07.053>.
- [35] S. Lotfian, M. Rodríguez, K.E. Yazzie, N. Chawla, J. Llorca, J.M. Molina-Aldareguía, High temperature micropillar compression of Al/SiC nanolaminates, *Acta Materialia*. 61 (2013) 4439–4451.  
<https://doi.org/10.1016/J.ACTAMAT.2013.04.013>.
- [36] G. Abadias, S. Dub, R. Shmegeera, Nanoindentation hardness and structure of ion beam sputtered TiN, W and TiN/W multilayer hard coatings, *Surface and Coatings Technology*. 200 (2006) 6538–6543.  
<https://doi.org/10.1016/J.SURFCOAT.2005.11.053>.
- [37] J.L. He, W.Z. Li, H.D. Li, C.H. Liu, Plastic properties of nano-scale ceramic–metal multilayers, *Surface and Coatings Technology*. 103–104 (1998) 276–280.  
[https://doi.org/10.1016/S0257-8972\(98\)00423-X](https://doi.org/10.1016/S0257-8972(98)00423-X).
- [38] G.A. Zhang, Z.G. Wu, M.X. Wang, X.Y. Fan, J. Wang, P.X. Yan, Structure evolution and mechanical properties enhancement of Al/AlN multilayer, *Applied Surface Science*. 253 (2007) 8835–8840.  
<https://doi.org/10.1016/J.APSUSC.2007.04.039>.
- [39] J. Wang, W.Z. Li, H. de Li, B. Shi, J. bin Luo, Nanoindentation study on the mechanical properties of TiC/Mo multilayers, *Thin Solid Films*. 366 (2000) 117–120. [https://doi.org/10.1016/S0040-6090\(99\)00968-2](https://doi.org/10.1016/S0040-6090(99)00968-2).
- [40] L.S. Wen, R.F. Huang, L.P. Guo, J. Gong, T.Y. Wei, Y.Z. Chuang, Microstructure and mechanical properties of metal/ceramic Ti/TiN multilayers, *Journal of Magnetism and Magnetic Materials*. 126 (1993) 200–202.  
[https://doi.org/10.1016/0304-8853\(93\)90580-U](https://doi.org/10.1016/0304-8853(93)90580-U).
- [41] G. Abadias, F. Pailloux, S.N. Dub, Epitaxial growth and mechanical properties of (001) ZrN/W nanolaminates, *Surface and Coatings Technology*. 202 (2008) 3683–3687. <https://doi.org/10.1016/J.SURFCOAT.2008.01.013>.

- [42] S.A. Barnett, A. Madan, Hardness and stability of metal–nitride nanoscale multilayers, *Scripta Materialia*. 50 (2004) 739–744.  
<https://doi.org/10.1016/J.SCRIPTAMAT.2003.11.042>.
- [43] A.G. Evans, M. Rühle, M. Turwitt, On the mechanics of failure in ceramic/metal bonded systems, *Le Journal de Physique Colloques*. 46 (1985) C4-613-C4-626.  
<https://doi.org/10.1051/JPHYSCOL:1985466>.
- [44] K. Chen, Y. Mu, W.J. Meng, A new experimental approach for evaluating the mechanical integrity of interfaces between hard coatings and substrates, *MRS Communications*. 4 (2014) 19–23. <https://doi.org/10.1557/mrc.2014.3>.
- [45] P. Wieceński, J. Smolik, H. Garbacz, K.J. Kurzydłowski, Failure and deformation mechanisms during indentation in nanostructured Cr/CrN multilayer coatings, *Surface and Coatings Technology*. 240 (2014) 23–31.  
<https://doi.org/10.1016/j.surfcoat.2013.12.006>.
- [46] D. Li, S. Guruvenket, S. Hassani, E. Bousser, M. Azzi, J.A. Szpunar, J.E. Klemberg-Sapieha, Effect of Cr interlayer on the adhesion and corrosion enhancement of nanocomposite TiN-based coatings deposited on stainless steel 410, *Thin Solid Films*. 519 (2011) 3128–3134.  
<https://doi.org/10.1016/j.tsf.2010.12.020>.
- [47] W. Guan, H. Zhu, W. Zhu, Z. Chen, J. Liu, X. Shi, X. Wang, Effects of the different interlayer deposition processes on the microstructure of Cr/TiN coating, *Materials Research Express*. 6 (2019) 126444. <https://doi.org/10.1088/2053-1591/ab67f4>.
- [48] N.D. Nam, M.J. Kim, D.S. Jo, J.G. Kim, D.H. Yoon, Corrosion protection of Ti/TiN, Cr/TiN, Ti/CrN, and Cr/CrN multi-coatings in simulated proton exchange membrane fuel cell environment, *Thin Solid Films*. 545 (2013) 380–384.  
<https://doi.org/10.1016/j.tsf.2013.07.056>.
- [49] S. Han, J.H. Lin, S.H. Tsai, S.C. Chung, D.Y. Wang, F.H. Lu, H.C. Shih, Corrosion and tribological studies of chromium nitride coated on steel with an interlayer of electroplated chromium, *Surface and Coatings Technology*. 133–134 (2000) 460–465. [https://doi.org/10.1016/S0257-8972\(00\)00979-8](https://doi.org/10.1016/S0257-8972(00)00979-8).
- [50] R. Bayón, A. Igartua, X. Fernández, R. Martínez, R.J. Rodríguez, J.A. García, A. de Frutos, M.A. Arenas, J. de Damborenea, Corrosion-wear behaviour of PVD Cr/CrN multilayer coatings for gear applications, *Tribology International*. 42 (2009) 591–599. <https://doi.org/10.1016/j.triboint.2008.06.015>.

- [51] T. Polcar, R. Martinez, T. Vítů, L. Kopecký, R. Rodriguez, A. Cavaleiro, High temperature tribology of CrN and multilayered Cr/CrN coatings, *Surface and Coatings Technology*. 203 (2009) 3254–3259. <https://doi.org/10.1016/j.surfcoat.2009.04.005>.
- [52] J.H. Park, H.G. Kim, J. Yong Park, Y. il Jung, D.J. Park, Y.H. Koo, High temperature steam-oxidation behavior of arc ion plated Cr coatings for accident tolerant fuel claddings, *Surface and Coatings Technology*. 280 (2015) 256–259. <https://doi.org/10.1016/j.surfcoat.2015.09.022>.
- [53] K. Yang, B. Liao, H. Zhu, W. Zhu, H. He, Y. Liu, H. Li, X. Wang, Influence of the Cr interlayer on the microstructure of sputtered TiN coatings deposited on zirconium alloy, *Materials Research Express*. 6 (2019) 026420. <https://doi.org/10.1088/2053-1591/aaf041>.
- [54] P. Guénard, G. Renaud, B. Villette, Structure, translational state and morphology of the Ag/MgO(001) interface during its formation, *Physica B: Condensed Matter*. 221 (1996) 205–209. [https://doi.org/10.1016/0921-4526\(95\)00925-6](https://doi.org/10.1016/0921-4526(95)00925-6).
- [55] O. Robach, G. Renaud, A. Barbier, Structure and morphology of the Ag/MgO(001) interface during *in situ* growth at room temperature, *Physical Review B*. 60 (1999) 5858. <https://doi.org/10.1103/PhysRevB.60.5858>.
- [56] H. Meltzman, D. Mordehai, W.D. Kaplan, Solid–solid interface reconstruction at equilibrated Ni–Al<sub>2</sub>O<sub>3</sub> interfaces, *Acta Materialia*. 60 (2012) 4359–4369. <https://doi.org/10.1016/j.actamat.2012.04.037>.
- [57] D. Cheng, Z.J. Yan, L. Yan, Misfit dislocation network in Cu/Ni multilayers and its behaviors during scratching, *Thin Solid Films*. 515 (2007) 3698–3703. <https://doi.org/10.1016/j.tsf.2006.10.001>.
- [58] M. Tamura, Two groups of misfit dislocations in GaAs on Si, *Applied Physics A* 1996 63:4. 63 (1996) 359–370. <https://doi.org/10.1007/BF01567327>.
- [59] B. Jelinek, S. Groh, M.F. Horstemeyer, J. Houze, S.G. Kim, G.J. Wagner, A. Moitra, M.I. Baskes, Modified embedded atom method potential for Al, Si, Mg, Cu, and Fe alloys, *Physical Review B*. 85 (2012) 245102. <https://doi.org/10.1103/PhysRevB.85.245102>.
- [60] I. Kim, F. Khatkhatay, L. Jiao, G. Swadener, J.I. Cole, J. Gan, H. Wang, TiN-based coatings on fuel cladding tubes for advanced nuclear reactors, *Journal of Nuclear Materials*. 429 (2012) 143–148. <https://doi.org/10.1016/j.jnucmat.2012.05.001>.

- [61] A.G. Evans, J.W. Hutchinson, Y. Wei, Interface adhesion: effects of plasticity and segregation, *Acta Materialia*. 47 (1999) 4093–4113. [https://doi.org/10.1016/s1359-6454\(99\)00269-4](https://doi.org/10.1016/s1359-6454(99)00269-4).
- [62] D.J. Siegel, L.G. Hector, J.B. Adams, First-principles study of metal–carbide/nitride adhesion: Al/VC vs. Al/VN, *Acta Materialia*. 50 (2002) 619–631. [https://doi.org/10.1016/s1359-6454\(01\)00361-5](https://doi.org/10.1016/s1359-6454(01)00361-5).
- [63] D. Bhattacharyya, X.-Y. Liu, A. Genc, H.L. Fraser, R.G. Hoagland, A. Misra, Heterotwin formation during growth of nanolayered Al-TiN composites, *Applied Physics Letters*. 96 (2010) 093113. <https://doi.org/10.1063/1.3330889>.
- [64] N. Li, S.K. Yadav, J. Wang, X.-Y. Liu, A. Misra, Growth and Stress-induced Transformation of Zinc blende AlN Layers in Al-AlN-TiN Multilayers, *Sci Rep*. 5 (2015) 18554. <https://doi.org/10.1038/srep18554>.
- [65] Z. Li, S. Yadav, Y. Chen, N. Li, X.-Y. Liu, J. Wang, S. Zhang, J.K. Baldwin, A. Misra, N. Mara, Mechanically controlling the reversible phase transformation from zinc blende to wurtzite in AlN, *Materials Research Letters*. 5 (2017) 426–432. <https://doi.org/10.1080/21663831.2017.1303793>.
- [66] H.Z. Zhang, L.M. Liu, S.Q. Wang, First-principles study of the tensile and fracture of the Al/TiN interface, *Computational Materials Science*. 38 (2007) 800–806. <https://doi.org/10.1016/j.commatsci.2006.05.017>.
- [67] S.K. Yadav, R. Ramprasad, A. Misra, X.-Y. Liu, First-principles study of shear behavior of Al, TiN, and coherent Al/TiN interfaces, *Journal of Applied Physics*. 111 (2012) 083505. <https://doi.org/10.1063/1.3703663>.
- [68] J. Hartford, Interface energy and electron structure for Fe/VN, *Physical Review B*. 61 (2000) 2221. <https://doi.org/10.1103/PhysRevB.61.2221>.
- [69] S. V. Dudiy, B.I. Lundqvist, First-principles density-functional study of metal-carbonitride interface adhesion: Co/TiC(001) and Co/TiN(001), *Physical Review B*. 64 (2001) 045403. <https://doi.org/10.1103/PhysRevB.64.045403>.
- [70] L.M. Liu, S.Q. Wang, H.Q. Ye, Adhesion of metal–carbide/nitride interfaces: Al/TiC and Al/TiN, *Journal of Physics: Condensed Matter*. 15 (2003) 8103. <https://doi.org/10.1088/0953-8984/15/47/013>.
- [71] A. Arya, E.A. Carter, Structure, bonding, and adhesion at the TiC(100)/Fe(110) interface from first principles, *The Journal of Chemical Physics*. 118 (2003) 8982. <https://doi.org/10.1063/1.1565323>.

- [72] D.J. Siegel, L.G. Hector, J.B. Adams, *Ab initio* study of Al-ceramic interfacial adhesion, *Physical Review B*. 67 (2003) 092105.  
<https://doi.org/10.1103/PhysRevB.67.092105>.
- [73] L.M. Liu, S.Q. Wang, H.Q. Ye, First-principles study of polar Al/TiN(1 1 1) interfaces, *Acta Materialia*. 52 (2004) 3681–3688.  
<https://doi.org/10.1016/J.ACTAMAT.2004.04.022>.
- [74] A. Karton, P.R. Spackman, Evaluation of density functional theory for a large and diverse set of organic and inorganic equilibrium structures, *Journal of Computational Chemistry*. 42 (2021) 1590–1601.  
<https://doi.org/10.1002/JCC.26698>.
- [75] F. Legrain, S. Manzhos, Understanding the difference in cohesive energies between alpha and beta tin in DFT calculations, *AIP Advances*. 6 (2016) 045116.  
<https://doi.org/10.1063/1.4948434>.
- [76] E. Lewin, M. Rsander, M. Klintonberg, A. Bergman, O. Eriksson, U. Jansson, Design of the lattice parameter of embedded nanoparticles, *Chemical Physics Letters*. 496 (2010) 95–99. <https://doi.org/10.1016/J.CPLETT.2010.07.013>.
- [77] D. Wu, Y. Chen, S. Manna, K. Talley, A. Zakutayev, G.L. Brennecke, C. V. Ciobanu, P. Constantine, C.E. Packard, Characterization of Elastic Modulus Across the (Al<sub>1-x</sub>Sc<sub>x</sub>)N System Using DFT and Substrate-Effect-Corrected Nanoindentation, *IEEE Transactions on Ultrasonics, Ferroelectrics, and Frequency Control*. 65 (2018) 2167–2175. <https://doi.org/10.1109/TUFFC.2018.2862240>.
- [78] D.G. (David G.) Pettifor, A. Cottrell, E. Electron theory in alloy design, *Institute of Materials London* (1992) 1-311.
- [79] P. Panjan, B. Navinšek, A. Cvelbar, A. Zalar, I. Milošev, Oxidation of TiN, ZrN, TiZrN, CrN, TiCrN and TiN/CrN multilayer hard coatings reactively sputtered at low temperature, *Thin Solid Films*. 281–282 (1996) 298–301.  
[https://doi.org/10.1016/0040-6090\(96\)08663-4](https://doi.org/10.1016/0040-6090(96)08663-4).
- [80] S.L. Shang, W.Y. Wang, B.C. Zhou, Y. Wang, K.A. Darling, L.J. Kecskes, S.N. Mathaudhu, Z.K. Liu, Generalized stacking fault energy, ideal strength and twinnability of dilute Mg-based alloys: A first-principles study of shear deformation, *Acta Materialia*. 67 (2014) 168–180.  
<https://doi.org/10.1016/J.ACTAMAT.2013.12.019>.
- [81] A.S. Mohammad Miraz, S. Sun, S. Shao, W.J. Meng, B.R. Ramachandran, C.D. Wick, Computational study of metal/ceramic interfacial adhesion and barriers to shear displacement, *Computational Materials Science*. 168 (2019) 104–115.  
<https://doi.org/10.1016/j.commat.2019.06.006>.

- [82] A.I. Duff, M.W. Finnis, P. Maugis, B.J. Thijsse, M.H.F. Sluiter, MEAMfit: A reference-free modified embedded atom method (RF-MEAM) energy and force-fitting code, *Computer Physics Communications*. 196 (2015) 439–445. <https://doi.org/10.1016/J.CPC.2015.05.016>.
- [83] S. Shao, J. Wang, A. Misra, Energy minimization mechanisms of semi-coherent interfaces, *Journal of Applied Physics*. 116 (2014) 23508. <https://doi.org/10.1063/1.4889927>.
- [84] B.-J. Lee, M.I. Baskes, Second nearest-neighbor modified embedded-atom-method potential, *Physical Review B*. 62 (2000) 8564–8567. <https://doi.org/10.1103/physrevb.62.8564>.
- [85] M.S. Daw, M.I. Baskes, Embedded-atom method: Derivation and application to impurities, surfaces, and other defects in metals, *Physical Review B*. 29 (1984) 6443–6453. <https://doi.org/10.1103/physrevb.29.6443>.
- [86] S.M. Foiles, M.I. Baskes, M.S. Daw, Embedded-atom-method functions for the fcc metals Cu, Ag, Au, Ni, Pd, Pt, and their alloys, *Physical Review B*. 33 (1986) 7983–7991. <https://doi.org/10.1103/physrevb.33.7983>.
- [87] M.I. Baskes, Application of the Embedded-Atom Method to Covalent Materials: A Semiempirical Potential for Silicon, *Physical Review Letters*. 59 (1987) 2666–2669. <https://doi.org/10.1103/physrevlett.59.2666>.
- [88] M.S. Daw, M.I. Baskes, Semiempirical, Quantum Mechanical Calculation of Hydrogen Embrittlement in Metals, *Physical Review Letters*. 50 (1983) 1285. <https://doi.org/10.1103/PhysRevLett.50.1285>.
- [89] A.E. Carlsson, Beyond Pair Potentials in Elemental Transition Metals and Semiconductors, *Solid State Physics - Advances in Research and Applications*. 43 (1990) 1–91. [https://doi.org/10.1016/S0081-1947\(08\)60323-9](https://doi.org/10.1016/S0081-1947(08)60323-9).
- [90] M.S. Daw, S.M. Foiles, M.I. Baskes, The embedded-atom method: a review of theory and applications, *Materials Science Reports*. 9 (1993) 251–310. [https://doi.org/10.1016/0920-2307\(93\)90001-u](https://doi.org/10.1016/0920-2307(93)90001-u).
- [91] M.I. Baskes, R.A. Johnson, Modified embedded atom potentials for HCP metals, *Modelling and Simulation in Materials Science and Engineering*. 2 (1994) 147–163. <https://doi.org/10.1088/0965-0393/2/1/011>.
- [92] M.I. Baskes, J.S. Nelson, A.F. Wright, Semiempirical modified embedded-atom potentials for silicon and germanium, *Physical Review B*. 40 (1989) 6085–6100. <https://doi.org/10.1103/physrevb.40.6085>.

- [93] B.-J. Lee, W.-S. Ko, H.-K. Kim, E.-H. Kim, The modified embedded-atom method interatomic potentials and recent progress in atomistic simulations, *Calphad*. 34 (2010) 510–522. <https://doi.org/10.1016/j.calphad.2010.10.007>.
- [94] X. Yuan, K. Takahashi, Y. Yin, T. Onzawa, Development of modified embedded atom method for a bcc metal: lithium, *Modelling and Simulation in Materials Science and Engineering*. 11 (2003) 447–456. <https://doi.org/10.1088/0965-0393/11/4/303>.
- [95] B.J. Lee, A modified embedded-atom method interatomic potential for the Fe–C system, *Acta Materialia*. 54 (2006) 701–711. <https://doi.org/10.1016/J.ACTAMAT.2005.09.034>.
- [96] Y.-K. Kim, H.-K. Kim, W.-S. Jung, B.-J. Lee, Atomistic modeling of the Ti–Al binary system, *Computational Materials Science*. C (2016) 1–8. <https://doi.org/10.1016/J.COMMATSCI.2016.03.038>.
- [97] B.J. Lee, J.H. Shim, H.M. Park, J.H. Shim, A semi-empirical atomic potential for the Fe-Cr binary system, *Calphad*. 25 (2001) 527–534. [https://doi.org/10.1016/S0364-5916\(02\)00005-6](https://doi.org/10.1016/S0364-5916(02)00005-6).
- [98] Y.K. Kim, W.S. Jung, B.J. Lee, Modified embedded-atom method interatomic potentials for the Ni–Co binary and the Ni–Al–Co ternary systems, *Modelling and Simulation in Materials Science and Engineering*. 23 (2015) 055004. <https://doi.org/10.1088/0965-0393/23/5/055004>.
- [99] J. Wang, B.J. Lee, Second-nearest-neighbor modified embedded-atom method interatomic potential for V-M (M = Cu, Mo, Ti) binary systems, *Computational Materials Science*. 188 (2021) 110177. <https://doi.org/10.1016/J.COMMATSCI.2020.110177>.
- [100] C.L. Kuo, P. Clancy, Development of atomistic MEAM potentials for the silicon-oxygen-gold ternary system, *Modelling and Simulation in Materials Science and Engineering*. 13 (2005) 1309–1329. <https://doi.org/10.1088/0965-0393/13/8/008>.
- [101] H.-K. Kim, W.-S. Jung, B.-J. Lee, Modified embedded-atom method interatomic potentials for the Fe–Ti–C and Fe–Ti–N ternary systems, *Acta Materialia*. 57 (2009) 3140–3147. <https://doi.org/10.1016/j.actamat.2009.03.019>.
- [102] F. Kong, R.C. Longo, C. Liang, D.H. Yeon, Y. Zheng, J.H. Park, S.G. Doo, K. Cho, CT-MEAM interatomic potential of the Li–Ni–O ternary system for Li-ion battery cathode materials, *Computational Materials Science*. 127 (2017) 128–135. <https://doi.org/10.1016/J.COMMATSCI.2016.10.030>.

- [103] S. Ding, X. Wang, A systematic study on the MEAM interatomic potentials of the transition metal nitrides TMNs (TM=Ti, V, Cr, Fe) binary systems, *Journal of Alloys and Compounds*. 805 (2019) 1081–1089.  
<https://doi.org/10.1016/j.jallcom.2019.07.114>.
- [104] B. Narayanan, K. Sasikumar, Z.G. Mei, A. Kinaci, F.G. Sen, M.J. Davis, S.K. Gray, M.K.Y. Chan, S.K.R.S. Sankaranarayanan, Development of a Modified Embedded Atom Force Field for Zirconium Nitride Using Multi-Objective Evolutionary Optimization, *Journal of Physical Chemistry C*. 120 (2016) 17475–17483. <https://doi.org/10.1021/acs.jpcc.6b05296>.
- [105] Y.-M. Kim, B.-J. Lee, Modified embedded-atom method interatomic potentials for the Ti–C and Ti–N binary systems, *Acta Materialia*. 56 (2008) 3481–3489.  
<https://doi.org/10.1016/j.actamat.2008.03.027>.
- [106] I. Salehinia, S. Shao, J. Wang, H.M. Zbib, Plastic Deformation of Metal/Ceramic Nanolayered Composites, *JOM*. 66 (2014) 2078–2085.  
<https://doi.org/10.1007/s11837-014-1132-7>.
- [107] I. Salehinia, J. Wang, D.F. Bahr, H.M. Zbib, Molecular dynamics simulations of plastic deformation in Nb/NbC multilayers, *International Journal of Plasticity*. 59 (2014) 119–132. <https://doi.org/10.1016/J.IJPLAS.2014.03.010>.
- [108] M. Damadam, S. Shao, I. Salehinia, G. Ayoub, H.M. Zbib, Molecular dynamics simulations of mechanical behavior in nanoscale ceramic–metallic multilayer composites, *Material Research Letters*. 5 (2017) 306–313.  
<https://doi.org/10.1080/21663831.2016.1275864>.
- [109] I. Aslam, M.I. Baskes, D.E. Dickel, S. Adibi, B. Li, H. Rhee, M. Asle Zaeem, M.F. Horstemeyer, Thermodynamic and kinetic behavior of low-alloy steels: An atomic level study using an Fe-Mn-Si-C modified embedded atom method (MEAM) potential, *Materialia (Oxf)*. 8 (2019) 100473.  
<https://doi.org/10.1016/j.mtla.2019.100473>.
- [110] A.E. Gheribi, Molecular dynamics study of stable and undercooled liquid zirconium based on MEAM interatomic potential, *Materials Chemistry and Physics*. 116 (2009) 489–496. <https://doi.org/10.1016/j.matchemphys.2009.04.020>.
- [111] E.Y. Chen, R. Dingreville, C. Deo, Misfit dislocation networks in semi-coherent miscible phase boundaries: An example for U–Zr interfaces, *Computational Materials Science*. 154 (2018) 194–203.  
<https://doi.org/10.1016/j.commatsci.2018.07.065>.

- [112] B.-J.J. Lee, M.I. Baskes, H. Kim, Y.K. Cho, B.-J.J. Lee, H. Kim, Y.K. Cho, Second nearest-neighbor modified embedded atom method potentials for bcc transition metals, *Physical Review B*. 64 (2001) 184102.  
<https://journals.aps.org/prb/abstract/10.1103/PhysRevB.64.184102>.
- [113] M. Damadam, S. Shao, G. Ayoub, H.M. Zbib, Recent advances in modeling of interfaces and mechanical behavior of multilayer metallic/ceramic composites, *Journal of Materials Science*. 53 (2017) 5604–5617.  
<https://doi.org/10.1007/s10853-017-1704-3>.
- [114] J. Wang, R. Zhang, C. Zhou, I.J. Beyerlein, A. Misra, Characterizing interface dislocations by atomically informed Frank-Bilby theory, *Journal of Materials Research*. 28 (2013) 1646–1657. <https://doi.org/10.1557/JMR.2013.34>.
- [115] J.H. Rose, J.R. Smith, F. Guinea, J. Ferrante, Universal features of the equation of state of metals, *Physical Review B*. 29 (1984) 2963–2969.  
<https://doi.org/10.1103/physrevb.29.2963>.
- [116] M. Timonova, B.J. Thijsse, Optimizing the MEAM potential for silicon, *Modelling and Simulation in Materials Science and Engineering*. 19 (2010) 015003.  
<https://doi.org/10.1088/0965-0393/19/1/015003>.
- [117] M.I. Baskes, Modified embedded-atom potentials for cubic materials and impurities, *Physical Review B*. 46 (1992) 2727.  
<https://doi.org/10.1103/PhysRevB.46.2727>.
- [118] M.I. Baskes, Determination of modified embedded atom method parameters for nickel, *Materials Chemistry and Physics*. 50 (1997) 152–158.  
[https://doi.org/10.1016/S0254-0584\(97\)80252-0](https://doi.org/10.1016/S0254-0584(97)80252-0).
- [119] S. Sun, B.R. Ramachandran, C.D. Wick, Solid, liquid, and interfacial properties of TiAl alloys: parameterization of a new modified embedded atom method model, *Journal of Physics: Condensed Matter*. 30 (2018) 75002.  
<https://doi.org/10.1088/1361-648x/aaa52c>.
- [120] A.S.M. Miraz, W.J. Meng, B.R. Ramachandran, C.D. Wick, Computational observation of the strengthening of Cu/TiN metal/ceramic interfaces by sub-nanometer interlayers and dopants, *Applied Surface Science*. 554 (2021) 149562.  
<https://doi.org/10.1016/j.apsusc.2021.149562>.
- [121] A.S.M. Miraz, N. Dhariwal, W.J. Meng, B.R. Ramachandran, C.D. Wick, Development and application of interatomic potentials to study the stability and shear strength of Ti/TiN and Cu/TiN interfaces, *Materials & Design*. 196 (2020) 109123. <https://doi.org/10.1016/j.matdes.2020.109123>.

- [122] S.K. Yadav, S. Shao, J. Wang, X.-Y. Liu, Structural modifications due to interface chemistry at metal-nitride interfaces, *Scientific Reports*. 5 (2015) 17380. <https://doi.org/10.1038/srep17380>.
- [123] V. Bonu, M. Jeevitha, V. Praveen Kumar, H.C. Barshilia, Nanolayered multilayer Ti/TiN coatings: Role of bi-layer thickness and annealing on solid particle erosion behaviour at elevated temperature, *Surface and Coatings Technology*. 357 (2019) 204–211. <https://doi.org/10.1016/j.surfcoat.2018.10.007>.
- [124] W. Yang, G. Ayoub, I. Salehinia, B. Mansoor, H. Zbib, The effect of layer thickness ratio on the plastic deformation mechanisms of nanoindented Ti/TiN nanolayered composite, *Computational Materials Science*. 154 (2018) 488–498. <https://doi.org/10.1016/j.commatsci.2018.08.021>.
- [125] Z. Nong, J. Zhu, H. Yu, Z. Lai, First principles calculation of intermetallic compounds in FeTiCoNiVCrMnCuAl system high entropy alloy, *Transactions of Nonferrous Metals Society of China*. 22 (2012) 1437–1444. [https://doi.org/10.1016/s1003-6326\(11\)61338-1](https://doi.org/10.1016/s1003-6326(11)61338-1).
- [126] L.-Z. He, J. Zhu, L. Zhang, First-principles study of structural phase transition, electronic, elastic and thermodynamic properties of C15-type Laves phase TiCr<sub>2</sub> under pressure, *Physica B: Condensed Matter*. 531 (2018) 79–84. <https://doi.org/10.1016/j.physb.2017.11.051>.
- [127] J. Hafner, Ab-initio simulations of materials using VASP: Density-functional theory and beyond, *Journal of Computational Chemistry*. 29 (2008) 2044–2078. <https://doi.org/10.1002/jcc.21057>.
- [128] J.P. Perdew, K. Burke, M. Ernzerhof, Generalized Gradient Approximation Made Simple, *Physical Review Letters*. 77 (1996) 3865–3868. <https://doi.org/10.1103/physrevlett.77.3865>.
- [129] D. Joubert, From ultrasoft pseudopotentials to the projector augmented-wave method, *Physical Review B - Condensed Matter and Materials Physics*. 59 (1999) 1758–1775. <https://doi.org/10.1103/PhysRevB.59.1758>.
- [130] H.J. Monkhorst, J.D. Pack, Special points for Brillouin-zone integrations, *Physical Review B*. 13 (1976) 5188–5192. <https://doi.org/10.1103/physrevb.13.5188>.
- [131] A.S.M. Miraz, E. Williams, W.J. Meng, B.R. Ramachandran, C.D. Wick, Improvement of Ti/TiN interfacial shear strength by doping – A first principles density functional theory study, *Applied Surface Science*. 517 (2020) 146185. <https://www.sciencedirect.com/science/article/pii/S0169433220309417>.

- [132] T. Hong, J.R. Smith, D.J. Srolovitz, Theory of metal—Ceramic adhesion, *Acta Metallurgica et Materialia*. 43 (1995) 2721–2730. [https://doi.org/10.1016/0956-7151\(94\)00457-s](https://doi.org/10.1016/0956-7151(94)00457-s).
- [133] S. Plimpton, Fast parallel algorithms for short-range molecular dynamics, *Journal of Computational Physics*. 117 (1995) 1–19. <https://doi.org/10.1006/jcph.1995.1039>.
- [134] W.G. Hoover, Canonical dynamics: Equilibrium phase-space distributions, *Physical Review A*. 31 (1985) 1695–1697. <https://doi.org/10.1103/PhysRevA.31.1695>.
- [135] S. Nosé, A unified formulation of the constant temperature molecular dynamics methods, *The Journal of Chemical Physics*. 81 (1984) 511–519. <https://doi.org/10.1063/1.447334>.
- [136] I. Salehinia, S. Shao, J. Wang, H.M. Zbib, Interface structure and the inception of plasticity in Nb/NbC nanolayered composites, *Acta Materialia*. 86 (2015) 331–340. <https://doi.org/10.1016/j.actamat.2014.12.026>.
- [137] P.K. Misra, *Physics of Condensed Matter*, Academic Press, (2010). <https://doi.org/10.1016/C2010-0-65289-8>.
- [138] C. Kittel, *Introduction to Solid State Physics*, 8th ed., John Wiley & Sons Inc., (2004). <https://doi.org/10.1119/1.1974177>.
- [139] W.-M. Choi, Y. Kim, D. Seol, B.-J. Lee, Modified embedded-atom method interatomic potentials for the Co-Cr, Co-Fe, Co-Mn, Cr-Mn and Mn-Ni binary systems, *Computational Materials Science*. 130 (2017) 121–129. <https://doi.org/10.1016/j.commatsci.2017.01.002>.
- [140] H. Ullmaier, *Atomic Defects in Metals*, Springer-Verlag, (1991). <https://doi.org/10.1007/b37800>.
- [141] W.R. Tyson, W.A. Miller, Surface free energies of solid metals: Estimation from liquid surface tension measurements, *Surface Science*. 62 (1977) 267–276. [https://doi.org/10.1016/0039-6028\(77\)90442-3](https://doi.org/10.1016/0039-6028(77)90442-3).
- [142] D.I. Bolef, J. de Klerk, Anomalies in the Elastic Constants and Thermal Expansion of Chromium Single Crystals, *Physical Review*. 129 (1963) 1063–1067. <https://doi.org/10.1103/physrev.129.1063>.
- [143] W.M. Haynes, *CRC Handbook of Chemistry and Physics*, 92nd ed., Boca Raton, FL, (2012).

- [144] F. Kong, R.C. Longo, C. Liang, Y. Nie, Y. Zheng, C. Zhang, K. Cho, Charge-transfer modified embedded atom method dynamic charge potential for Li–Co–O system, *Journal of Physics: Condensed Matter*. 29 (2017) 475903. <https://doi.org/10.1088/1361-648X/AA9420>.
- [145] K.J. Martinschitz, R. Daniel, C. Mitterer, J. Keckes, Elastic constants of fibre-textured thin films determined by X-ray diffraction, *J Appl Crystallogr.* 42 (2009) 416–428. <https://doi.org/10.1107/S0021889809011807>.
- [146] A. Pathak, A.K. Singh, Transition Metal Nitrides: A First Principles Study, *High Temperature Materials and Processes*. 35 (2016) 389–398. <https://doi.org/10.1515/http-2014-0169>.
- [147] V. Antonov, I. Iordanova, First principles study of crystallographic structure and elastic properties of chromium nitride, in: *AIP Conference Proceedings*, American Institute of Physics AIP, (2010) 1149–1154. <https://doi.org/10.1063/1.3322328>.
- [148] A. Hunter, R.F. Zhang, I.J. Beyerlein, The core structure of dislocations and their relationship to the material  $\gamma$ -surface, *Journal of Applied Physics*. 115 (2014) 134314. <https://doi.org/10.1063/1.4870462>.
- [149] S. Shao, J. Wang, Relaxation Mechanisms, Structure and Properties of Semi-Coherent Interfaces, *Metals (Basel)*. 5 (2015) 1887–1901. <https://doi.org/10.3390/met5041887>.
- [150] A. Stukowski, Structure identification methods for atomistic simulations of crystalline materials, *Modelling and Simulation in Materials Science and Engineering*. 20 (2012) 045021. <https://doi.org/10.1088/0965-0393/20/4/045021>.
- [151] C.L. Kelchner, S.J. Plimpton, J.C. Hamilton, Dislocation nucleation and defect structure during surface indentation, *Physical Review B*. 58 (1998) 11085–11088. <https://doi.org/10.1103/physrevb.58.11085>.
- [152] J. Tang, L. Feng, J.S. Zabinski, The effects of metal interlayer insertion on the friction, wear and adhesion of TiC coatings, *Surface and Coatings Technology*. 99 (1998) 242–247. [https://doi.org/10.1016/S0257-8972\(97\)00570-7](https://doi.org/10.1016/S0257-8972(97)00570-7).
- [153] I.J. Bennett, J.M. Kranenburg, W.G. Sloof, Modeling the Influence of Reactive Elements on the Work of Adhesion between Oxides and Metal Alloys, *Journal of the American Ceramic Society*. 88 (2005) 2209–2216. <https://doi.org/10.1111/J.1551-2916.2005.00408.X>.
- [154] H.S. Abdelkader, H.I. Faraoun, C. Esling, Effects of rhenium alloying on adhesion of Mo/HfC and Mo/ZrC interfaces: A first-principles study, *Journal of Applied Physics*. 110 (2011) 044901. <https://doi.org/10.1063/1.3624580>.

- [155] C.A. Leon, V.H. Lopez, E. Bedolla, R.A.L. Drew, Wettability of TiC by commercial aluminum alloys, *Journal of Materials Science*. 37 (2002) 3509–3514. <https://doi.org/10.1023/A:1016523408906>.
- [156] H.F. Fischmeister, G. Elssner, B. Gibbesch, K.H. Kadow, F. Kawa, D. Korn, W. Mader, M. Turwitt, Solid-state bonding of accurately oriented metal/ceramic bicrystals in ultrahigh vacuum, *Review of Scientific Instruments*. 64 (1998) 234. <https://doi.org/10.1063/1.1144443>.
- [157] J.R. Smith, T. Hong, D.J. Srolovitz, Metal-Ceramic Adhesion and the Harris Functional, *Physical Review Letters*. 72 (1994) 4021. <https://doi.org/10.1103/PhysRevLett.72.4021>.
- [158] E.A.A. Jarvis, E.A. Carter, An Atomic Perspective of a Doped Metal-Oxide Interface, *Journal of Physical Chemistry B*. 106 (2002) 7995–8004. <https://doi.org/10.1021/JP0257348>.
- [159] T. Sun, X. Wu, W. Li, R. Wang, The mechanical and electronic properties of Al/TiC interfaces alloyed by Mg, Zn, Cu, Fe and Ti: First-principles study, *Physica Scripta*. 90 (2015) 035701. <https://doi.org/10.1088/0031-8949/90/3/035701>.
- [160] H. hui Xiong, H. Hua Zhang, H. Ning Zhang, Y. Zhou, Effects of alloying elements X (X=Zr, V, Cr, Mn, Mo, W, Nb, Y) on ferrite/TiC heterogeneous nucleation interface: first-principles study, *Journal of Iron and Steel Research International* 2017 24:3. 24 (2017) 328–334. [https://doi.org/10.1016/S1006-706X\(17\)30047-X](https://doi.org/10.1016/S1006-706X(17)30047-X).
- [161] H.Z. Zhang, S.Q. Wang, The effects of Zn and Mg on the mechanical properties of the Al/TiN interface: a first-principles study, *Journal of Physics: Condensed Matter*. 19 (2007) 226003. <https://doi.org/10.1088/0953-8984/19/22/226003>.
- [162] E.A. Jarvis, E.A. Carter, Importance of open-shell effects in adhesion at metal-ceramic interfaces, *Physical Review B*. 66 (2002) 100103. <https://doi.org/10.1103/PhysRevB.66.100103>.
- [163] J. Akola, H. Häkkinen, M. Manninen, Ionization potential of aluminum clusters, *Physical Review B*. 58 (1998) 3601. <https://doi.org/10.1103/PhysRevB.58.3601>.
- [164] G.E. Totten, D.S. MacKenzie, *Handbook of Aluminum: Vol. 1: Physical Metallurgy and Processes*, CRC Press, (2003). <https://books.google.com/books?id=Wbwv3nt1gp0C>.
- [165] N. Dhariwal, A.S.M. Miraz, W.J. Meng, B.R. Ramachandran, C.D. Wick, Impact of metal/ceramic interactions on interfacial shear strength: Study of Cr/TiN using a new modified embedded-atom potential, *Materials & Design*. 210 (2021) 110120. <https://doi.org/10.1016/J.MATDES.2021.110120>.

- [166] H.E. Schaefer, R. Gugelmeier, M. Schmolz, A. Seeger, Positron Lifetime Spectroscopy and Trapping at Vacancies in Aluminium, *Materials Science Forum*. 15–18 (1987) 111–116.  
<https://doi.org/10.4028/WWW.SCIENTIFIC.NET/MSF.15-18.111>.
- [167] P. (Pierre) Villars, P. (Pierre). Villars, *Pearson's handbook : crystallographic data for intermetallic phases.*, Desk ed., ASM International, Materials Park OH, (1997).
- [168] K. Tanaka, T. Ichitsubo, H. Inui, M. Yamaguchi, M. Koiwa, Single-crystal elastic constants of gamma-TiAl, *Philosophical Magazine Letters*. 73 (1996) 71–78.  
<https://doi.org/10.1080/095008396181019>.
- [169] K. Tanaka, K. Okamoto, H. Inui, Y. Minonishi, M. Yamaguchi, M. Koiwa, Elastic constants and their temperature dependence for the intermetallic compound Ti<sub>3</sub>Al, *Philosophical Magazine A*. 73 (2006) 1475–1488.  
<https://doi.org/10.1080/01418619608245145>.
- [170] M. Nakamura, K. Kimura, Elastic constants of TiAl<sub>3</sub> and ZrAl<sub>3</sub> single crystals, *Journal of Materials Science*. (1991) 2208–2214.  
<https://doi.org/10.1007/BF00549190>.
- [171] R.S. Mishra, N. Kumar, M. Komarasamy, Lattice strain framework for plastic deformation in complex concentrated alloys including high entropy alloys, *Material Science and Technology*. 31 (2015) 1259–1263.  
<https://doi.org/10.1179/1743284715Y.0000000050>.
- [172] C.H. Cáceres, D.M. Rovera, Solid solution strengthening in concentrated Mg–Al alloys, *Journal of Light Metals*. 1 (2001) 151–156. [https://doi.org/10.1016/S1471-5317\(01\)00008-6](https://doi.org/10.1016/S1471-5317(01)00008-6).
- [173] H.W. Rosenberg, W.D. Nix, Solid solution strengthening in Ti–Al alloys, *Metallurgical Transactions* 4 (1973) 1333–1338.  
<https://doi.org/10.1007/BF02644529>.
- [174] P. Kwasniak, H. Garbacz, Screw dislocation mediated solution strengthening of substitutional  $\alpha$ -Ti alloys - First principles investigation, *Acta Materialia*. 141 (2017) 405–418. <https://doi.org/10.1016/j.actamat.2017.09.028>.
- [175] P. Kwasniak, H. Garbacz, K.J. Kurzydowski, Solid solution strengthening of hexagonal titanium alloys: Restoring forces and stacking faults calculated from first principles, *Acta Materialia*. 102 (2016) 304–314.  
<https://doi.org/10.1016/J.ACTAMAT.2015.09.041>.

- [176] F. Ernst, Metal-oxide interfaces, *Materials Science and Engineering: R: Reports*. 14 (1995) 97–156. [https://doi.org/10.1016/0927-796X\(95\)80001-8](https://doi.org/10.1016/0927-796X(95)80001-8).
- [177] V. Botu, R. Ramprasad, Adaptive machine learning framework to accelerate ab initio molecular dynamics, *International Journal of Quantum Chemistry*. 115 (2015) 1074–1083. <https://doi.org/10.1002/QUA.24836>.
- [178] E.J. Pickering, N.G. Jones, High-entropy alloys: a critical assessment of their founding principles and future prospects, *International Material Reviews*. 61 (2016) 183–202. <https://doi.org/10.1080/09506608.2016.1180020>.
- [179] S. Gorsse, D.B. Miracle, O.N. Senkov, Mapping the world of complex concentrated alloys, *Acta Materialia*. 135 (2017) 177–187. <https://doi.org/10.1016/J.ACTAMAT.2017.06.027>.
- [180] D.B. Miracle, O.N. Senkov, A critical review of high entropy alloys and related concepts, *Acta Materialia*. 122 (2017) 448–511. <https://doi.org/10.1016/j.actamat.2016.08.081>.
- [181] S. Gorsse, J.P. Couzinié, D.B. Miracle, From high-entropy alloys to complex concentrated alloys, *Comptes Rendus Physique*. 19 (2018) 721–736. <https://doi.org/10.1016/J.CRHY.2018.09.004>.
- [182] W.M. Choi, Y.H. Jo, S.S. Sohn, S. Lee, B.J. Lee, Understanding the physical metallurgy of the CoCrFeMnNi high-entropy alloy: an atomistic simulation study, *NPJ Computational Materials* 4 (2018) 1–9. <https://doi.org/10.1038/s41524-017-0060-9>.
- [183] Y.-M. Kim, Y.-H. Shin, B.-J. Lee, Y.-M. Kim, Y.-H. Shin, B.-J. Lee, Modified embedded-atom method interatomic potentials for pure Mn and the Fe-Mn system, *AcMat*. 57 (2009) 474–482. <https://doi.org/10.1016/J.ACTAMAT.2008.09.031>.
- [184] C. Wu, B.J. Lee, X. Su, Modified embedded-atom interatomic potential for Fe-Ni, Cr-Ni and Fe-Cr-Ni systems, *Calphad. C* (2017) 98–106. <https://doi.org/10.1016/J.CALPHAD.2017.03.007>.
- [185] W.P. Dong, H.K. Kim, W.S. Ko, B.M. Lee, B.J. Lee, Atomistic modeling of pure Co and Co–Al system, *Calphad*. (2012) 7–16. <https://doi.org/10.1016/J.CALPHAD.2012.04.001>.